Frequency Evolution
of
Integrated Pulse Profiles

A Diploma Thesis

Emmanouil Angelakis
Under the supervision of Professor John H. Seiradakis

Department of Physics, Section of Astrophysics, Astronomy and Mechanics
ARISTOTLE UNIVERSITY of THESSALONIKI

To my angels, Evangelia and Katerina Angelaki and the memory of my precious father who passed away on 27^{th} October 1997.

Contents

Chapter 1

Pulsating Stars

Although it may sound impressive *pulsars* only stands for Pulsating Stars. With respect to the fundamental quality of fast rotating neutron stars to send precisely periodic pulses to a terrestrial observer, pulsars become perceivable as though they were cosmic lighthouses (in case of correct orientation of their magnetic field's axis to our line-of-sight).

Born during a titanic supernova explosion that left behind only a tiny (in comparison with the usual stellar dimensions) perfect super-dense spherical remnant, pulsars serve as ideal cosmic laboratories to study physical conditions completely unattainable on earth. Great excitement, surprise and inspiration accompanies each scientific pulsar approach since it would not be exaggeration to say that they are the dense-most state of matter that contemporary physics tools are adequate to describe.

The present work has proved to us the quotation opening Manchester and Taylor's text book "Pulsars" [Manchester and Taylor, 1977] to be the most accurate to describe our feelings. They wrote:

> To Jocelyn Bell, without whose perceptiveness and persistence we might not yet have had the pleasure of studying pulsars.

1.1 Stellar Evolution: from Birth to Death

Most of the tiny silver dots we see when gazing at the night sky are subject to an interesting state of equilibrium. What relentlessly threats them of death is what triggers their will to live. Its majesty, Gravity. The cosmic governor! The force capable of turning a cold dark cloud of interstellar medium into a steadily shiny fireball which in turn could warm up the birth of an inconceivably long series of species inhabiting a wonderful blue dot in the cold vacuum of the universe.

Initiating their history as gaseous clouds composed mainly of Hydrogen, stars are unable to avoid the gravitational pull and start falling into themselves. The more they contract the more their core temperature and pressure increases.

Passing through several more or less known stages of evolution they eventually give birth to a new object: a star! That is, core conditions are extreme enough to trigger the nuclear reactor in their center. From that moment, and for more than the 80% of their whole life, stars obey a dynamic equilibrium occupying a position in the main sequence. The gravitational pressure is resisted by the radiation pressure constantly generated by the nuclear fusion of four atoms of Hydrogen into an Helium one.

Inevitably, Hydrogen gradually expires and when about 13% of the star's initial mass has been consumed dramatic changes and titanic events start destroying the so far serene stellar life. Roughly about once every century in our galaxy the end of equilibrium breaks down with a majestic supernova explosion preceded by a short period during which the star exists as a super-giant. A few seconds are enough to violently erase what billions of years built. The core of the star collapses living behind fast expanding layers of stellar material. Simultaneously, a white dwarf, a neutron star or a black hole is formed at the center of the star depending strongly on the initial amount of material composing it.

Now, the end of a life becomes the beginning of another. On the one hand, the supernova debris spreading through the interstellar space will some day be engulfed in a greater cloud to create a new star. On the other, the shock wave from the explosion may cause the contraction of a nearby gaseous cloud accelerating a second generation star birth process. But even more interestingly, new fascinating types of equilibrium occur supporting the existence of super-dense stellar corpses.

1.2 Neutron Stars: Astonishingly Exotic Guys...

The 34 sequential years of pulsar studies seem to imply that the theoretical speculations of Landau [Landau, 1932] and Baade & Zwicky [Baade and Zwicky, 1934] have been more than science fiction. Considering the possible scenarios for stellar death, they predicted the existence of an exotically super-dense object named *neutron star* to be the remnant of a star with an initial mass (i.e. during the main sequence stage) heavier more than 5 but less than 20 $M_{\odot}$ [Seiradakis and Varvoglis, 1994]. For such a star, no radiation pressure is intense enough to resist the gravitational pull of its inner layers on the outer ones. When Such a star collapses, a new kind of pressure is needed to stabilize it. According to their idea the pressure that could eventually hold back further collapse of the object is due to Pauli's law for fermions in conjunction with Heisenberg's uncertainty principle [Seiradakis and Varvoglis, 1994]. Qualitatively speaking, it is well understood that one is not allowed to decrease the product between the uncertainty in the position and that in the momentum of a particle bellow the limit of Planck's constant, h. That is:

$$\Delta x \cdot \Delta p \geq h \tag{1.1}$$

Where,Δx and Δp is the uncertainty in the position and that in the particle's momentum, respectively. Hence, if very little free space (Δx) is given to particles to move about, their momentum should increase so that the product $\Delta x \cdot \Delta p$ exceeds h. But increasing momentum is equivalent to increasing the kinetic energy and therefore the pressure. This mechanism is known as *degenerate fermions pressure* and occurs in environments of extremely high densities as the ones characterizing the interiors of neutron stars. For the case under examination, even the degeneracy of electrons is worked out to be too weak to resist the gravitational pull. However, it is easy to demonstrate that degenerate neutrons can provide the pressure necessary for the establishment of equilibrium in the interior of a body of between 1.4 and 3.2 $M_{\odot}$ blended in a sphere of a 10-kilometer radius!

Let us recall what has just been stated. A neutron star possesses a mass of about half a million planets-Earth (in average) squeezed in the volume of a sphere 20 km across! Can you imagine how dense a body of that sort will be? Simple calculations will lead to a typical density of the order of $10^{14} gr/cm^3$, that is equal to the typical nuclear density [Charalampous, 1981]! The above conditions lead to an escape velocity of roughly 64% of the speed of light since the gravitational pull on the surface of such an object exceeds that on Earth by a factor of 200 billions! Here on Earth, a cubic centimeter of such material would be as heavy as 650 million tons [Kramer, 1995]. From a different perspective, the highest mountain on a neutron star would hardly reach a few centimeters height.

Slightly more detailed reflections on the process leading to the formation of a neutron star lead to further surprises. Imagine a star with a mass between 5 to 20 $M_{\odot}$ disintegrating during a powerful supernova explosion. Its core collapses into a corpse 20 km in diameter. The conservation of magnetic flux determines that the final stage (i.e. the super-dense remnant) will exhibit an enormously strong magnetic field. An estimation of **B** based on typical values of the involved parameters would imply surface fields as strong as a few thousand billions times that of the Sun! It is this fact, as we discuss later, that makes neutron stars periodically visible in the radio sky.

But, it is not only magnetic flux that obeys a conservation law. Angular momentum does so as well. Hence, it is reasonable to expect the strange guy under our examination to rotate very fast in the heavens. Would it be too shocking to accept a spin frequency of typically one rotation each second? Or, would a rotation per millisecond sound inconceivable? Whether it does or not, the sophisticated studies of pulsars that have been carried out from some of the most famous radio astronomy groups during the last one third of the century prove that such exotic objects do exist.

1.3 The Discovery and Interpretation Attempts

Since 1934 when Walter Baade & Fritz Zwicky proposed the existence of the neutron star as an end product of stellar evolution, only in 1967 an observation brought to light their idea.

It was in July 1967 when Jocelyn Bell (Figure 1.1), under the supervision of Antony Hewish (Nobel prize 1974), carried out several series of observations with a low frequency radio telescope operating at a frequency of $81.5\ MHz$. Her project was the study of the angular structure of compact radio sources by observing the scintillation caused by the irregular structure of the interplanetary medium [Hewish et al., 1968]. While Jocelyn was investigating the pen chart recordings obtained with their observing system she realized that a series of clock-like radio pulses had been recorded! After allowing for mistaken observational proce-

Figure 1.1: Professor J. Bell during one of her amazingly interesting lectures.

dure and justifying the correctness of their technique, quite methodical and intense study was dedicated to the answer of the question:"What sort of source could emit such signals?"

Even extraterrestrial intelligence, namely little green men, among a long sequence of possible answers was examined as the possible origin of so regularly emitted pulses. It is impressive how remarkable is the signal analysis contained in the legendary discovery letter published in Nature in February 1968 [Hewish et al., 1968]. Let us recall the abstract of their report:

> Unusual signals from pulsating radio sources have been recorded at Mullard Radio Astronomy Observatory. The radiation seems to come from local objects within the galaxy, and may be associated with oscillations of white dwarf or neutron stars.

The surprising regularity of the pulse's arrival time led to a very restricted group of assumptions with regard to the pulses' origin. First of all, the idea that the signals resulted from a binary revolution appeared to be irrelevant mainly for two reasons [Seiradakis and Varvoglis, 1994]:

- It is trivial to rule out a white-dwarf binary since the revolution period cannot be shorter than $1.7\ s$ whereas pulsars of far shorter period had been discovered.

- Moreover, a neutron-star binary also was worked out to be inadequate to give an explanation. Such systems emit gravitational waves at quite high rates at rotational energy's expense. Therefore, in case they were the origin of pulses a constantly fast decrease in the pulse period should be observed. In fact, what has been observed is a period increase instead.

Soon, the assumption of a an oscillating white dwarf or neutron star was found to be impossible as well as that of a rotating white dwarf. What was eventually and after deep speculations left to serve as the most promising explanation was that of a *fast rotating neutron star*. Later we discuss the most contemporary ideas concerning how such an object could result in the observed signals and many of their observed properties 1.5.

1.4 Observational Overview

Since July 1967 when the first pulsar, PSR B1919+21, was discovered, interestingly sophisticated observing systems have been recording signals from pulsars. Long series of data reveal numerous noteworthy pulsar properties.

1.4.1 Emission range

As we discuss later in more detail, the energy source of pulsars is their rotational energy, converted to radiation, as they slowdown. As they spin rapidly around their axis with their magnetosphere following their rotation (locked onto their surface), neutron stars gradually loose kinetic energy transforming it into radiation

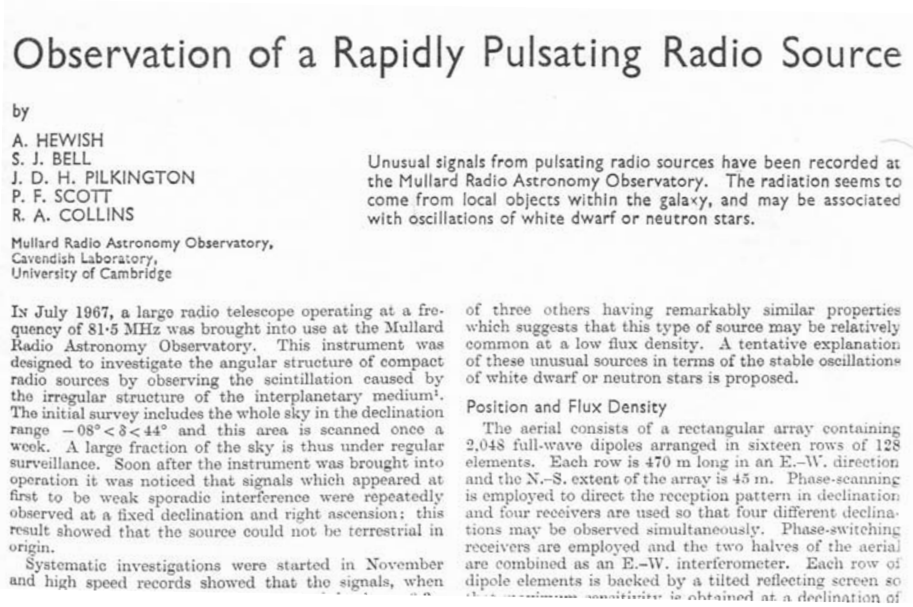

Observation of a Rapidly Pulsating Radio Source

by

A. HEWISH
S. J. BELL
J. D. H. PILKINGTON
P. F. SCOTT
R. A. COLLINS

Mullard Radio Astronomy Observatory,
Cavendish Laboratory,
University of Cambridge

Unusual signals from pulsating radio sources have been recorded at the Mullard Radio Astronomy Observatory. The radiation seems to come from local objects within the galaxy, and may be associated with oscillations of white dwarf or neutron stars.

IN July 1967, a large radio telescope operating at a frequency of 81·5 MHz was brought into use at the Mullard Radio Astronomy Observatory. This instrument was designed to investigate the angular structure of compact radio sources by observing the scintillation caused by the irregular structure of the interplanetary medium[1]. The initial survey includes the whole sky in the declination range $-08° < \delta < 44°$ and this area is scanned once a week. A large fraction of the sky is thus under regular surveillance. Soon after the instrument was brought into operation it was noticed that signals which appeared at first to be weak sporadic interference were repeatedly observed at a fixed declination and right ascension; this result showed that the source could not be terrestrial in origin.

Systematic investigations were started in November and high speed records showed that the signals, when

of three others having remarkably similar properties which suggests that this type of source may be relatively common at a low flux density. A tentative explanation of these unusual sources in terms of the stable oscillations of white dwarf or neutron stars is proposed.

Position and Flux Density

The aerial consists of a rectangular array containing 2,048 full-wave dipoles arranged in sixteen rows of 128 elements. Each row is 470 m long in an E.–W. direction and the N.–S. extent of the array is 45 m. Phase-scanning is employed to direct the reception pattern in declination and four receivers are used so that four different declinations may be observed simultaneously. Phase-switching receivers are employed and the two halves of the aerial are combined as an E.–W. interferometer. Each row of dipole elements is backed by a tilted reflecting screen so

Figure 1.2: The front page of the legendary Nature letter.

through processes that will be mentioned later. This is the very idea that also interprets the observed increase in their period.

It would not be true at all to say that pulsars emit only in the radio band. Actually their radio emission represents only a small part of the total energy loss. The Crab pulsar (the youngest known pulsar), for example, emits detectable pulses over the whole spectrum. Radiating from radio to high energy gamma-rays, it emits most of its energy in the X-ray region. In Figure 1.3 an optical photograph of its neighborhood is shown during the on and off phase. However, high energy radiation appears to be characteristic of the youngest pulsars.

As for the radio emission, which offers the best possibility for studying pulsars, one should investigate the pattern of its spectrum. Figure 1.4 illustrates typical radio spectra which are described by a law of the form:

$$S = S_0 f^a \tag{1.2}$$

Where, S is the *flux density* and a the *spectral index*. In general, it is quite steep and becomes even steeper at higher frequencies for most pulsars.

1.4.2 Radio pulse morphology

Before proceeding with the study of pulse morphology, we should first distinguish between *individual* pulses and the *integrated pulse profile*.

In the previous discussion it was repeatedly mentioned that what makes pulsars special, at the first place, is their peculiarity to send pulses of radio rather than continuous radiation. Each and every pulse received is named as *individual* or *single*. Quite wide variation in the properties of single pulses can be observed, as we discuss in the next Paragraph.

Assuming that one can average long series of sequential individual pulses, one can construct what is known as *integrated pulse profile*. A pattern that, for the majority of cases, serves as the pulsar fingerprint. Later, the above distinction will hopefully become more clear through a more extended discussion.

Individual pulses

The specific shape of single pulses can change dramatically from period to period. Very often the emission stops and no pulse can be observed, for several periods. Figure 1.5 shows a series of sequential pulses. It is clear how randomly the received flux is distributed over the period.

Most of the known pulsars emit pulses that cover only a small portion of their period, usually between $5^o - 15^o$, assuming that a full period covers 360^o.

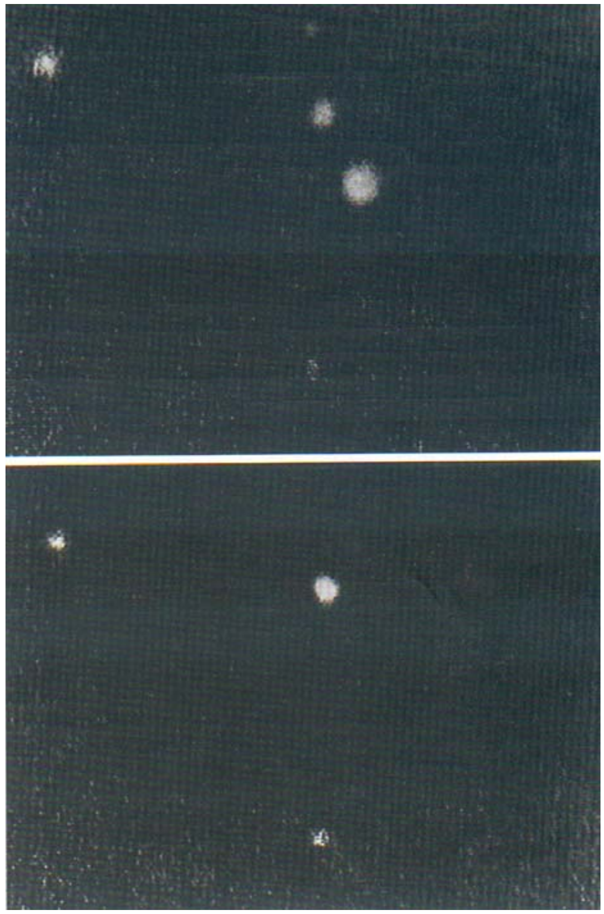

Figure 1.3: The Crab pulsar pulsating at optical. At the top picture the pulsar is “on”

A single pulse often consists of a number of *components* (sub-pulses) that can be observed only with systems supporting high time resolution. Even better resolution can reveal the microstructure of sub-pulses.

In some cases *interpulses* are observed, as well. That is, for a small portion of the period a pulse-like pattern completely separated from the *main pulse* is received. Figure 1.5 is the best to describe that phenomenon.

The individual pulses are often very highly polarized; this is characteristic of strong magnetic fields.

There are pulsars that display the *nulling* phenomenon. That is, for several sequential periods no pulse is observed. The duration of nulls and the time span between their occurrence vary randomly about characteristic values. For instance, nulls of two or three pulses long may occur at intervals of order one hundred pulses. Nulling seems to be a characteristic of older pulsars.

Drifting is also an interesting individual pulses peculiarity that is observed in many long-period pulsars. Sub-pulses of successive periods appear at progressively changing longitudes. Figure 1.6 illustrates a typical nulling case as well as a drifting one.

Integrated pulse profiles

It has been stated that integrated pulse profiles serve as fingerprints for each particular pulsar at fixed frequency.

In order to obtain the integrated pulse profile, people superpose a sequence of some hundreds of single pulses. The resulted pattern then becomes “stable” in a sense that it does not change if more single pulses are added to it.

This statement should not lead to the misconception that for all known pulsars the profile remains unchanged in time. Important modifications can be observed. For instance, many pulsars share two completely different profiles and switch between them unexpectedly (*mode changing*). Moreover, integrated profiles can change over frequency. By the way, this very issue is the motivation for the present project.

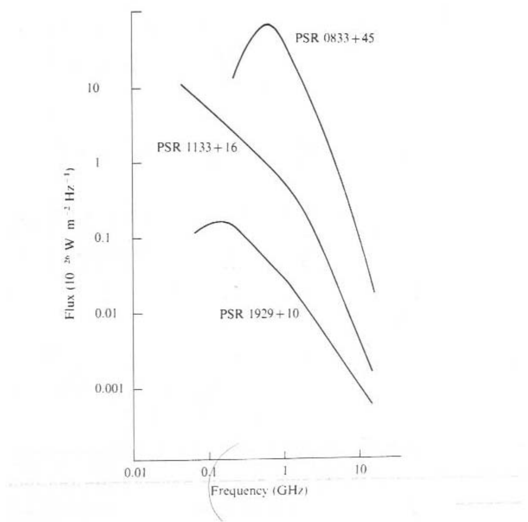

Figure 1.4: Typical pulsar spectra.

In general, integrated profiles may occupy between 2% to 10% of the period though there are exceptions. Some pulsars posses profiles that cover even 60 out of 360 degrees of rotation.

Similarly to single pulses, integrated profiles usually consist of individual components more or less distinct from each other. Their number is often close to two or three but five-component profiles have been observed, as well (see Figure 1.8). As we discuss later their appearance is attributed to the intersection of our line-of-sight with discrete emitting regions.

A lot of information, concerning the physical processes occurring at the neutron star, can be accumulated from the study of integrated polarization patterns.

As a conclusion we should mention the existence of inter-pulses in many integrated pulse profiles. Figure **??** illustrates a typical profile of that sort.

1.4.3 Pulse timing

State-of-the-art observing systems have made precise timing observations achievable nowadays. The unfamiliar with this topic may be surprised by the accuracy with which people can record pulsar signals. Nevertheless, very important phenomena have been disclosed thanks to the accuracy provided by some available instruments.

To indicate how fast the observational systems should be, we would give the example of millisecond pulsars. As we mentioned earlier the profile possesses, in many cases, detectable microstructure. You can perceive now the need in high receiving speed in order to detect such fine details.

The following paragraphs refer to some basic topics, regarding pulse timing, and imply the necessity of extremely fast observing systems.

Period distribution

The most important parameter, in the context of pulse timing studies, is of course the pulsars' period.

Figure 1.9 illustrates the period distribution for the so far known pulsars. Two main populations can be seen. Most of the pulsars occupy the long period range whereas a fairly large number can be found at periods of the order of 10^{-3} seconds. The former group includes the so called *normal pulsars* and the later the *millisecond* pulsars. We discuss this distinction in more detail later (paragraph 1.4.3).

From the roughly 1200 pulsars known so far the fastest, PSR J1939+2134, spins about 645 times per second! That is, it has completed about 58000 rotations since you have started reading this paragraph! On the contrary, the one with the longest period, PSR 2144-3933, rotates once each 8.5 s. Hence, generally speaking we would say that pulsars' periods cover a range of 3 orders of magnitude.

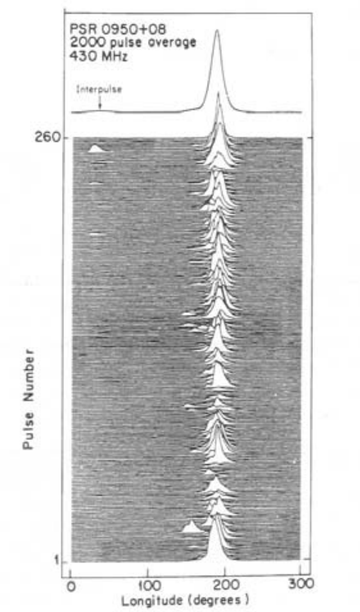

Figure 1.5: Sequencial single pulse

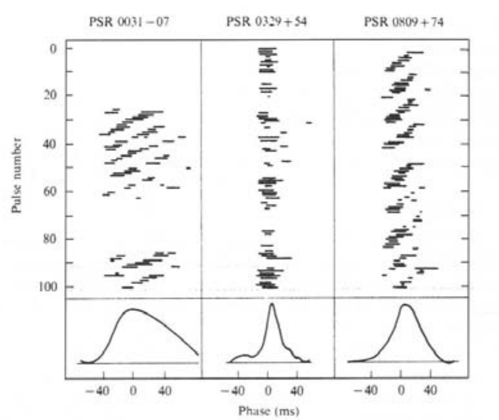

Figure 1.6: Drifting and nulling. Each horizontal line is centered on the expected arrival time, with time increasing downwards and to the right. The positions of each sub-pulse are shown.

P-$\dot{P}$ diagram

In Section 1.4.1 we stated that the energy source of the pulsar is the rotational slowdown it undergoes. Therefore, it is reasonable to expect the pulsar periods to increase since they gradually loose kinetic energy transforming it into radiation. The measure of how fast the period lengthening happens, is of course the period derivative, $\dot{P}$. Figure 1.10 demonstrates the $P - \dot{P}$ diagram for the majority of known pulsars.

Avoiding a detailed talk on this diagram (which is of significant importance) we only point out that it proves the evolutionary path to be specific for each pulsar. In the opposite case, most of the pulsars should be concentrated around a line rather than been scattered over the whole plot as they are.

Pulsar ages

Very important conclusions may be reached after careful investigation on the period distribution diagram and that of slowdown rates.

For the majority of pulsars the rotation slows down on a timescale of 10^6 to 10^8 years. Additionally, most of the pulsars start their lives with periods below 100 milliseconds and cease to radiate after a few tens of million years. The birthrate deduced by this assumption is of the order of 1 per 50 years being consistent with an origin during the violent collapse of massive stars observed as supernovae.

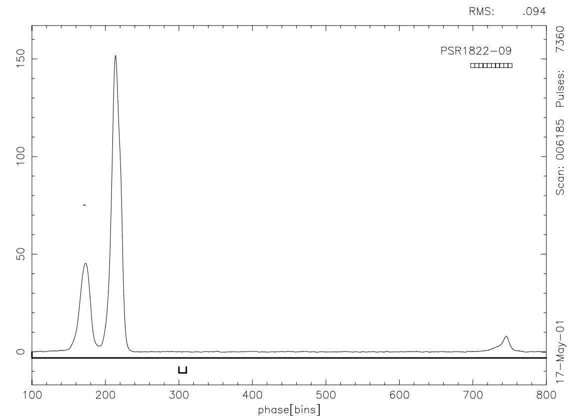

Figure 1.7: Profiles with interpulses.

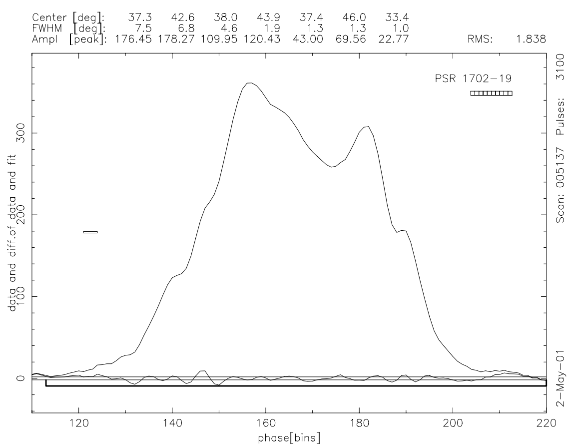

Figure 1.8: A profile of multiple components.

Besides, the study of the slowdown rates can lead to the estimation of *characteristic ages* for pulsars. Assuming that they loose energy through dipole radiation, not very complicated calculations reveal that their characteristic age is:

$$\tau = P/2\dot{P} \tag{1.3}$$

This value is only approximate since very general assumptions have been taken into consideration . Nevertheless, it serves as an indicator for the time spans that pulsars may spend radiating.

Classification

The plot shown in Figure 1.9 leads to a classification of pulsars into two groups according to their period.

The group laying over the long period regime consists of new born pulsars that carry stronger magnetic fields than what the second group does. These pulsars are known as *normal pulsars*.

The minority of the total pulsar population spin with very short periods. Their slowdown rates are yet smaller compared to the ones of normal pulsars as a result of weaker magnetic fields. They are refered to as *millisecond pulsars*.

The above classification is of physical content rather than only a formalized grouping. Millisecond pulsars are believed to be neutron stars that have passed their normal age span of activity. At present, their magnetic fields have decayed, but they have rejuvenated by spin-up process involving a binary partner.

Timing irregularities

A spinning body with such large moment of inertia (about $10^{44} g \cdot cm^2$) as a neutron star isolated in space, is reasonably expected to possess a remarkable uniformity of rotation rate. Therefore, it is not surprising that in a time scale of several days pulsars do not display any irregularity in their period. However, some very

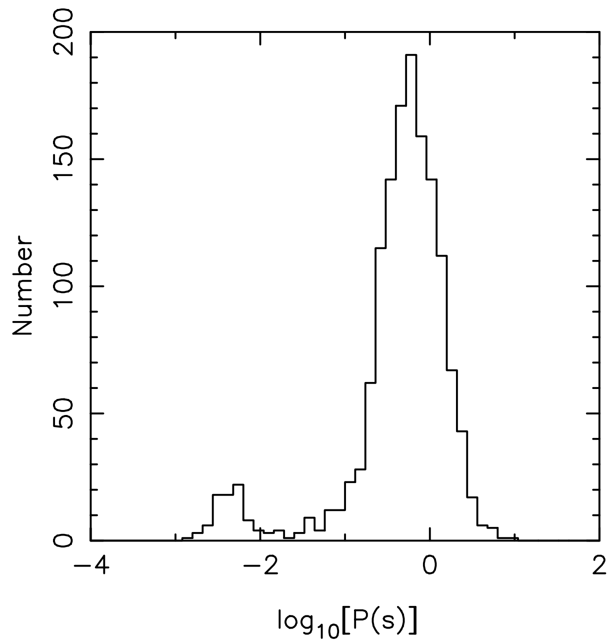

Figure 1.9: Pulsars period distribution [Hobbs, 2001].

interesting sorts of irregularities in their rotation have been observed. Two categories of timing irregularities may be established. A general noisy and rather continuously erratic behavior and a spectacular step change in rotation speed, known as *glitch*. Both classes of irregularities have been mainly observed in young pulsars.

In the context of a purely descriptive reference to timing irregularities it would not be necessary to give a detailed description of all the observed phenomena. We take the opinion that a short description of glitches would be enough.

Glitches are not so often. They have been observed in 21 pulsars, at least so far, most of which are in young pulsars. They are characterized by a step decrease in period followed by a period of slow recovery. Figure 1.11 is a typical diagram showing a glitch. The most promising theory that tries to explain glitches discuss the possibility of internal changes. Specifically, it has been examined the possibility of a step change in period due to changes in equilibrium ellipticity of the crust that may be resulted from the centrifugal force decrease.

Dispersion

In the general framework of pulse timing it would be a mistake to refrain from dedicating time to a discussion about dispersion.

Radio waves propagating through the interstellar medium encounter ionized gas, whose refractive index differs from unity. As a result, a delay in the pulse arrival time arises. The magnitude of the delay depends on the total electron content of the propagation path and the observing frequency in a manner that higher frequencies travel faster. Figure 1.12 perfectly supports the above description. The whole phenomenon is named *dispersion*.

Comparing the pulse arrival time at different frequencies one can estimate the pulsar's distance. If t is the dispersive delay added to the free space travel time (in seconds) and f the observing frequency (in MHz), then the relation between them is given by:

$$t = DM/2.41 \cdot 10^{-4} \cdot f^2 \tag{1.4}$$

where DM is the *dispersion measure* defined as:

$$DM = \int_0^L n_e dl \tag{1.5}$$

Measured in $pc \cdot cm^{-3}$. In the above equation, n_e is the electron number density and L the total path length. By measuring the difference in the arrival time dt at two different observing frequencies we can calculate

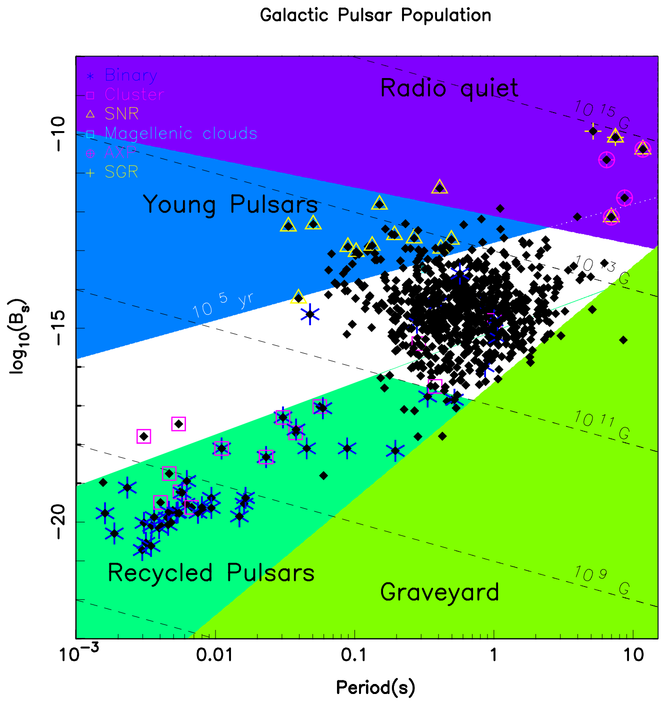

Figure 1.10: $P - \dot{P}$ diagram for most of the known pulsars [Hobbs, 2001].

DM. Then, for given electron distribution (expressed by n_e) we can estimate L which is of the order of pulsar's distance.

Great deal of time and of computational resources is dedicated to the data *de-dispersion* since dispersion causes what is known as *pulse dispersion broadening*; that is, the broadening of pulse profile resulting in from wide bandwidth observations. If B is the receiver's bandwidth (in MHz) and Δt the dispersion broadening (in milliseconds), then:

$$\Delta t = 8.3 \cdot 10^3 \cdot DM \cdot f^{-3} \cdot B \tag{1.6}$$

During the actual data analysis of our project we use this parameter in order to calculate our errors, as will be mentioned later.

1.4.4 Distances and galactic distribution

Four different methods are used for the estimation of pulsar distances: parallax, hydrogen absorption, optical identifications and dispersion measure.

The method based on the parallax takes the advantage of the annual parallactic motion. Unfortunately, this method can only be used for pulsars within 1 kpc from the Sun.

The second method, presupposes a dynamical rotation model of the Galaxy. Having measured the absorption, due to spin-flip Hydrogen transition (at 21 cm), along the line of sight, one can infer the pulsar's distance.

A different way to estimate the distance of a pulsar is to associate it with a supernova remnant and subsequently measure the distance of the optical object.

The most used method is the one base on dispersion measure's studies. In paragraph 1.4.3 we gave a detailed description of this method.

From the very early days when the first surveys were under way the spatial distribution of pulsars was under examination. In Figure 1.13 we present the galactic distribution of known pulsars. It is immediately seen that they concentrate close to the galactic plane. Most pulsars are concentrated within a layer about 1 kpc thick and within a radial distance from the center of the order 10 kpc. Normal pulsars are found on the galactic plane whereas millisecond ones are distributed more isotropically. Many of the later are found in globular clusters as well. It is estimated that, in total, 10^5 to 10^6 active pulsars are present in the Galaxy. The so far known pulsars are about 1200.

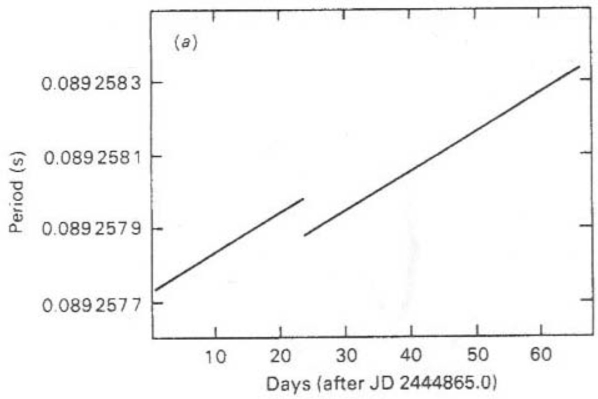

Figure 1.11: . The glitch in Vela pulsar (October 1981).

1.5 Contemporary Knowledge of Pulsars

Here we intent to summarize the most important results recently achieved in pulsars research. Before we proceed it is important to mention that the following description of physical processes will be made from a qualitative point of view. In particular cases, where quantitative and a more accurate approach is necessary, our perspective selectively changes.

1.5.1 Neutron star structure

It has already been pointed out that from the very early pulsar days a rapidly rotating neutron star became clear to be the most eligible explanation for pulsars. It is interesting therefore to concentrate on the structure of such objects for a while.

The interior

Figure 1.14 illustrates the basic ideas people share nowadays as regards the interior of a neutron star. There, a typical neutron star of 1.4 $M_\odot$ and a diameter of about 10-20 km is shown. Therefore, the deduced central density is roughly of the order $3 \cdot 10^{14}$ to $3 \cdot 10^{15}$ gcm^{-3}.

Moving from the surface of the star inwards to its center the density runs from $10^{\,6}$ to $10^{15} gcm^{-3}$ covering a range of about nine orders of magnitude. The main body of a neutron star is believed to consist mainly of two components. A crystalline solid crust, 1 km thick, and a neutron liquid interior. The division between them is at a density near $p_0 = 2.8 \cdot 10^{14}$ gcm^{-3}.

The outer part of the crust is very rigid and dominated by iron nuclei. As the density increases, deeper in the star, more and more electrons penetrate the nuclei and combine with protons to form exotic nuclei with unusually large neutron numbers [Lyne and Graham-Smith, 1998].

At the *neutron drip point*, that is at density as high as $4 \cdot 10^{11}$ gcm^{-3}, almost no neutrons can be found outside the nuclei. Densities higher than this cause the most massive nuclei to become unstable and subsequently embedded in a neutron fluid [Lyne and Graham-Smith, 1998].

The central core consists only of a neutron fluid, containing a small proportion of electrons and protons. Both the neutron and the proton fluid are superfluids [Lyne and Graham-Smith, 1998].

Even more exotic states of matter could characterize the central regions. For instance, at densities of about $6 \cdot p_0$ neutrons may be squeezed and form mesons and kaons. A solid core deduced by such a process would be important for the interpretation of an outstanding pulse timing irregularity known as *glitch*. Moreover, all these extraordinary states of matter affect the cooling rates of a neutron star, since they allow energy to be lost as a flux of neutrinos.

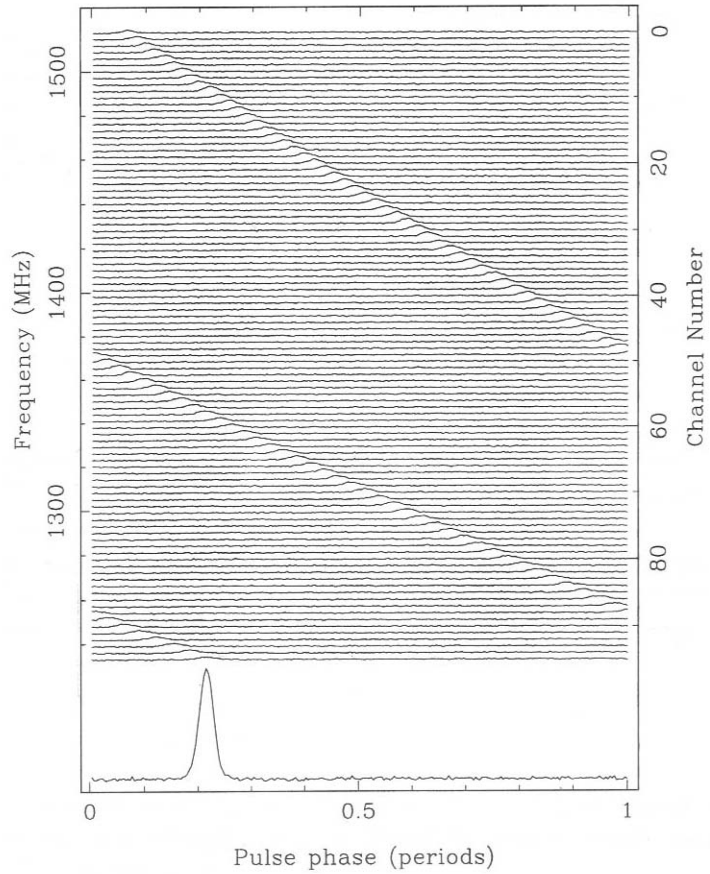

Figure 1.12: Frequency dispersion in pulse arrival time.

The exterior

It has been explained earlier (Section 1.2) that neutron stars are very strongly magnetized. Their magnetic field strengths correspond to the conservation of magnetic flux of a normal star with a field of order 100 $gauss$. Young pulsars have dipole field strengths close to 10^{12} $gauss$, while 10^{10} $gauss$ is a typical value for old pulsars. In millisecond pulsars even weaker may fields occur (10^{8} $gauss$).

Despite the fact that the presence of an extremely strong magnetic field , which like a rigid body co-rotates with the rapidly spinning neutron star, is the reason for all the observed pulsar radiation, there is very little effect on the structure of the star. Only a modification of the crystal structure is deduced. However, outside the star the field dominates all the physical processes. Skipping a more detailed description of this topic we only underline the importance of a field configuration as the one shown in Figure 1.15. This arrangement in conjunction with the field strength will serve as the basic idea to explain the pulses we receive.

1.5.2 The emission mechanism

The years following the pulsar discovery were ones of intensive activity trying to deduce a reasonable explanation for their periodic signals. Soon, it became clear that pulsars could not be oscillating neutron stars but rather rotating ones (remember Section 1.3). The radiation was also established to be emitted in a narrow lighthouse beam locked on the surface of the star co-rotating with it.

The proposed models should therefore allow the radiation to be emitted in the form of a narrow beam and further to predict emission over the whole electromagnetic spectrum. Mainly, two theories were extensively explored:

- The *outer magnetospheric gap*, according to which the radiation originates far out in the magnetosphere, close to the velocity-of-light cylinder.

- The *polar cap* model, which placed the source of the emission immediately above a magnetic pole.

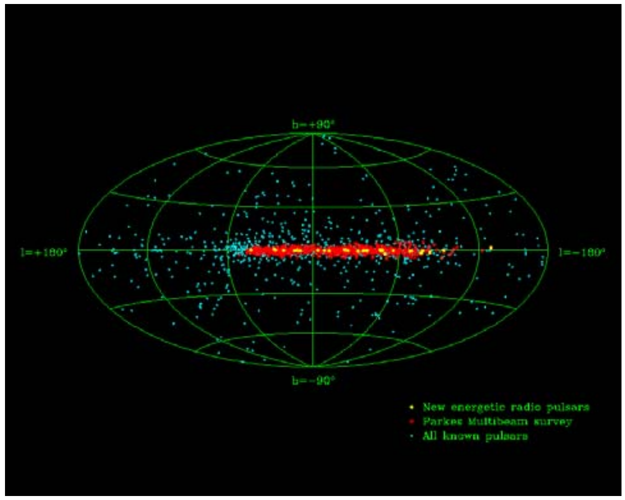

Figure 1.13: The galactic distribution of pulsars.

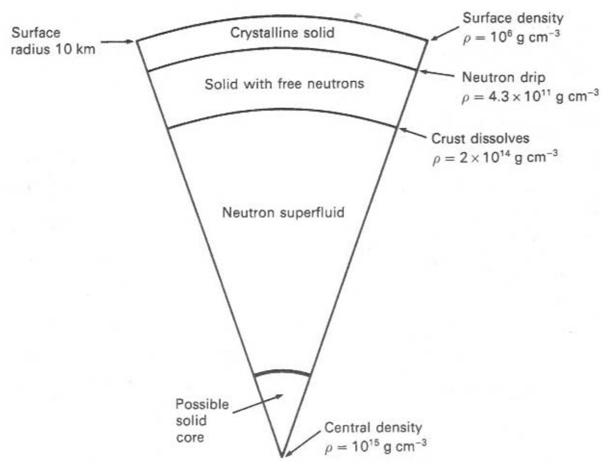

Figure 1.14: Typical cross-section of a neutron star.

Beamwidth and polarization studies gave evidence for the former, while the later was supported by the high energy radiation observed from young pulsars (such as Crab and Vela pulsars).

In both, outer magnetospheric gap and polar cap, regions the radiation is deduced by the acceleration of charged particles at high energies along the field lines. Hence, the radiation is directed along the particle flow (i.e. along the magnetic field lines).

Nowadays, most astrophysicists take the opinion that not a single region is responsible for the radiation. Radio emission is taking place at the polar cap whereas high energy radiation comes from the outer magnetospheric gap.

The outer magnetospheric gap

In Figure 1.16 we give a picture of the region far out in the magnetosphere where the high energy emission originates. This territory is close to velocity-of-light cylinder. Its thickness may be of several kilometers.

The dominating emission mechanism can be roughly described as follows. Electron-positron pairs are being created via the interaction of gamma rays with either magnetic field or low energy photons. The members of the pair are separately accelerated along the field lines. Their energy may reach very high values. Successively, they radiate gamma rays (either by *curvature radiation* or by *inverse Compton collisions* with low energy photons). These gamma rays may interact once again creating pairs and so on. Soon, a cascade of high energy radiating particles appears.

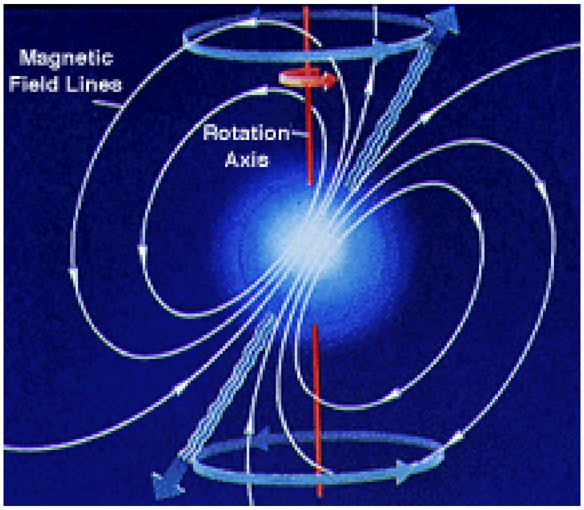

Figure 1.15: The typical magnetosphere's configuration. The field here is assumed to be bipolar. Notice the inclination between the rotation axis to that of magnetic field. This is the reason for the fact that we observe periodical pulses instead of a continuous radiation [Pasachoff, 1998].

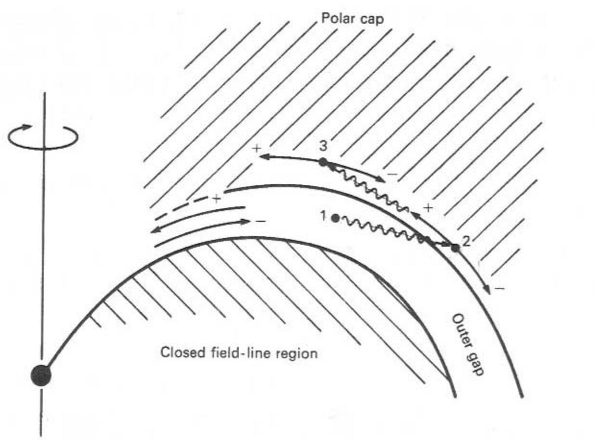

Figure 1.16: The cascade process in the outer magnetospheric gap.

The polar cap

Polar cap model appears to be the most popular among the models proposed to explain the radio emission. Provided that this frequency regime characterizes the majority of pulsars, it is important to give a more detailed description.

Figure 1.17 gives an illuminating description of the radio emission according to the polar cap model. The first to notice is of course the conical shape of the radiation beam.

In contrast to the high energy regime (outer magnetospheric gap), the radiation originates very close to the surface of the star. Charged particles are accelerated in a vacuum gap over the magnetic pole. Each one of them is accelerated along a field line and emits coherent synchrtron radiation.

The cone-like beam is limited by those field lines that tangentially meet the velocity-of-light cylinder. Figure 1.18 demonstrates the geometry of the polar cap in the case of a dipole field with its axis aligned with the rotation axis.

1.6 Applications

Apart from being extraordinarily interesting itself the study of pulsars may provide important information for several astrophysics's problems other than those closely related to neutron stars.

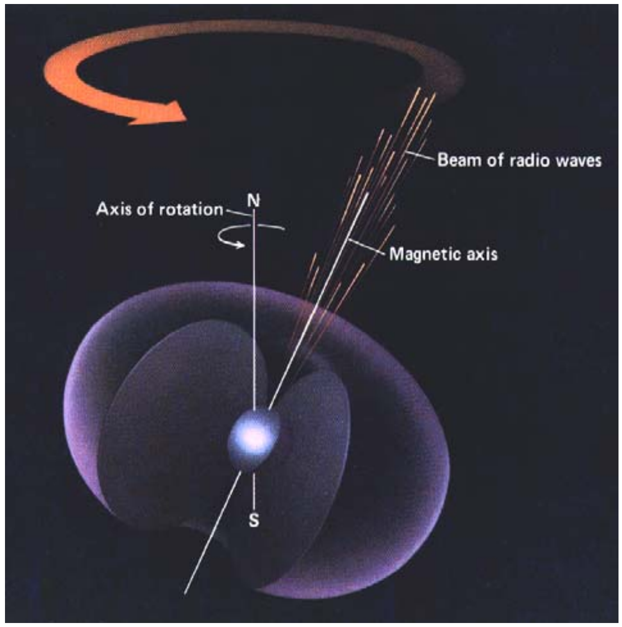

Figure 1.17: The polar cap model [Pasachoff, 1998].

Interstellar magnetic field

Pulsar radio waves may be the most accurate means to study the interstellar magnetic field. The idea hidden behind such probes is very simple.

The high magnetic field occurring at the pulsar causes the radio waves leaving its magnetosphere to be linearly polarized. This is not surprising, of course, since $10^{11} gauss$ is a typical magnetic field strength. While waves propagate through interstellar space they are subject to *Faraday rotation* due to the weak interstellar field. Measurements of this effect on the received signals provide us with information about the magnetic field along the line-of-sight. The estimated magnetic field strength of the interstellar medium is of the order 1 to 10 gauss.

Interstellar electron density

In Paragraph 1.4.3 we discussed the dispersion effect on the received pulsar signals. That discussion implies an accurate method for probing the interstellar electron density along the line-of-sight. Nowadays, pulsars serve as means for even mapping the electron distribution in the Galaxy, at least for the galactic plane (where most of the known pulsars are located).

Testing the theory of General Relativity

The earliest classical test of general relativity involved accurate measurements of the precession of the orbit of Mercury. Since then, the 34 years of continuous pulsar studies proved pulsars to be an astonishingly precise system to test the gravitational theory. Timing observations of PSR B1913+16 gave a strong evidence for the correctness of the theory.

Millisecond pulsars as clocks

Unlike normal pulsars millisecond ones display far smaller slowdown rates giving a time scale comparable with the best atomic clocks. Actually, millisecond pulsars have been measured to lose only one period in 10^{19} proving to be extremely accurate clocks.

Other applications

Apart from all the above, pulsars give people the opportunity to carry out a long series of projects that demand extreme precision. For example pulsars may, in the future, serve as gravitational wave detectors.

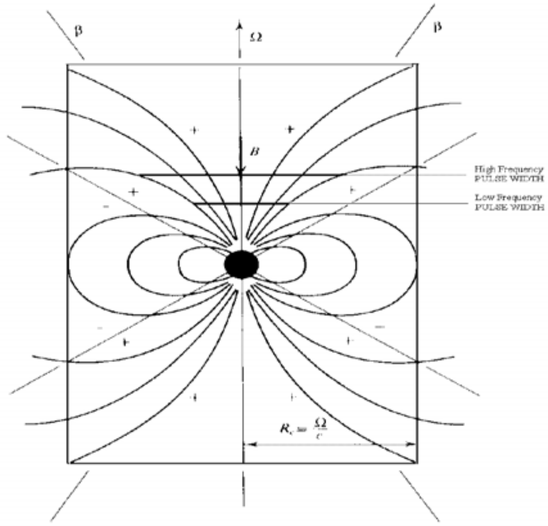

Figure 1.18: The dipole field configuration.

They may also be used to measure the gravitational constant G or even provide a time standard. Hopefully, we will be here to enjoy all this.

Chapter 2

Introducing Our Project

2.1 A Brief Revision

Let us recall the basic points related to the emission mechanisms occurring at neutron stars.

2.1.1 Generalities

Pulsars are fast rotating and extremely magnetized neutron stars constantly converting rotational kinetic energy into radiation. The observed slowdown rate is attributed exactly to this energy expense.

According to the most contemporary theories, the radiation emitted from pulsars is believed to occur in two different locations [Lyne and Graham-Smith, 1998]. The *polar cap* where the radio emission is taking place. The *outer magnetospheric gap* where the high energy emission originates from (optical, x-rays, gamma-rays).

As for the radio regime, which we are interested in, we should recall the following. Radio is emitted as charged particles are being accelerated along the magnetic field lines. The radiation is coherent, polarized synchrotron one. The most accepted idea is that of the conical beam. That is, the radio signals are emitted on a cone with its axis parallel to that of the magnetic field. The geometry of pulsar beams is shown in Figure 2.1.

The particular shape of an individual pulse received can be interpreted as the result of the line-of-sight trajectory tracing the beam cross section. The variation that emerges from observation of individual pulses disappears as soon as we average a sufficiently large number of them to obtain the integrated profile which, as mentioned earlier (Section 1.4.2), is unique for each pulsar and can be taken as its fingerprint for a particular frequency. There is a link between individual pulses and integrated pulse profiles that is best described by Lyne and Smith [Lyne and Graham-Smith, 1998]. They state:

> The integrated profiles are made up of very varied individual pulses, each of which may have more than one component: it is the statistical distribution of these components over a range of longitude, combined with their characteristic width and the probability distribution of their intensities that determine the repeatable shape of the integrated profile.

2.1.2 Structure of the emitting region

So far, we have avoided to mention anything relative to the exact structure of the emission region. Because our project involves this specific topic, a more accurate reference appears to be necessary.

Nowadays, two different phenomenological models are trying to interpret the observed integrated shapes of radio pulse [Lorimer, 1999]. Figure 2.2 illustrates the idea hidden behind each one of them.

The *core-cone* model depicts the beam as a core surrounded by a series of nested cones [Rankin, 1983]. In this case, each component corresponds to the intersection of the line-of-sight with a particular region of either the cone or the inner or the outer cone.

The *patchy-beam* model has the beam populated by series of emission regions [Lyne and Manchester, 1988]. That is, the emitting material is in the form of bunches of particles. In case one of these regions is on the observer's line-of-sight a component appears.

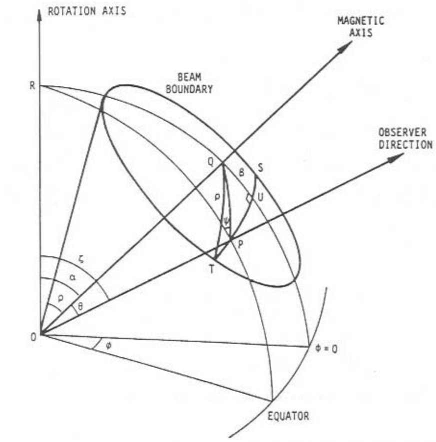

Figure 2.1: The geometry of pulsar beams.

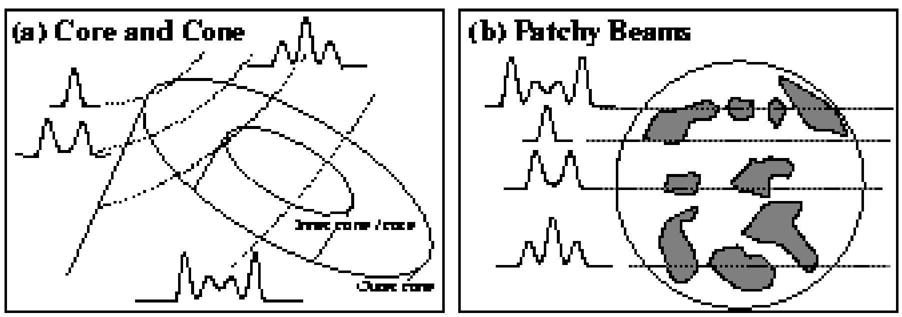

Figure 2.2: Several possible profiles that could be observed with respect to the specific line-of-sight trajectory.

2.1.3 A method to map the emitting region

In the above discussion, we assumed that the distance of the observed emitting region from the surface of the star is constant. Figure 1.15 illustrates the configuration of the magnetosphere around a neutron star. As shown there, if it was possible to 'look' at different depths into the cone-like beam, we should perceive changes in the angular distance of integrated pulse components since the actual distance between the radiating regions would decrease with increasing depth. The expected changes depend on the strength of the magnetic field since the curvature of the field lines is a function of B (see Section 2.1.4).

Hence, the above discussion reveals an adequate method regarding the study of the emitting region's topology. That is, studying the evolution of several features of the emitting region, beamwidth for example, over a depth range would provide us with important information about its configuration. Therefore, the crucial question would be:

> "Is it possible to look at selectively different depths into the cone?"

The answer is fortunately "Yes!".

It is well known that the depth into an emitting body where the observed radiation originates depends on the *optical depth*, which is a function of the observing frequency. For instance, when we 'look' at the surface of the moon with a receiver operating at 10 GHz, we do not really 'see' its optical surface but a layer a few centimeters deeper. In fact, this was the method used in the study of the lunar surface before a manned space craft was sent to land there.

In summary, different observing frequencies correspond to different depths so that high frequencies reveal regions deeper in the cone than lower ones. Therefore, we would expect regularities in the change of particular properties of an integrated profile observed at different frequencies. Apparently, such regularities would be consistent to the magnetic field configuration.

2.1.4 Frequency dependence of the pulse profile

From both observational and theoretical perspective, people have been trying to figure out what happens at the polar cap. This is reasonable because a knowledge of that sort would be necessary for the construction of a reliable model.

A huge volume of work has been done in the field of pulse profile's dependence on frequency. Such studies appear to be very illuminating since their correlation with polarization studies can provide invaluable information concerning the structure of the emitting region. From all the so far proposed ideas we will only focus on what is observationally proved to describe the evolution of beamwidth over frequency.

Assuming an aligned rotator and after rather simple calculations one may reach a relation between the beamwidth and the observing frequency. From the observational point of view it has been deduced [Lyne and Graham-Smith, 1998] that for most individual pulsars the above relation below 1 GHz, is of the form:

$$Beamwidth \propto f^{-1/4} \tag{2.1}$$

With f being the observing frequency. Nevertheless, we should point out that such studies involve many parameters which are not well established. For example, the relation between the observing frequency and the associated distance from the surface of the star, is not well known.

What is very interesting in the context of the present work, is a theoretical proposition made by Professor F. G. Smith during personal communications [Smith, 2000]. According to Professor Smith it is possible to give a theoretical relation between the beamwidth, θ, and the frequency f. In what follows we present this theoretical relation and in paragraph 2.2.1 we describe how this relation happily led to the extension of the initially scheduled work. Let us follow his idea.

The magnetic field lines diverge as:

$$\theta \propto r^{1/2} \tag{2.2}$$

Where, θ is a measure of beamwidth and r the distance from the surface of the star. If, therefore, we assume a very general relation between θ and f, of the form:

$$\theta \propto f^{-\beta} \tag{2.3}$$

Then :

$$f \propto r^{-1/2\beta} \tag{2.4}$$

Let us try to estimate the crucial parameter β. For dipole radiation, the inductance of the magnetic field is reduced according to:

$$B \propto r^{-3} \tag{2.5}$$

as a function of r. On the other hand, if we assume that the frequency of radiation corresponds to the *gyrofrequency* of electrons radiating in a magnetic field of inductance B, we get:

$$2\pi f = \frac{e}{m}B \tag{2.6}$$

or

$$f \propto B \tag{2.7}$$

Therefore, we expect $\beta = 1/6$. Hence, the relation between the beamwidth of the emission, θ, and the frequency, f, becomes:

$$\theta \propto f^{-1/6} \tag{2.8}$$

It is expected that such a relation holds for the width of the integrated profile, as well as the width of the individual components of pulsar profiles.

If instead of the gyrofrequency relation we assume a more general one of the form $f \propto B^{\,n}$ (rather than $f \propto B$), then the relation under investigation, becomes:

$$\theta \propto f^{1/6n} \tag{2.9}$$

The examination of the above estimation is one of our aims as we discuss later.

2.2 Our Project's Description

Keeping ourselves aware of all the above, we are in the position to explain the main points of our project.

2.2.1 Our aim

Let us go straight to the statement of our aim. Explanations will be given immediately after that.

The initial aim

Given the frequency dependence of the integrated pulse profile on the observing frequency, as it is proved via previous extended studies (see Section 2.1.4), we regarded important to examine the following question:

"Do the observed changes of the pulse profile happen rapidly or do they happen gradually?"

In case we observe rapid changes, there exist two alternatives. Either **B** undergoes a fast change, or an emission mechanism peculiarity is involved.

If the profile's changes happen smoothly over frequency then it is rather impossible for an emission mechanism characteristic to be the reason.

Translating the above into the language of actual study one would underline the following. Using closely sampled observing frequencies we obtain integrated profiles as stable as possible. That means, profiles made of number of individual pulses large enough to ensure the stability of the profile for the given frequency. Successively, we go through an estimation of characteristic features of the profile for each different frequency. Finally, we plot the evolution of each feature over the available frequency range and examine if the changes happen fast or slowly.

Important notice

Apparently, the above investigation requires observations at as many closely sampled frequencies, which would not overlap with each other, as possible.

During the summer of 1992 a series of observations had been carried out at Effelsberg under the title "Five Frequency Project". The selected pulsars were observed at 1315, 1420, 1510, 1615 and 1710 MHz. Certainly, a motivation for that project, among others, was the present study.

Unfortunately, data reduction revealed the lack of high quality data. That is, not often the signal-to-noise ratio was high enough to guarantee reliable results. A more detailed discussion about this topic is included later.

The additional project

The theoretical model discussed in paragraph 2.1.4 made it obligatory to survey the uniform pulsar data base at Jodrell Bank in order to include additional data for the pulsars under study. Soon we realized that the observing frequencies there were not as closely sampled as to perfectly support our study.

Nevertheless, we went on compiling data that were used in order to extend our study. That is, we concluded that it would be interesting to carry out a broadly sampled frequency study for the specific neutron stars under examination. Moreover, we tried to fit models to the observational data in order to decide whether the orthogonal rotator model, proposed by Smith [Smith, 2000], is consistent with the observations. For this very issue we should sincerely thank Professor F. G. Smith with whom personal communications were more than exciting. Professor Smith carried out the calculations we presented in paragraph 2.1.4, personally.

Of course, studies of the frequency development of pulsar profiles has been done before for some pulsars; but, nevertheless we regarded a careful extension to our project, in order to examine the proposal made by Professor Smith, as very useful.

2.2.2 Attempting to reach our aim

Section 2.2.1 implies that in order to reach an answer to our question we should investigate the frequency evolution of several properties of the integrated profile. And because the depth where the observed signal originates from is a function of the observing frequency, any correlation between such a property and the frequency will be equivalent to a relation between that property and the observed depth. Hence, the frequency evolution of a property is, in terms of physical meaning, the evolution of the emitting region configuration over a depth range. What is necessary then for an approach to our aim is to establish a set of properties whose relation with frequency should be examined.

The first correlation to investigate would be that between frequency and **pulse width** (whatever its definition is). The deeper we 'look' in the cone, the narrower its cross section is. Further, we would expect a frequency dependence of the **separation of peaks** for reasons similar to the above. Finally, the relation between frequency and the **ratio of peaks of individual components** was also studied. The driving force for this study originates from the assumption that different components possess different spectral indices. Specifically, Rankin proposed that the core component has a more steep spectrum than the conal ones [Rankin, 1983]. This very issue has been further investigated and confirmed by Lyne and Manchester [Lyne and Manchester, 1988].

What we have studied in the present project is the evolution over frequency of the three properties mentioned above. That is, we investigate the frequency dependence of:

- Pulse width at 50% of peak flux ($W_{50\%}$).
- Pulse width at 10% of peak flux ($W_{10\%}$).
- Pulse equivalent width (W_{eq}).
- Angular separation between flux peaks.
- Ratio between flux peaks.

It is important to point out that the above features have been studied for both cases; For closely sampled frequency (data from Effelsberg) as well as for broadly sampled ones (data from Jodrell Bank).

2.3 Resources

2.3.1 Data resources

As we mentioned in the previous Section, the present work's aim is the study of frequency evolution of several specific integrated profiles' features. Therefore, the first requirement was to find pulsars observed at a sufficiently large frequency range. Initially, this demand restricted our options only to pulsars observed during the so-called "Five Frequency Project".

Obviously, it has been of great importance to obtain stable profiles for each particular pulsar that we studied. That meant that the number of pulses averaged for the construction of each profile was carefully selected to consist of a sufficiently large number of single pulses. This was a second reason for our options to be further limited.

Moreover, the nature of our project demanded as high signal-to-noise ratios as possible. This need emerged mainly from the fact that two of the parameters of our study were the separation and the ratio between components. Hence, profiles of high signal-to-noise ratios are necessary for estimations of the height and the location of a flux peak. Reasonably, this introduced an additional restriction.

Fortunately, the last two requirements are satisfied together. Given that noise is a random phenomenon, it is clear that the more numerous the averaged pulses are, the smaller the noise fluctuations in intensity become. This results from the fact that the median of a number of random fluctuations around a constant value, approximates that constant value when their number goes to infinity.

In the present study the data used were selected from a large body of observation obtained either with the 76-m Lovell Radio Telescope (Figure 2.3) at Jodrell Bank Observatories (University of Manchester), or the 100-m Effelsberg Radio Telescope (Figure 2.4) near Bonn (Max Planck Institute for Radioastronomy).

In general, the frequency range was from about 1315 MHz up to 1710 MHz for the Effelsberg Radio Telescope data and from roughly 200 MHz up to 4850 MHz for the Lovell Radio Telescope.

Actually, the data compilation was separated into two steps. At first we compiled data from the Effelsberg Radio Telescope taking into account all the restrictions stated in the above discussion. In a second step we tried to increase the number of available frequencies (for the already selected pulsars) with data from the Lovell Radio Telescope. In other words, the available records at Effelsberg guided us to the selection of the final group of pulsars to be studied. The reason for setting this criterion was the better time resolution that in general characterizes the observations at Effelsberg.

In most cases, although the available number of pulses was sufficiently large, the compilation of good quality profiles was not as trivial as it may appear at first. The difficulties aroused from the low intensities that usually pulsars emit.

In Table 2.1 we present the main characteristics of the pulsars that finally 'passed our tests'. The information is extracted from the textbook Pulsar Astronomy [Lyne and Graham-Smith, 1998]. In the Notes field G stands for 'Glitch activity'.

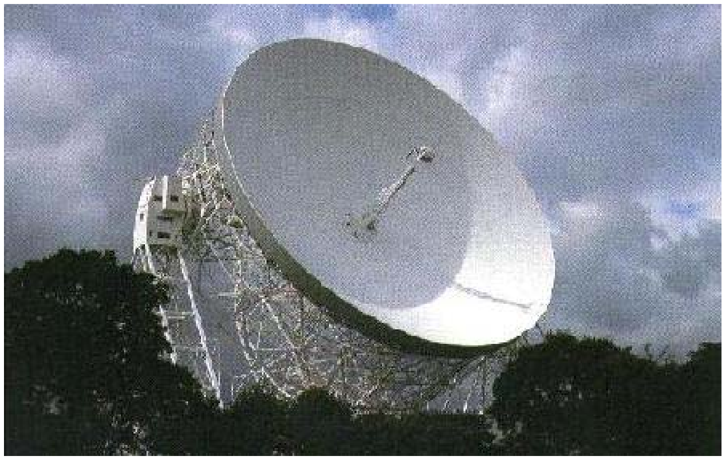

Figure 2.3: The 76-m Lovell Radio Telescope (Jodrell Bank Observatories).

Table 2.1: The compilation of pulsars we have studied.

B name	J name	l	b	DM	Distance	P	Notes
		deg	deg	cm^{-3} pc	kpc	ms	
0525+21	0528+2200	183.9	-6.9	51	2.3	3745.521	G
0540+23	0543+2329	184.4	-3.3	78	3.5	245.974	
0740-28	0742-2822	243.8	-2.4	74	1.9	166.761	
1702-19	1705-1906	3.2	13.0	23	1.2	298.987	
1742-30	1745-3040	358.6	-1.0	88	2.1	367.427	
1822-09	1825-0935	21.4	1.3	19	1.0	768.979	
1831-04	1834-0426	27.0	1.7	83	2.3	290.108	
1929+10	1932+1059	47.4	-3.9	3	0.2	226.518	
2319+60	2321+6024	112.1	-0.6	95	3.2	2256.488	

2.3.2 Software resources

Programs used

Several software packages served as tools for the present work. In the following we give a brief description for their usage during the analysis. The programs mainly used, are:

1. **jhspuls**: Pulsar data reduction program (Unix/VMS-Version, Last modified 4 August 1998).

2. **bfit**: Fitting program (Version 2.0).

3. **psrprof**: Pulsar profile analysis program (Version 5.1).

4. **gnuplot**: General plotting program (Unix-Version 3.7, Last modified 7 May 1999).

jhspuls was initially used for the pulsar data reduction from Effelsberg. All the integrated profiles constructed with Effelsberg data, are produced by it. This program was developed mainly by J.H. Seiradakis with the contribution of W. Sieber, A. Sievers, A. Jessner and M. Kramer. During our project **jhspuls** could handle only EPOS format. Recently it has been modified by J. H. Seiradakis and A. Noutsos to read EPN format as well [Seiradakis and Noutsos, 2000].

The reduction of data obtained with the Lovell Radio Telescope was done with **psrprof**. The way that it was used during the actual work was similar to that of **jhspuls**. It served as a tool to investigate the data base at the Jodrell Bank Observatories and successively to construct each integrated profile.

Probably the most important tool for our study was **bfit**. It was used to fit a set of gaussians to a given profile in order to obtain the widths ($W_{50\%}$,$W_{10\%}$ and W_{eq}). Moreover, it was used to estimated the height (P_i) and the center (C_i) of each flux peak. It has been developed by Dr M. Kramer [Kramer et al., 1994].

Figure 2.4: The 100-m Effelsberg Radio Telescope (Max Planck Institute for Radioastronomy, Bonn).

To conclude with, **gnuplot** served as a standard plotting package as well as a tool for fitting models to our observations. All the plots that follow in this text have been produced with it. **gnuplot** is supported by both UNIX and Linux operating system.

Software peculiarities

The experience gained by the usage of the software discussed previously, allows us to make some comments regarding their reliability. As for the data reduction packages (i.e. **jhspuls** and **psrprof**), we take the opinion that any of the trivial hints we encountered was due to the specialization of our project. In fact, this is expected in the field of a scientific project. Especially, when different observing systems and recording configurations have been used.

Similarly, **bfit** has not displayed any bugs. The only exception involves the case in which one tries to fit a profile that has a precursor. If gaussians are necessary to fit side components, then a well known problem in the estimation of widths emerges. From the very beginning of our actual analysis we were aware of that. So, we have been carrying out very careful examinations of the profiles in order to become absolutely sure that our results are reliable.

2.4 Analysis Procedure

Up to now we have made clear what we intend to study. However, the exact analysis procedure we followed has not been mentioned yet. In the following we trace back in the most important steps we have made.

2.4.1 Terminology

To begin with, we should establish a terminology that will be used throughout this document.

It should be noted that whenever the term *component* is referred to in the text, it is used to indicate a visually identifiable flux peak. The term *component* is not related in the present work with anything else than that.

During the study of this report the reader will often come across two quantities related to each component. The first is its center which will be indicated as C_i (stands for the $Component_i$) where i is an index to distinguish between several components in the same profile. That index has the value of 1, 2, 3 etc. We

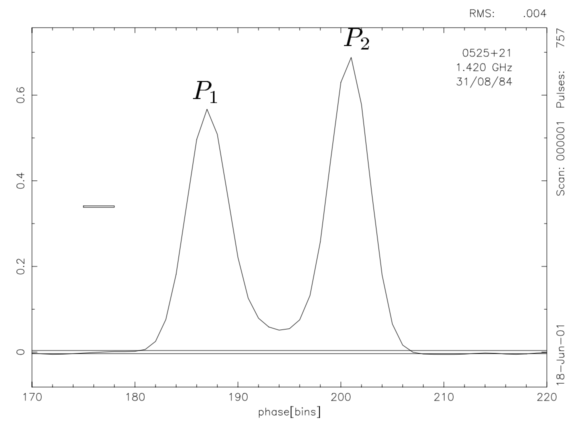

Figure 2.5: Step 1: Averaging the profiles with the highest signal-to-noise ratio, we construct the integrated profile which will be under investigation. Above, a 1420-MHz observation is illustrated. For the construction of this profile 757 single pulses are averaged.

always count from left to the right of the visually inspected profile. The second is its height in terms of flux density represented by the symbol P_i (stands for $Peak_i$).

Whenever two adjacent components are separated by a region of low flux density which is clearly identifiable, we call this region *Bridge*. Its position is declared with the symbolic name C_{Bridge} and its height with the name P_{Bridge}. Figure 3.2 illustrates the above terminology.

2.4.2 An example

Before proceeding to the discussion of the error estimations (Section 2.4.3), it would be useful to provide the reader with a brief virtual analysis process considering all its steps. The example illustrates the study of PSR B0525+21.

Step 1 : Data selection

The first step is to select the appropriate profiles. In other words, for each given frequency we collect the profiles of the highest signal-to-noise ratio among all the available ones. Averaging all these individual profiles together we construct the "stable" integrated one as presented in Figure 2.5. This profile not only is characterized by stability, but by the relatively high signal-to-noise ratio, as well. At this step we use either **jhspuls** or **psrprof** for data from Effelsberg or the Lovell Radio Telescope respectively.

Step 2 : Calculations

After having completed *step 1* for all available frequencies, we continue with the calculation of $W_{50\%}$, $W_{10\%}$ and W_{eq}. This is achieved by using **bfit**. Figure 2.5 illustrates the profile which we pretend we are interested in studying. It is important to note that in all cases our data were smoothed with smoothing parameter in **bfit** set to 1. Then, following the procedure described by Kramer, Wielebinski, Jessner, Gil and Seiradakis [Kramer et al., 1994] we fit to our profile a collection of gaussians.

The fitting range is carefully selected to be of the same length for all profiles. After having reached a satisfactory approximation of the actual data, it is trivial to calculate the widths. **bfit** can automatically calculate them using the fitted profile. Figure 2.6 presents the result of our fitting procedure.

At this step we also estimate the height and the center of the components. This is done using **bfit** once again. The fitting range is set to cover only two to four phase bins about the visually selected center of the peak and subsequently a gaussian is fitted. Figure 2.7 makes clear the idea. The parameters characterizing that gaussian are assigned to the peak.

Step 3 : Study

Although the above two steps may appear to be trivial, they were the most time consuming since the accuracy of the present work is closely related to that of the above calculations. Once we felt confident with the results of the previous steps (testing the estimated values by careful inspection of the profiles), we would go on to

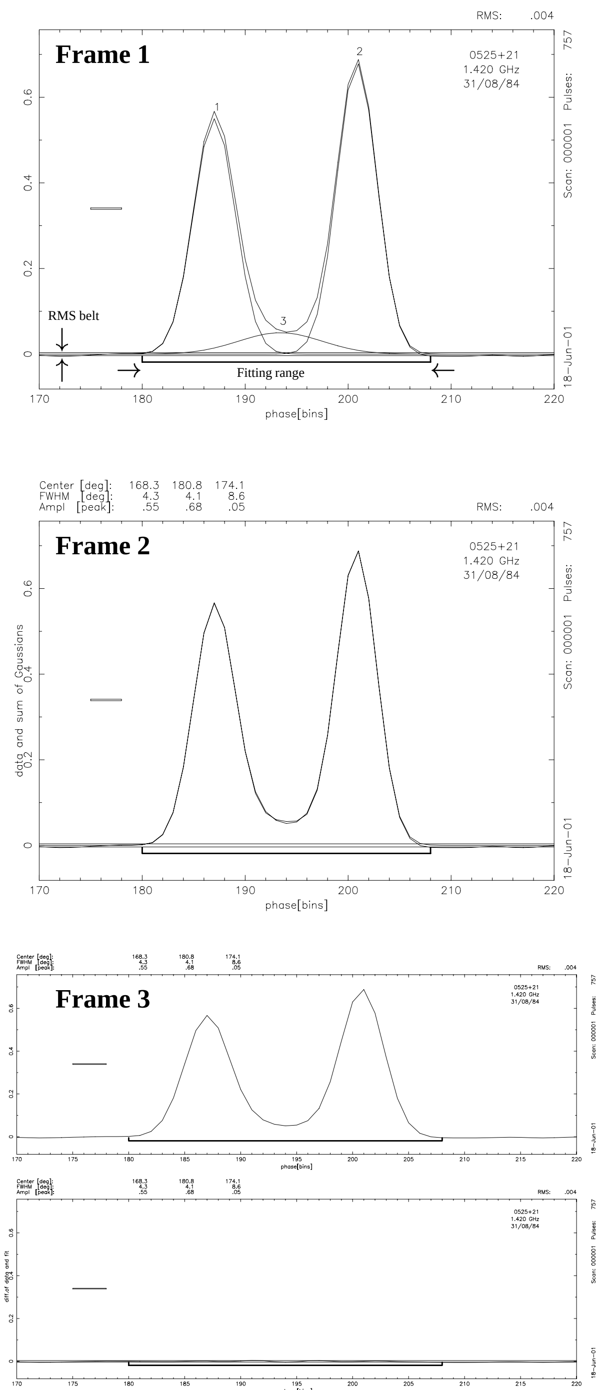

Figure 2.6: Step 2.a: Above, the fitted set of gaussians is plotted. The *fitting range* and the *RMS belt* are also indicated. **Frame 1**: The set of gaussians is shown together with the actual data. The parameters characterizing the gaussians, are the ones obtained with the fitting algorithms supported by **bfit**, that is the ones that correspond to the smallest difference between the actual data and the fitted profile (i.e. the sum of the gaussians). **Frame 2**: The actual profile is superposed to the sum of the set of gaussians. Obviously, the two curves fit together enough accurately to be indistinguishable. **Frame 3**: In the upper plot, the actual profile is shown. In the lower, the post-fit residuals are shown. Notice that the residuals' curve is within the RMS belt along the whole fitting range.

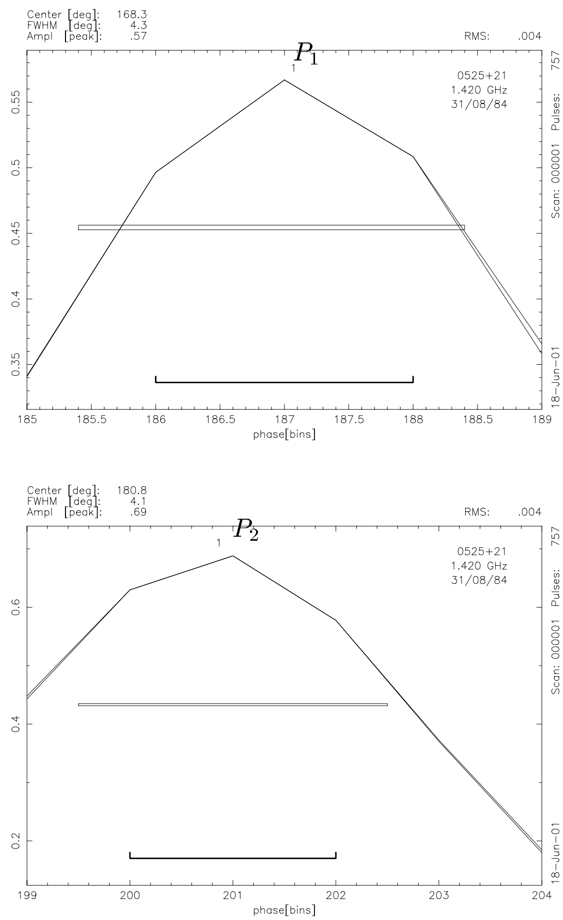

Figure 2.7: Step 2.b: At this phase we measure the height (P) and the center (C) of each individual component. This is by fitting a gaussian to each flux peak. The fitting range is only a few phase bins long (two in the example we present) in order to cover the immediate vicinity of the flux peak. It is worth to notice that the fitted gaussian is difficult to be distinguished from the actual data within the fitting range.

plot the observational points and fit the suggested models. This was carried out by **gnuplot** which uses the Marquardt-Levenberg fitting algorithm.

2.4.3 Error estimation

Obviously, the most substantial part of a study based on observations is the estimation of the errors in each calculated quantity. This is what allows us to test the correctness of the assumptions we have made in order to reach a certain conclusion and how reliable these are. Moreover, it is the errors which indicate the model that could be reasonable to be fitted over a given collection of observational points. Therefore, the present paragraph should be treated very carefully.

The error in separation and width

An entity that often appears in our text, is the *phase bin*. This very concept is the first thing we should discuss regarding the errors estimation. In order to study a source of electromagnetic radiation, we observe the photons it emits and record the intensity they 'carry'. Fundamentally, this is the idea hidden behind the observation of a pulse profile as well. It is expected that the pulse profile of a pulsar consists of an infinite number of points, each one of which is associated to an instant measurement of the received intensity. But this is not the case. What is really happening is an integration of intensity over a constant time interval (the *phase bin*). In other words, the observing system integrates the intensity (or number of photons) that reach the antenna during the time span of a *phase bin* and then records it in the storage means. Hence, a pulse profile is not a smooth curve composed by innumerable points. Figure 2.8 presents the above idea.

It is becoming clear now that the first uncertainty we have to consider is that associated with the center of a component. Indeed, it is not trivial to decide where the peak is located. It could be either at the extreme left of the associated bar or at the extreme right. Therefore, the error of the position of a given point in our pulse is equal to the phase bin length.

To be more precise, we should mention that the above determines the error only if the dispersion effect is absent from our observations. But this is not true. In fact the error in the position of a point on the profile, Δt (in terms of time), is:

$$\Delta t = \sqrt{\Delta t_{DM}^2 + \Delta t_s^2} \tag{2.10}$$

where Δt_{DM} is the error due to the dispersion effect and Δt_s is that due to the sampling rate (the one we already referred to as 'phase bin length'). Usually, the data are absolutely free from dispersion and hence the first term of that equation is negligible.

Given the above equation, what is the error in the separation of two components? Applying the error distribution formula on the function S that describes the separation, one can easily find:

$$\Delta S = 0.7 \cdot \Delta t \tag{2.11}$$

So far we regarded dispersion effects as negligible. Actually, we took it into account during our errors estimation. The idea is as follows. Dispersion causes a profile lengthening by a time interval Δt_{DM} (in milliseconds), which is given by:

$$\Delta t_{DM} = 8.3 \cdot 10^6 \cdot DM \cdot \Delta f \cdot f^{-3} \tag{2.12}$$

Where, DM the dispersion measure, f the observing frequency and Δf the observing bandwidth.

After all the above calculations we decided that the error in the separation is given by Equation 2.11 with Δt being the longer between the sampling interval (Δt_s) and the dispersion broadening (Δt_{DM}). As for the widths, there is no need for further discussion since the widths can be considered as separations as well.

The error in ratio

Avoiding the details, we only give the formula used for the estimation of errors in the component ratios, r. The error in the ratio r between two flux peaks P_1 and P_2 is :

$$\Delta r = r \cdot \sqrt{2 \cdot (0.1)^2 + (rms/P_1)^2 + (rms/P_2)^2} \tag{2.13}$$

Where rms is a characteristic of the observation.

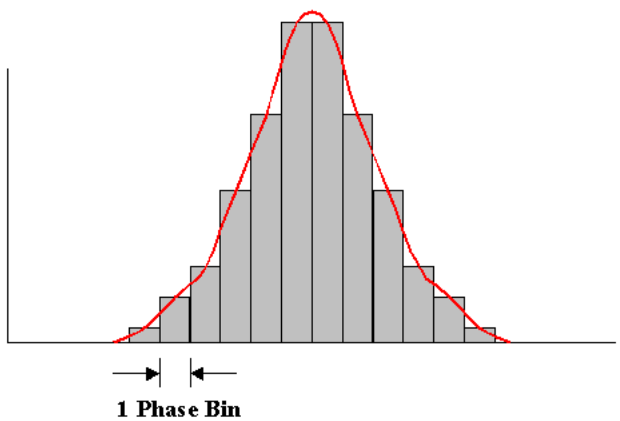

Figure 2.8: The phase bin concept. The red line describes what we would see with a data reduction program while the grey bars represent the actual data.

Chapter 3

Evolution over Broadly Sampled Frequency Range

This chapter serves as the report for the project based on broadly sampled frequencies. That is, based on data compiled from the Jodrell Bank pulsar data base.

Each Section is dedicated to an individual pulsar in ascending order of pulsar coordinates.

For each pulsar we try to examine if a power law is suitable to fit the observational points. In case this happens we also estimate the parameters characterizing the power law.

3.1 PSR B0525+21

In Section 2.2 we discussed several criteria for selecting a set of pulsars that would prove interesting to study. PSR B0525+21 not only satisfied such criteria but moreover played a crucial role in this project. This pulsar has been previously studied concerning the evolution of the separation between its components [Thorsett, 1991]. Therefore, it proved very useful to use this pulsar as a test for our analysis procedure.

Fortunately, we soon realized that PSR B0525+21 displayed a behavior which was very close to that of previous studies. Furthermore, it proved to be our best tool to observationaly test the theory put forward in the previous Chapter and compare its accuracy with previous projects.

3.1.1 General information about PSR B0525+21

PSR B0525+21 lays in the constellation of Taurus (Figure 3.1) at a distance of about $2.3\ kpc$ from us (its dispersion measure is $51\ pc \cdot cm^{-3}$). Its period is about $3.746\ s$ and its period derivative roughly $40.0321 \cdot 10^{-15}\ s/s$ giving a characteristic age of about $1.48 \cdot 10^{6}\ years$. Its mean flux density at $400\ MHz$ is about $57\ mJy$ whereas at $1400\ MHz$, about $9\ mJy$. In the past it has displayed glitch activity.

3.1.2 A discussion about profile morphology

As shown in Figure 3.2, PSR B0525+21 displays an interesting profile. It consists of two distinct components clearly separated from one another. From Figure 3.2 it is immediately obvious that a region of low intensity separates them. This region will be called hereafter ‘bridge’.

3.1.3 Integrated profile study

The integrated profiles used in the study of PSR B0525+21, were constructed by averaging large numbers of single pulses. Each individual observation was carried out with either the Effelsberg, or the Lovell Radio Telescope.

Although the total observing time dedicated to PSR B0525+21 was again significantly long, our profiles were not all satisfactory. In many cases the signal-to-noise ratios were low, implying the necessity of smoothing. Therefore, all the data were smoothed before being studied. The smoothing parameter in **bfit** was set to 1.

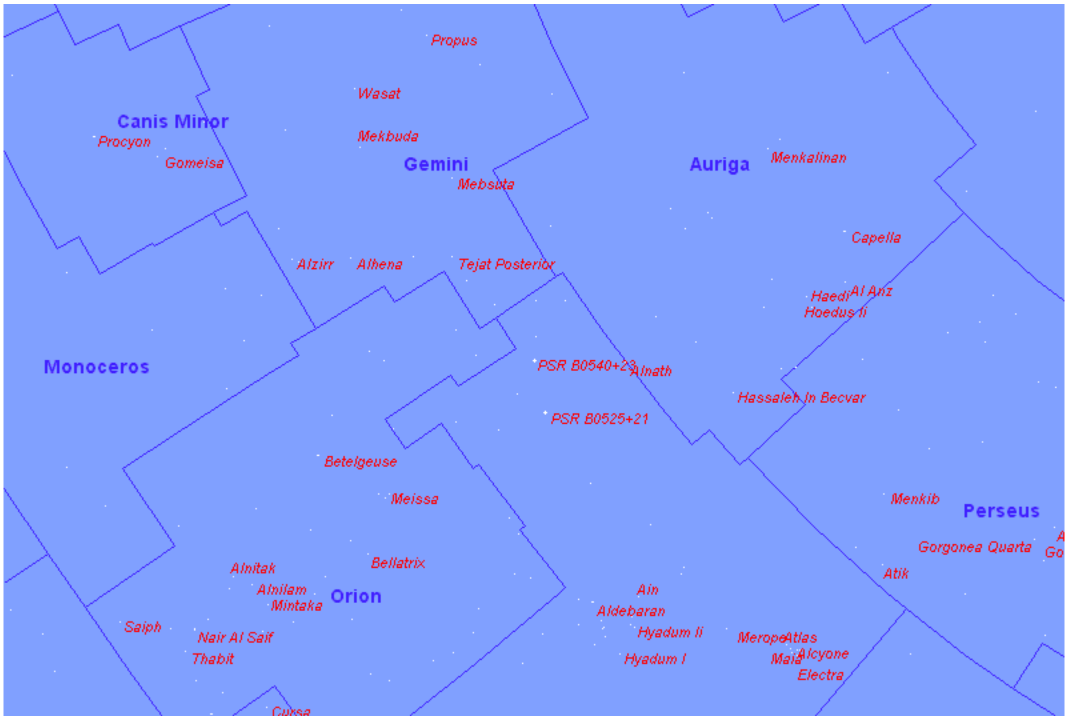

Figure 3.1: PSR B0525+21: Its location in the constellation of Taurus.

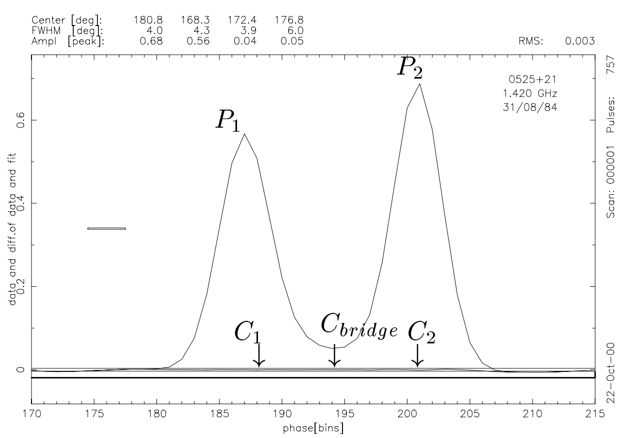

Figure 3.2: PSR B0525+21: Observed at 21 cm (1420 MHz). The terminology used in the text is also indicated.

Table A.1 contains all the values which are useful during the study of the analysis. As it is shown there, the data cover a frequency range from 408 up to $4850\ MHz$. Analytically, the frequencies used, are: 408, 606, 910, 1408, 1667 MHz (Lovell) and $4850\ MHz$ (Effelsberg).

In the following we present the study of the evolution of $W_{50\%}$, $W_{10\%}$, W_{eq}. Moreover, we study the separation between the two components and the ratio between their peaks. Because of the ambiguity in the definition of where the 'bridge' is located, we refrain from studying the ratio of each one of P_1 and P_2, over P_{bridge}.

Before proceeding to the actual analysis we should underline, that: Due to the lack of good quality data from Effelsberg, PSR B0525+21 was studied only for broadly sampled frequencies compiled from the Lovell Telescope. In other words, what we intent to do here is to test the hypothesis made in Section 2.1.4 by F. G. Smith.

Evolution of $W_{50\%}$

Figure 3.3 illustrates the evolution of $W_{50\%}$ over a broadly sampled frequency range for PSR 0525+21.

A quick look reveals that the data follow a clear regularity. The next step would be to search for a model to fit the data. A power law model of the form:

$$W_{50\%} = a \cdot f^b \tag{3.1}$$

gives:

$$a = 36 \pm 1\ \frac{Degrees}{MHz^b},\ b = -0.107 \pm 0.004 \tag{3.2}$$

Figure 3.4 presents both the data and the fitted model.

It would be very interesting to investigate the existence of a model of the previous form including the 4850 MHz point from Effelsberg. Figure 3.5 illustrates the result for the values:

$$a = 46 \pm 2\ \frac{Degrees}{MHz^b},\ b = -0.143 \pm 0.006 \tag{3.3}$$

We finally fit a model of the form $W_{50\%} = a \cdot f^b + c$ (a power law with an offset) for the last set of points. The estimated parameters, are

$$a = 52 \pm 49\ \frac{Degrees}{MHz^b},\ b = -0.078 \pm 0.176,\ c = -13\ Degrees \pm 64 \tag{3.4}$$

Figure 3.6 presents the results. From the previous equations it becomes clear that the uncertainty in the values of a, b and c, is huge. Therefore, we regard the former model (i.e. $W_{50\%} = a \cdot f^b$) as the most likely to represent the actual distribution of the present set of points.

Evolution of $W_{10\%}$

Studying the evolution of $W_{10\%}$ over frequency, gave similar results as for $W_{50\%}$. Again, tha data are regularly distributed.

In Figure 3.7 we display the observational points of the form $f - W_{10\%}$ obtained with the Lovell data alone. The regular behaviour is obvious. The power law that was fitted to the set of observational points, is described by the parameters:

$$a = 38\ \frac{Degrees}{MHz^b} \pm 2,\ b = -0.089 \pm 0.006 \tag{3.5}$$

The model plus the data are displayed in Figure 3.8.

Evolution of W_{eq}

The regular behavior we have met in the cases of $W_{50\%}$ and $W_{10\%}$ is also apparent, in the case of W_{eq}. Figure 3.9 indicates this point.

As Figure 3.10 shows, the approximation of our data with a power law appears to be accurate enough. The parameters a and b, are:

$$a = 35\ \frac{Degrees}{MHz^b} \pm 4,\ b = -0.194 \pm 0.019 \tag{3.6}$$

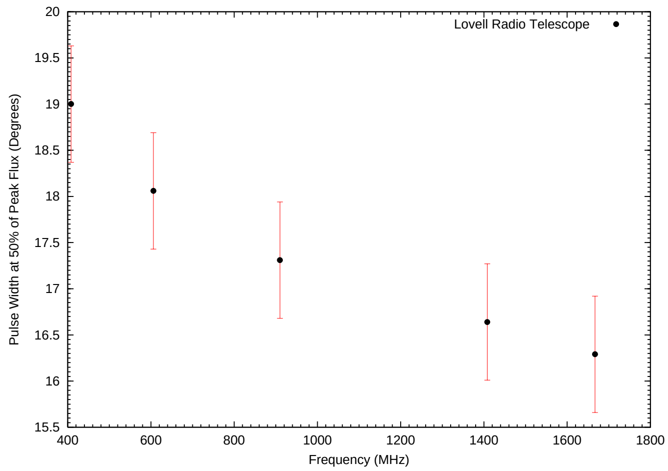

Figure 3.3: PSR B0525+21: the observational $f - W_{50\%}$ points. The data come from observations at broadly sampled frequencies (Lovell data).

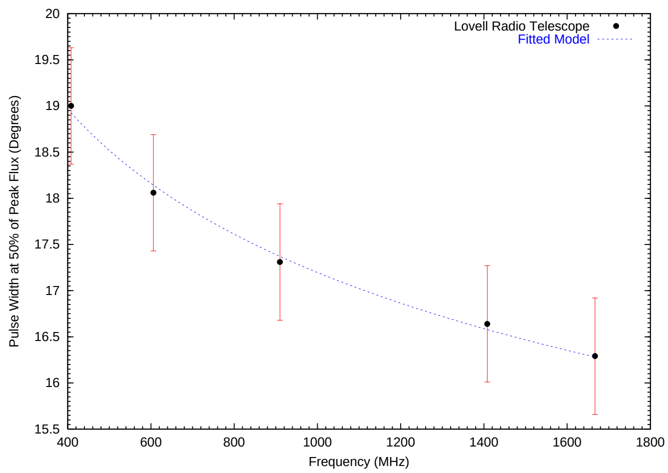

Figure 3.4: PSR B0525+21: the observational $f - W_{50\%}$ points together with the fitted model $W_{50\%} = a \cdot f^b$.

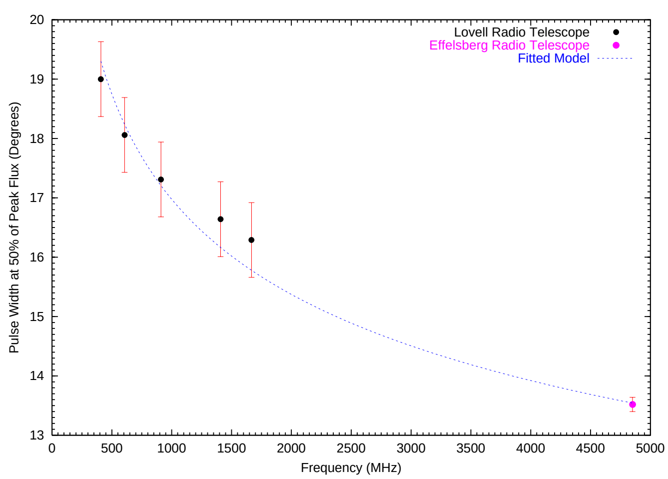

Figure 3.5: PSR B0525+21: the observational $f - W_{50\%}$ points together with the model $W_{50\%} = a \cdot f^b$. Effelsberg point at 4850 MHz is also present.

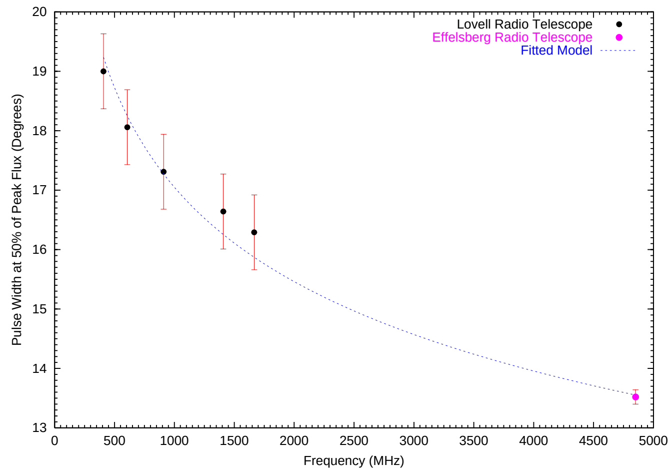

Figure 3.6: PSR B0525+21: the $f - W_{50\%}$ points together with the model $W_{50\%} = a \cdot f^b + c$. The Effelsberg point at 4850 MHz is also taken into account.

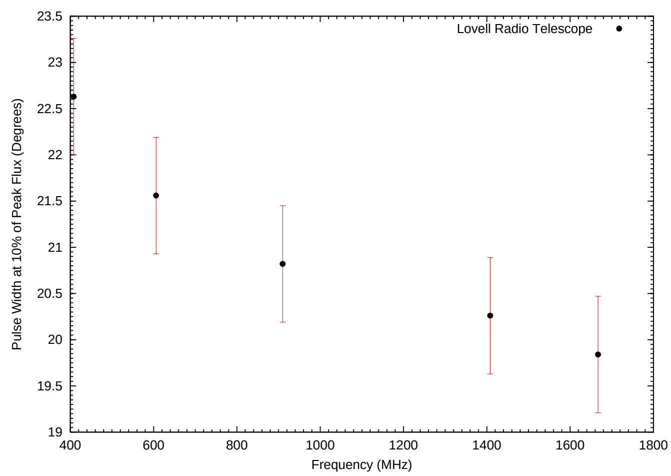

Figure 3.7: PSR B0525+21: the $f - W_{10\%}$ points as obtained with Lovell Radio Telescope.

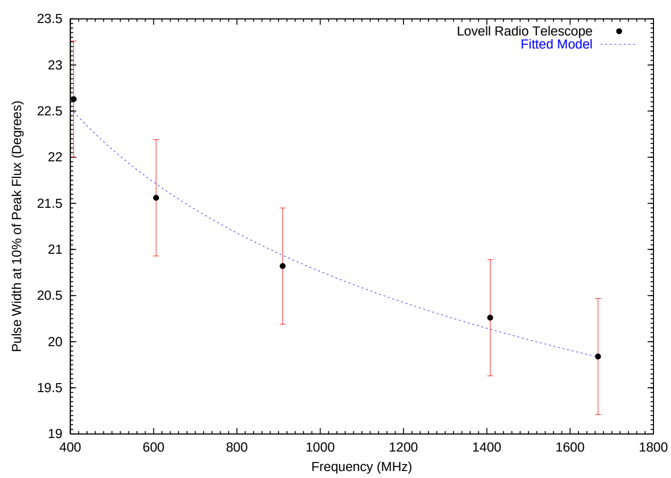

Figure 3.8: PSR B0525+21: $f - W_{10\%}$ points plus the fitted power law $W_{10\%} = a \cdot f^b$.

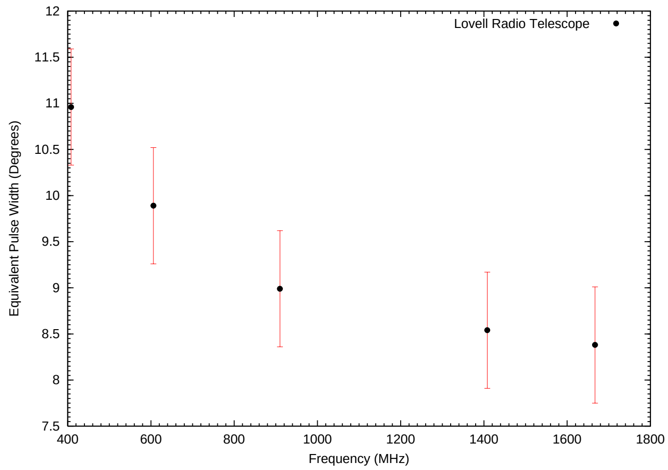

Figure 3.9: PSR B0525+21: $f - W_{eq}$ points (Lovell data).

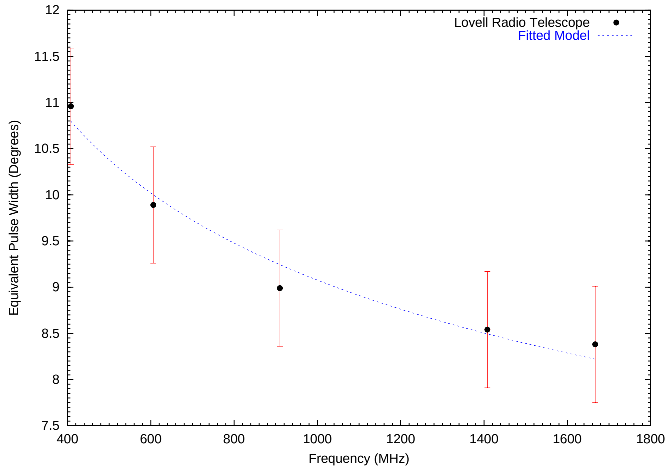

Figure 3.10: PSR B0525+21: $f - W_{eq}$ points in conjunction with the fitted power law.

After that, we tried to fit a power law with an offset. The values of a, b and c that we have calculated, are:

$$a = 1665 \pm 1564 \, \frac{Degrees}{MHz^b}, \; b = -1.03 \pm 0.169, \; c = 7.6 \, Degrees \pm 0.3 \tag{3.7}$$

The error in a is of course non-negligible. On the other hand, it is surprising how well the model fits to the points (Figure 3.11).

Calculations similar to the above that took into account the Effelsberg point as well (4850 MHz) proved to give very bad approximations.

Separation between C_1 and C_2

The regularity in the evolution of $Widths$ seems to be present here as well.

At first we tried to fit a power law ($C_2 - C_1 = a \cdot f^b$) to the Lovell data. In Figure 3.12 we present the results that corresponds to the following values of a and b:

$$a = 31 \, \frac{Degrees}{MHz^b} \pm 0.4, \; b = -0.127 \pm 0.002 \tag{3.8}$$

Undoubtedly, we have an interestingly precise approximation with errors only of the order of 1%! Of course that is something amazing.

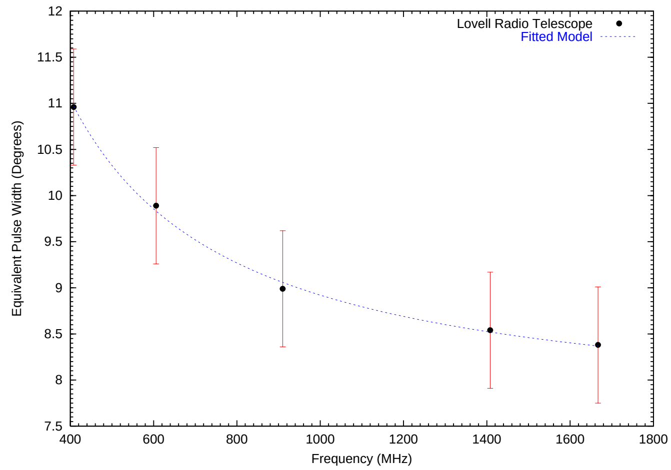

Figure 3.11: PSR B0525+21: $f - W_{eq}$ points in conjunction with the fitted power law with offset (Lovell data).

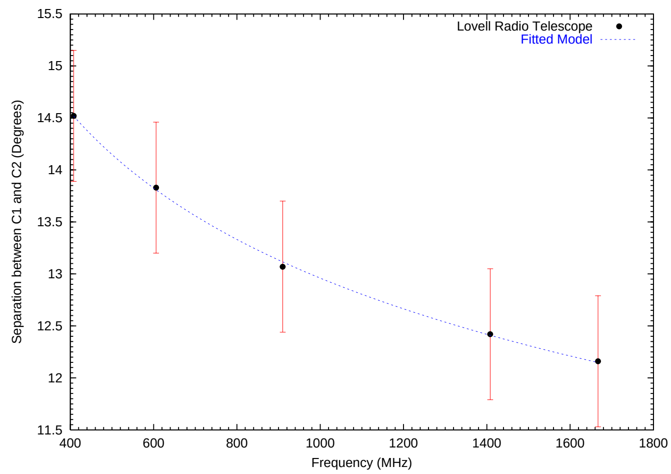

Figure 3.12: PSR B0525+21: evolution of $C_2 - C_1$ as observed with Lovell. The fitted model is a simple power law.

Then we fitted a power law with an offset to the same set of data. That is observations carried out with the Lovell Telescope. In Figure 3.13 we present the obtained plot. The parameters' values are given by:

$$a = 32\,\frac{Degrees}{MHz^b} \pm 4,\ b = -0.191 \pm 0.087,\ c = 4\ Degrees \pm 4 \tag{3.9}$$

Although the appearance of that plot is impressive, the errors in the estimation of a, b and c are large enough to prevent us from regarding the power law with offset a reliable model.

We repeated the two previous steps (power law and power law with offset) in the case that our Lovell data were corroborated with the $4850\ MHz$ observation from Effelsberg. Figure 3.14 illustrates the result. The best fit parameters, a and b, are:

$$a = 27\,\frac{Degrees}{MHz^b} \pm 1,\ b = -0.104 \pm 0.004 \tag{3.10}$$

In Figure 3.15 we present the calculations for a power law with an offset. The best fit values of a and b, are:

$$a = 55\,\frac{Degrees}{MHz^b} \pm 9,\ b = -0.376 \pm 0.037,\ c = 9\ Degrees \pm 0.3 \tag{3.11}$$

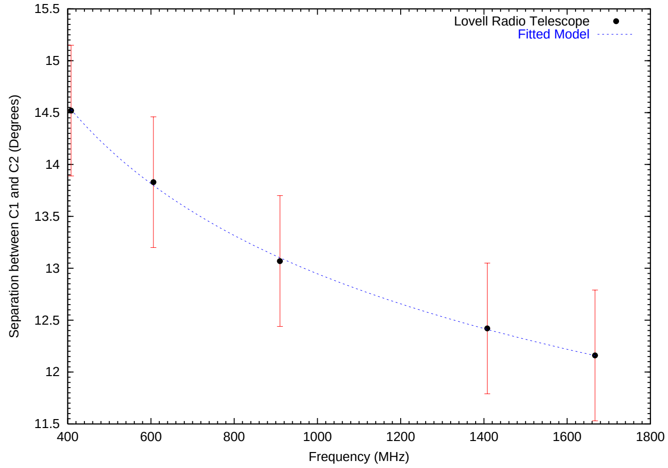

Figure 3.13: PSR B0525+21: evolution of $C_2 - C_1$ together with the fitted power law with offset.

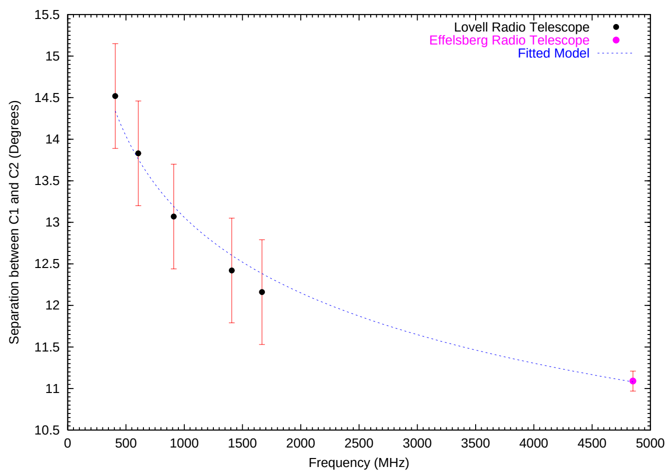

Figure 3.14: PSR B0525+21: the evolution of $C_2 - C_1$. The fitted power law is also shown. Here we took into account the 4850 MHz observation as well.

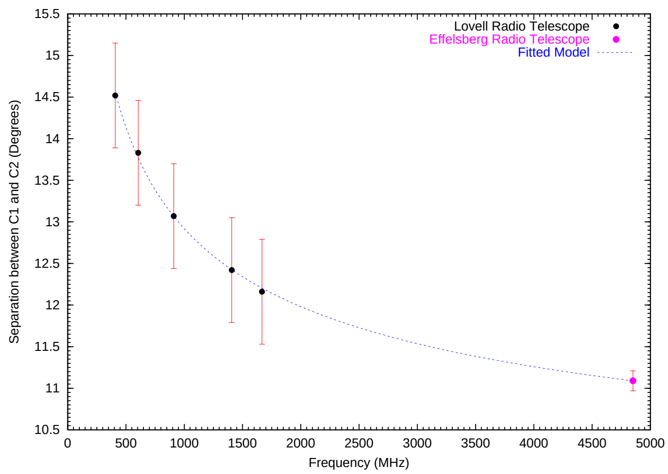

Figure 3.15: PSR B0525+21: evolution of $C_2 - C_1$, and the fitted power law with offset.

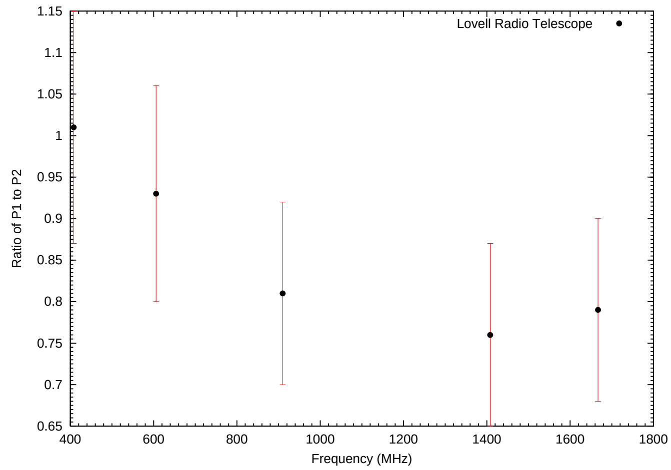

Figure 3.16: PSR B0525+21: The evolution of $P_1/P2$ over a broadly sampled frequency range (Lovell data).

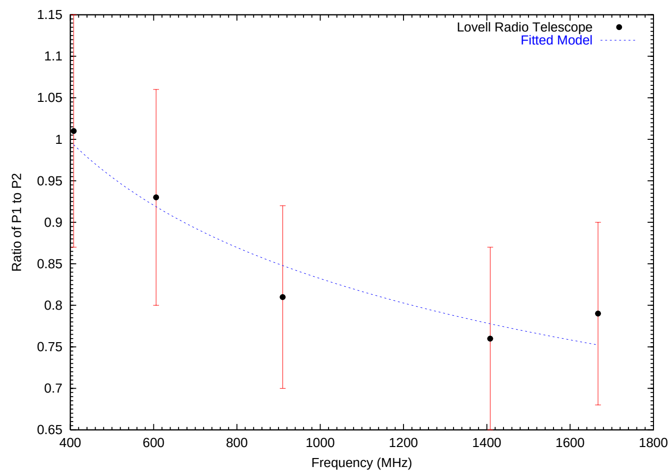

Figure 3.17: PSR B0525+21: The evolution of $P_1/P2$ over a broadly sampled frequency range plus the power law (Lovell data).

Evolution of ratio between P_1 and P_2

So far, PSR B0525+21 seems to exhibit an interestingly regular behavior. The evolution of P_1/P_2, is not an exception. In Figure 3.16 we present the distribution of the points that correspond to 408, 606, 910, 1408 and 1667 MHz. The parameters a and b for the power law in Figure 3.17, are:

$$a = 3\,\frac{Degrees}{MHz^b} \pm 0.8,\ b = -0.198 \pm 0.038 \tag{3.12}$$

Now, if we try to extend the frequency range adding the observation at $4850\ MHz$, the parameters become:

$$a = 4\,\frac{Degrees}{MHz^b} \pm 0.5,\ b = -0.217 \pm 0.020 \tag{3.13}$$

Figure 3.18 displays the resulted plot.

A brief discussion

From the above study it becomes clear that the development of the characteristic properties of PSR B0525+21, is interestingly regular. The power law appears to be suitable to describe the behavior of the data. Particularly, the separation $C_2 - C_1$ is very accurately described by the power law.

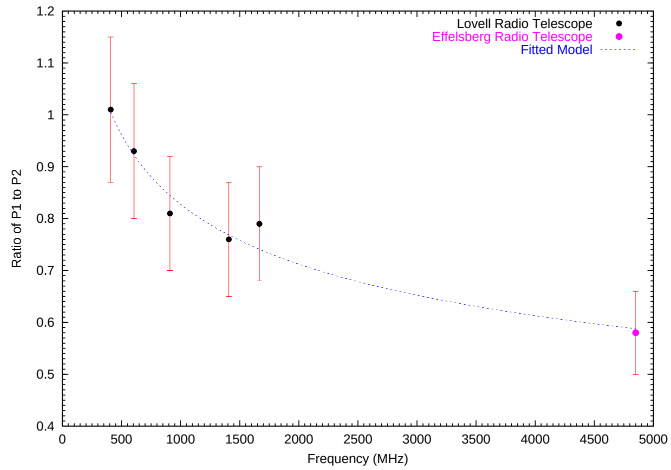

Figure 3.18: PSR B0525+21: The evolution of $P_1/P2$ over a broadly sampled frequency range plus the observation at 4850 MHz.

Nevertheless, the parameter b is not that close to the value 6, which is expected according to the theory proposed by Smith (see Section 2.1.4). The best approximation appears in the case of W_{eq} where this parameter is assigned the value 5.3.

3.2 PSR B0540+23

PSR B0540+23 does not possesses an extraordinary profile. It exhibits a rather simple profile that may consist of a number of "hidden" components. Figure 3.20 illustrates a typical observation at 21 cm.

3.2.1 General information about PSR B0540+23

PSR B0540+23 is located very closely to PSR B0525+21 (Figure 3.19). It is located 3.5 kpc from the Sun. Its dispersion measure is about 78 $cm^{-3}pc$. It rotates with a period of 245.974 ms. It displays a slowdown rate of about $15.4 \cdot 10^{-15}$ s/s which implies a characteristic age of roughly $0.25 \cdot 10^{6}$ $years$. Its mean flux density at 400 and 1400 MHz is 29 and 9 mJy respectively.

3.2.2 A discussion about profile morphology

Its profile morphology does not invoke any particular impression. In fact it represents very well the lighthouse model with a simple gradual increase in intensity that fades out after a while. This characteristic made it impossible to study anything else than the widths. Figure 3.20 presents a typical 21-cm observation.

3.2.3 Integrated profile study

The bad signal-to-noise ratio that characterizes observations with the Effelsberg Radio Telescope, prevented us from carrying out the closely sampled frequency project. Hence, we only studied observations obtained with the Lovell Telescope. Specifically, the used frequencies were: 410, 606, 926, 1376, 1412 and 1642 MHz.

Evolution of $W_{50\%}$

In Figure 3.21 the evolution of $W_{50\%}$ is presented. Although it displays a smooth behavior, the power law seems to be absent.

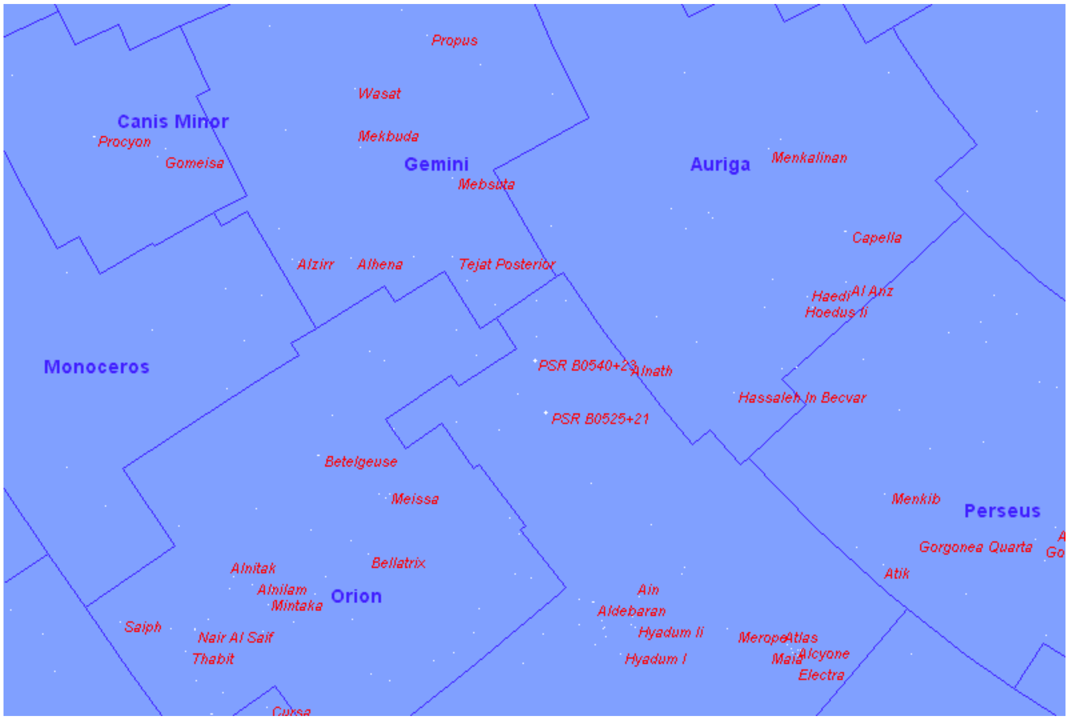

Figure 3.19: PSR B0540+23: its location in the heavens.

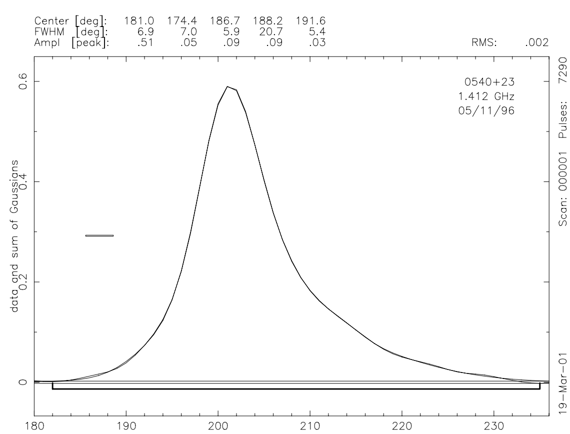

Figure 3.20: PSR B0540+23: A typical 21-cm observation.

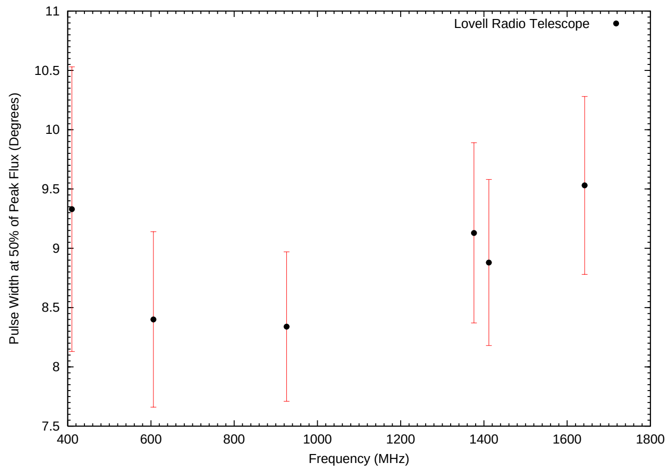

Figure 3.21: PSR B0540+23: The evolution of $W_{50\%}$ over a broadly sampled frequency range.

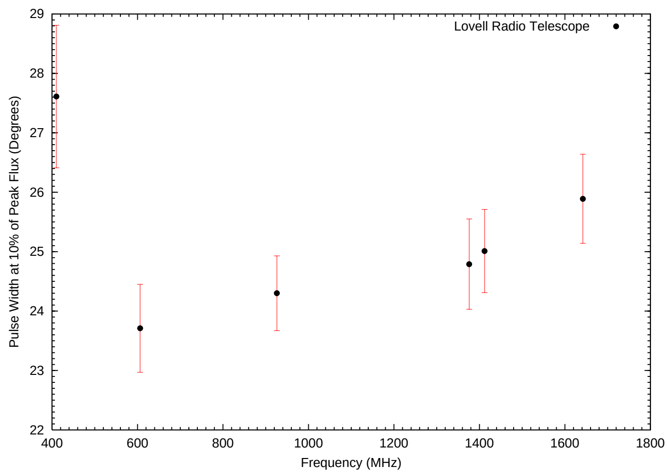

Figure 3.22: PSR B0540+23: The evolution of $W_{10\%}$ over a broadly sampled frequency range.

Evolution of $W_{10\%}$

Qualitatively speaking, the evolution of $W_{10\%}$, as shown in Figure 3.22, is very similar to that of $W_{50\%}$. Hence, no power law is present here and therefore we will not try to fit any model.

Evolution of W_{eq}

Once again, the correlation between frequency and $W_{50\%}$ seems to be of the same sort with the relation between frequency and W_{eq}.

A brief discussion

PSR B0540+23 may display a simple profile but we share the opinion that the above results are interestingly important, at least in a sense. That is, the fact that three characteristic features of an integrated profile seem to evolve following a qualitatively similar law, is a strong evidence for the correctness of the analysis method. Concerning the simplicity of the profile shape, we become even more confident for the reliability of our method since the possibility for a mistaken estimation of a property, is minimized.

On the other hand, an attempt to find a model, other that a simple power law, suitable for fitting the above distributions would be, at least, motivating. The regularity possessed by these points implies that there must

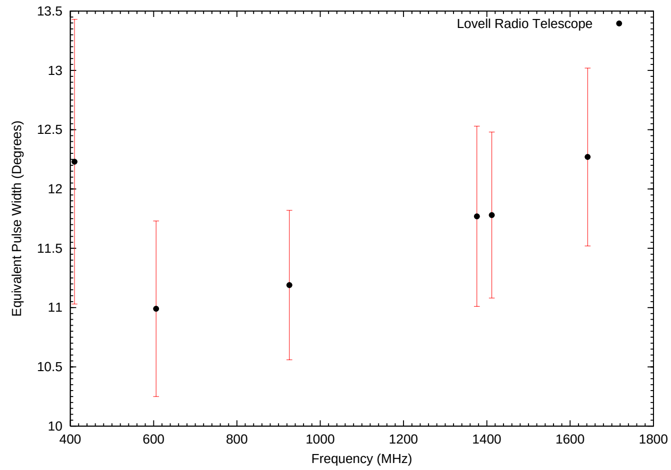

Figure 3.23: PSR B0540+23: The evolution of W_{eq} over a broadly sampled frequency range.

be a hidden law determining their behavior.

3.3 PSR B0740-28

Similarly to the case of PSR B0540+23, PSR B0740-28 has a gaussian-like pulse shape. Obviously, only widths can be studied.

3.3.1 General information about PSR B0740-28

PSR B0740-28 is located $1.9\ kpc$ from the Sun in the constellation of Puppis (Figure 3.24). Its dispersion measure is $73.77\ cm^{-3}pc$. Its period is $166.761\ ms$ with a derivative of roughly $16.8 \cdot 10^{-15}\ s/s$. Its $\dot{P}$ corresponds to a characteristic age of about $0.16 \cdot 10^{6}\ years$. The mean flux density at 400 and $1400\ MHz$ is 296 and 23 mJy respectively.

3.3.2 A discussion about profile morphology

Since no complication or peculiar structure appears on the profile (Figure 3.25), we proceed with the study of widths only. Note that once again the only available observations are those from the Lovell Telescope. The frequencies used to derive the following plots, are: 234, 326, 413.9, 606, 925, 1396, 1420, 1594, 1616 and $1642\ MHz$.

3.3.3 Integrated profile study

As it has already become clear, only Jodrell Bank data are available. Hence, we proceed to the broadly sampled frequency study.

Evolution of $W_{50\%}$

In Figure 3.26 we illustrate the evolution of $W_{50\%}$. Although it is not that obvious, the points are distributed in a manner that reminds us that of PSR B0540+23. Later we will discuss this point.

Evolution of $W_{10\%}$

In Figure 3.27 we present the derived plot for the evolution of $W_{10\%}$. Apparently, the points are widely scattered but still they exhibit a regular pattern.

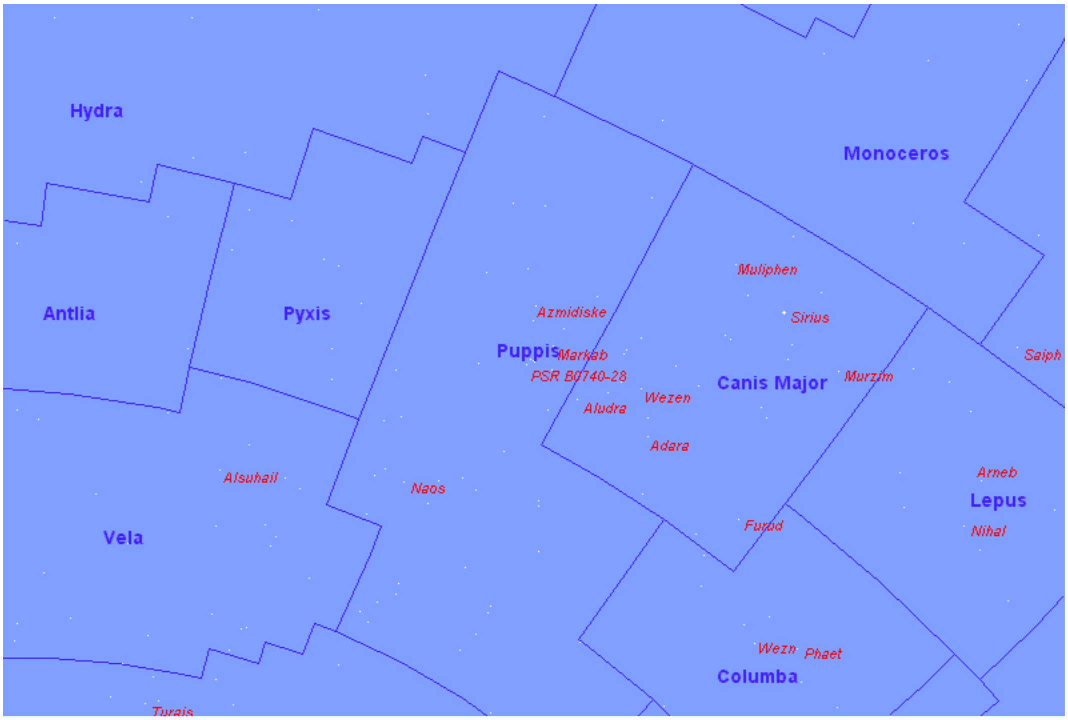

Figure 3.24: PSR B0740-28: Its location in the constellation of Puppis.

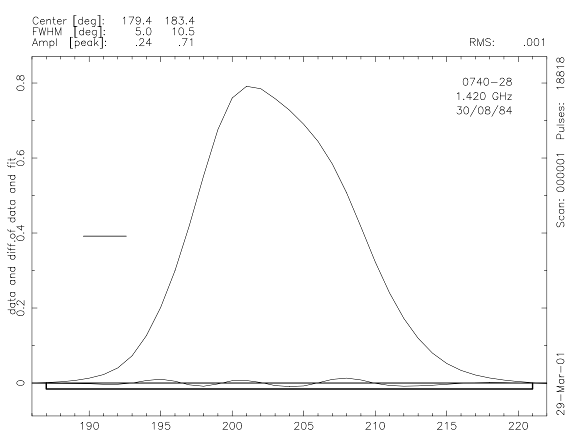

Figure 3.25: PSR B0740-28: A typical 21-cm observation.

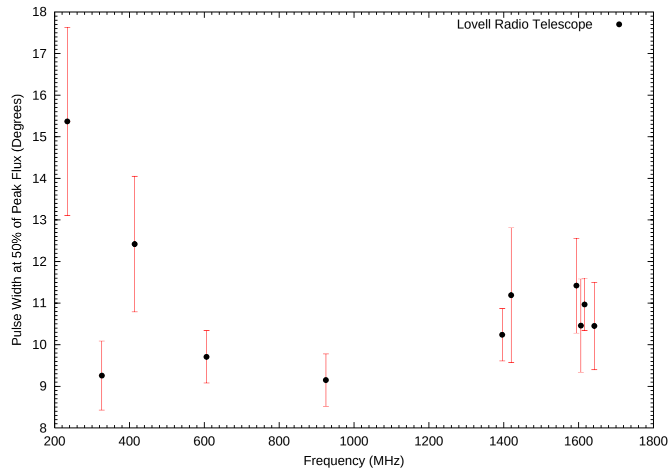

Figure 3.26: PSR B0740-28: The evolution over a broadly sampled frequency range of $W_{50\%}$.

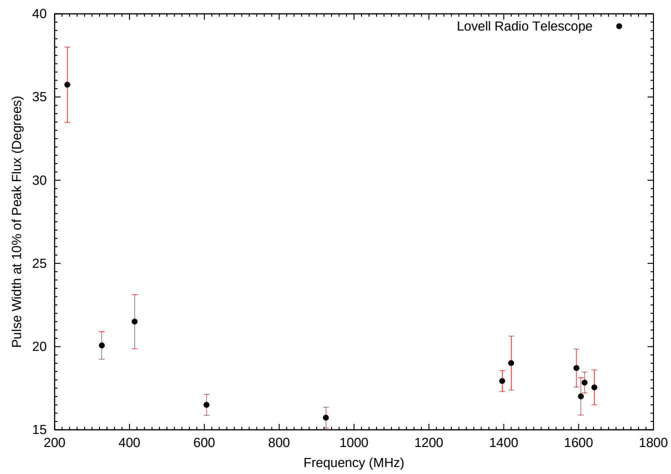

Figure 3.27: PSR B0740-28: The evolution over a broadly sampled frequency range of $W_{10\%}$.

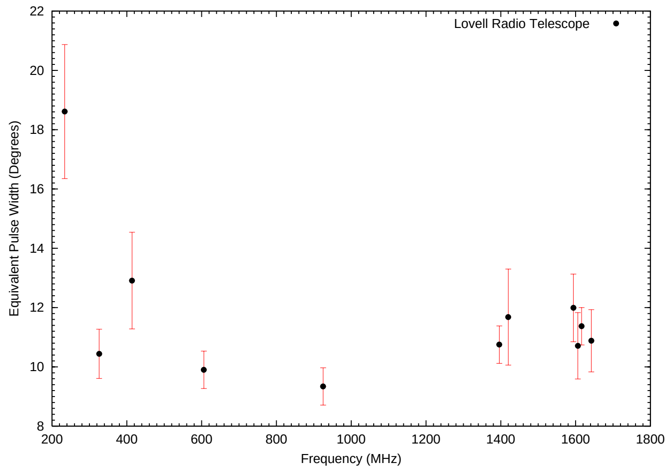

Figure 3.28: PSR B0740-28: Equivalent width versus frequency.

Evolution of W_{eq}

In Figure 3.28 we show the points corresponding to the $f - W_{eq}$ data.

A brief discussion

It is interesting that, although the points are more scattered than in the case of PSR B0540+23, still they show a somehow similar behavior. That is, initiating from large values, $W_{50\%}$ falls fairly fast to a regime of low values around 1 GHz and then increase again.

This become even more interesting if we pay attention to the fact that the same distribution is apparent, more or less, for the three widths. Of course, we could repeat the same statement concerning the evidence for correctness of our analysis procedure. But we are of the opinion that may be a law other than a power law would probably be of physical meaning.

3.4 PSR B1742-30

Undoubtedly, it would be very interesting to have both Jodrell Bank and Effelsberg data available for all the pulsars we study. Except for some particular cases this is impossible. PSR B1742-30 is one of the exceptions. That is, in the following presentation we disclose a study based on broadly sampled frequencies. In Section 4.2 we present the study based on closely sampled frequencies.

3.4.1 General information about PSR B1742-30

PSR B1742-30 is located 2.1 kpc from our Sun in the constellation of Scorpius (Figure 3.29). Its dispersion measure is about 88 $cm^{-3}pc$. It rotates once every 367.427 ms having a slowdown rate of approximately $10.7 \cdot 10^{-15}$ s/s. These values deduce a characteristic age of roughly $0.5 \cdot 10^{6}$ $years$. At 400 MHz its a mean flux density is 66 mJy. At 1400 MHz its mean flux density is about 14 mJy.

3.4.2 A discussion about profile morphology

Before any comment concerning the integrated profile's properties, it would be very illuminating to begin with the description of a peculiarity we encountered during the actual analysis. In paragraph 2.3.2 we discussed the small (but yet crucial) difficulty in defining the limits of $W_{10\%}$ or $W_{50\%}$ in particular cases. As we commented there, the problem arises only if 'side' gaussians are necessary to be added (for a more detailed discussion one can have a look through paragraph 2.3.2).

For PSR B1742-30 it came up that the problem was non-negligible. Even though the residuals between the actual data and the sum of the fitted gaussians had been restricted within the RMS 'belt' throughout the whole fitting region, **bfit** returned $W_{10\%}$ and $W_{50\%}$ values that seemed completely unreasonable. Therefore,

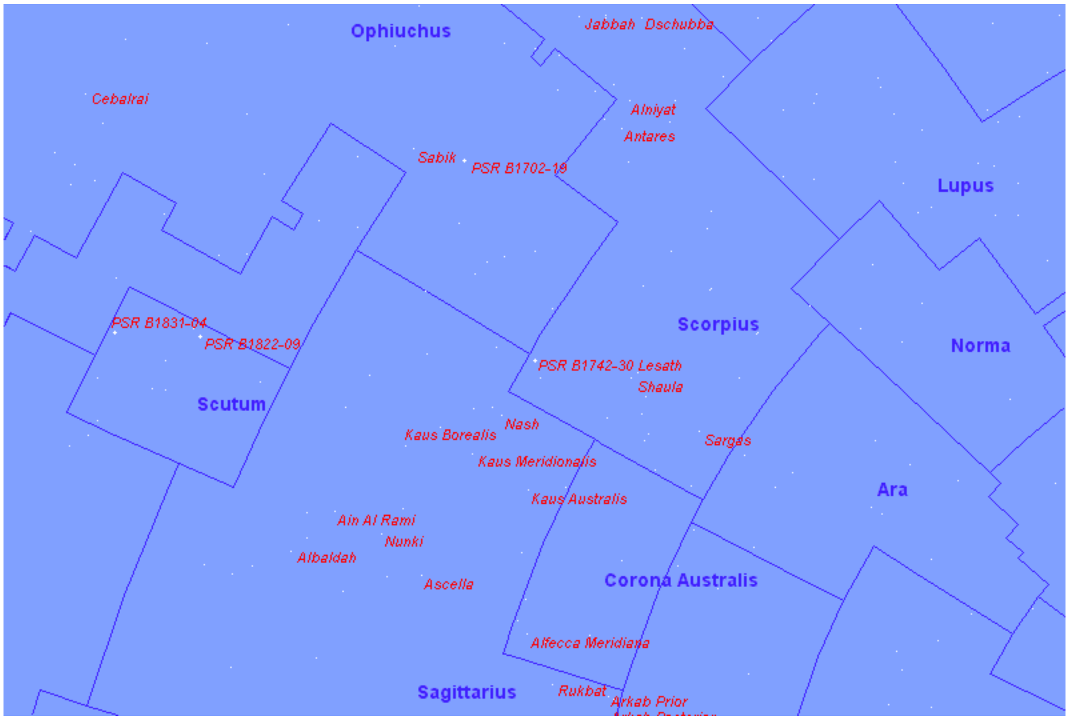

Figure 3.29: PSR B1742-30: Its location in the constellation of Scorpius.

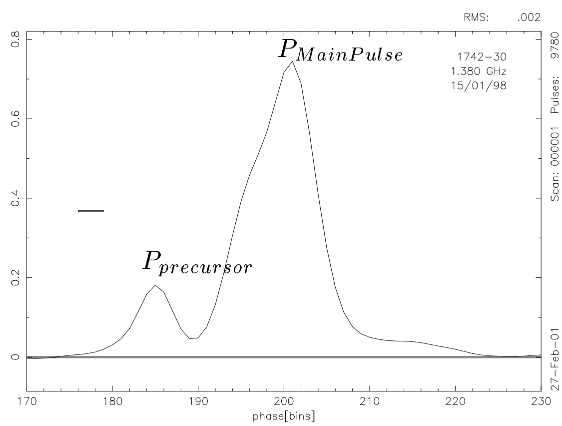

Figure 3.30: PSR B1742-30 : A typical 1380-MHz observation.

we ended up with the idea that the optimal way to overcome this hint was to study the main pulse separately from the precursor. In Figure 3.30 one can inspect the pulse profile displayed by PSR B1742-30.

3.4.3 Integrated profile study

Here we present the plots resulted from the study based on Jodrell Bank data alone. Later we repeat the procedure for data obtained with the Effelsberg Telescope. At present we base our study to the usage of: 410, 606, 925, 1380, 1412 and 1642 MHz.

Evolution of $W_{50\%}$

In Figures 3.31 and 3.32 we present the plot showing the evolution of $W_{50\%}$ for both the main pulse and the precursor. It obvious that it is impossible to fit a power law with the parameter b to be assigned a negative value.

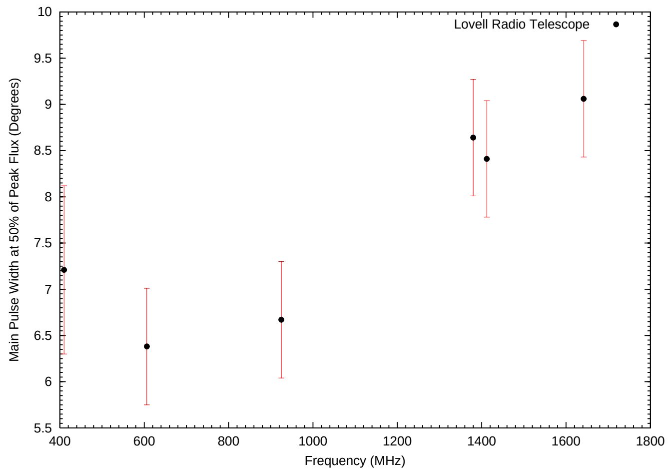

Figure 3.31: PSR B1742-30: The evolution of main pulse's $W_{50\%}$

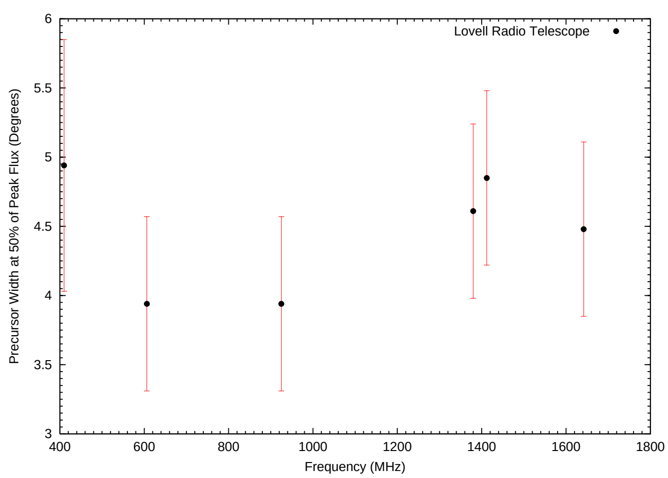

Figure 3.32: PSR B1742-30: The evolution of precursor's $W_{50\%}$

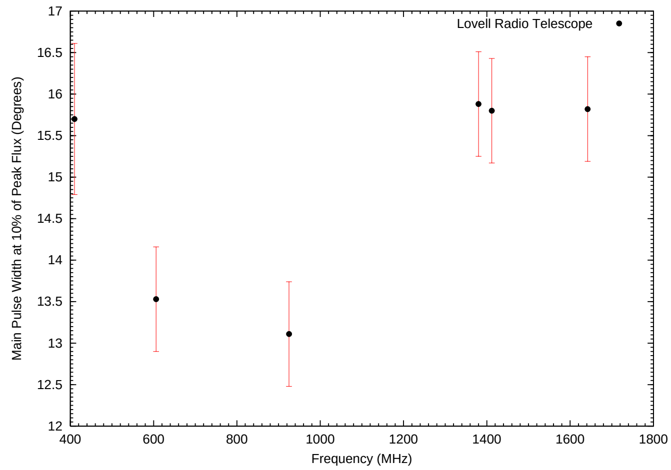

Figure 3.33: PSR B1742-30: The evolution of main pulse's $W_{10\%}$

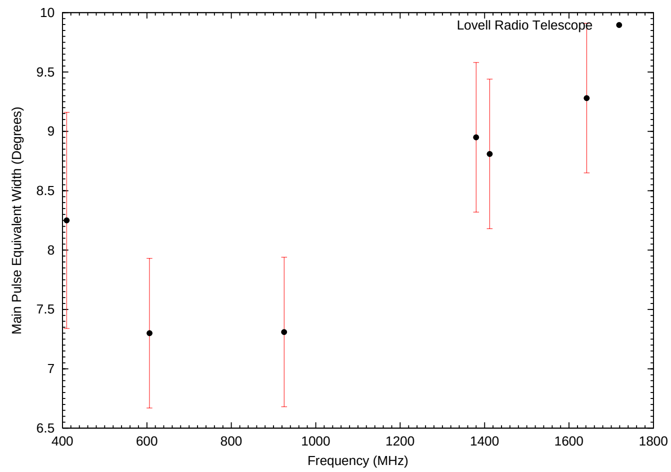

Figure 3.34: PSR B1742-30: The evolution of main pulse's W_{eq}

Evolution of $W_{10\%}$

Jodrell Bank data appear to lead us to unreliable results regarding the evolution of precursor's 10% width. Therefore, in Figure 3.33 we show only what corresponds to the main pulse.

Evolution of W_{eq}

In the case of equivalent width, the data seem to give good results even for the precursor. Figures 3.34 and 3.35 illustrate what we have obtained.

Separation between main pulse and precursor

The separation between main pulse and precursor is most likely to obey the familiar to us power law. In Figure 3.36 the observational points together with the fitted power law which corresponds to the parameters:

$$a = 21\,\frac{Degrees}{MHz^{-b}} \pm 0.7,\ b = -0.054 \pm 0.005 \tag{3.14}$$

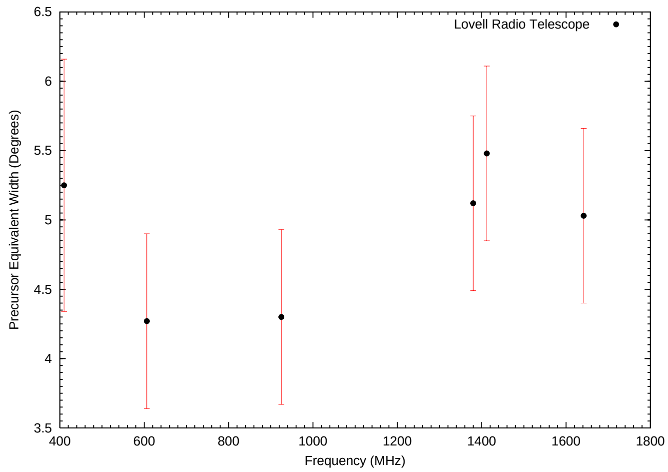

Figure 3.35: PSR B1742-30: The evolution of precursor's W_{eq}

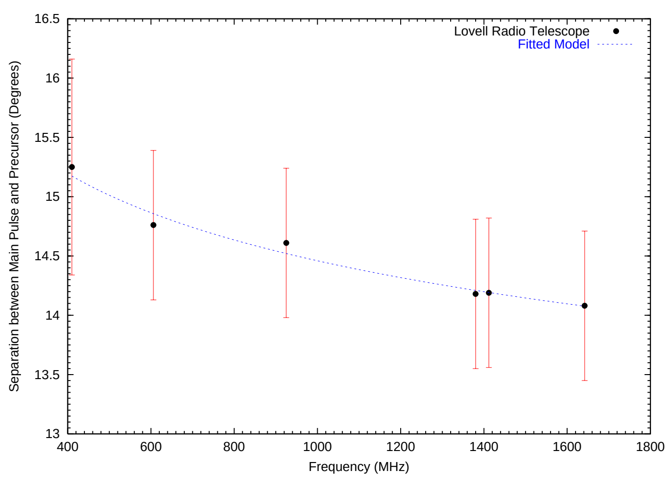

Figure 3.36: PSR B1742-30: separation between main pulse and precursor.

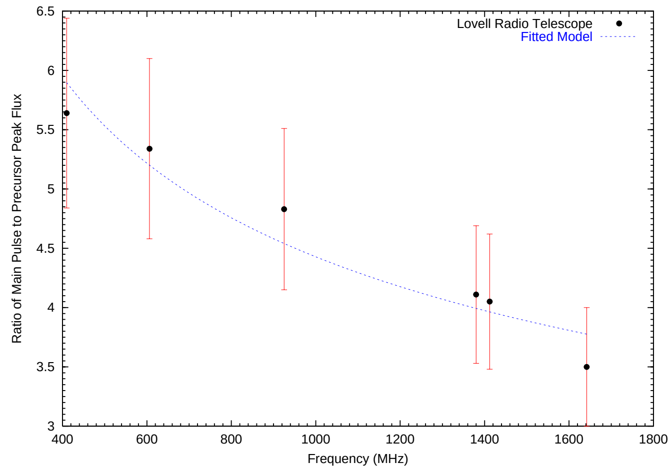

Figure 3.37: PSR B1742-30: The evolution of $P_{mainpulse}/P_{precursor}$

Evolution of $P_{mainpulse}$ over $P_{precursor}$

The evolution of $P_{mainpulse}/P_{precursor}$ seems to obey the power law. In Figure 3.37 we present the results. The parameters have the values:

$$a = 41\,\frac{Degrees}{MHz^{-b}} \pm 13,\; b = -0.321 \pm 0.047 \tag{3.15}$$

A brief discussion

Except for the separation between main pulse and precursor (Figure 3.36) and the ratio of the peaks associated with them (Figure 3.37), all the other studied properties display the same behavior over frequency. Hence, it is very likely that a physical process, other than a power law, governs their development. Note that dramatic changes seem to happen around 1400 MHz.

3.5 PSR B1822-09

3.5.1 General information about PSR B1822-09

PSR B1822-09 is placed in the constellation of Scutum, 1 kpc from the Sun. Its dispersion measure is about 19 $cm^{-3}pc$. Its period is approximately $768.979\ ms$ and its derivative $52.4 \cdot 10^{-15}\ s/s$. Therefore, the age characterizing it is about $0.2 \cdot 10^6\ years$. Its mean flux density at 400 and 1400 MHz is 36 and 11 mJy respectively.

3.5.2 A discussion about profile morphology

In Figure 3.39 we provide the reader with a typical 21-cm observation. As it is shown there, PSR B1822-09 has a very interesting profile made of two clearly separated peaks and an inter-pulse as well.

3.5.3 Integrated profile study

Using observations obtained with the Lovell Telescope at frequencies of: 408, 608, 925, 1380, 1419.5, 1616 and 1642 MHz, we studied the behavior of the widths. In addition, we studied the separation and the ratio between main pulse and inter-pulse. We refrain from giving results about the inter-pulse's widths. Although, calculations have been done we regard the results unreliable due to its weakness.

Before presenting our results it is important to note the following. $W_{50\%}$ was studied only for the main pulse, ignoring the precursor. This was done in order to avoid the already mentioned problem displayed by

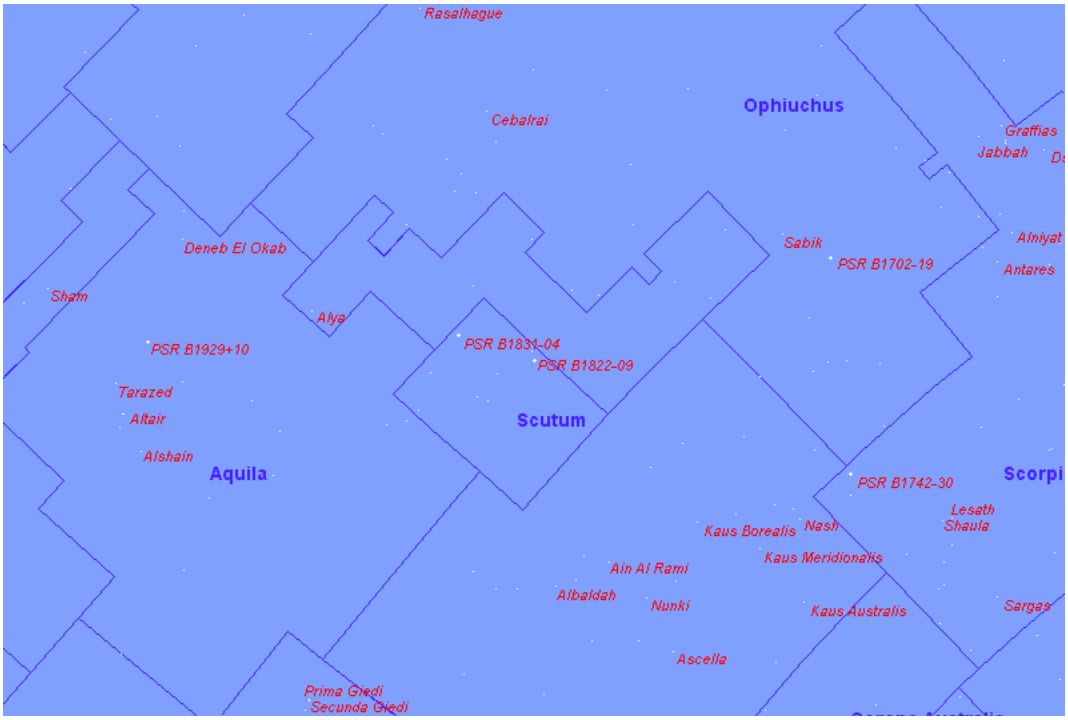

Figure 3.38: PSR B1822-09: Its location in the constellation of Scutum.

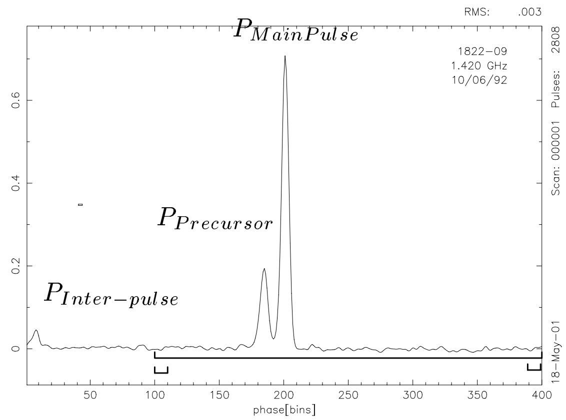

Figure 3.39: PSR B1822-09: A typical observation at 1420 MHz.

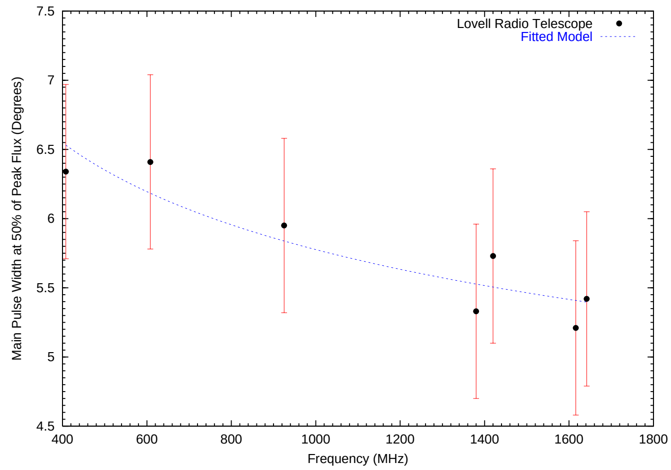

Figure 3.40: PSR B1822-09: Main pulse's $W_{50\%}$ and the fitted power law.

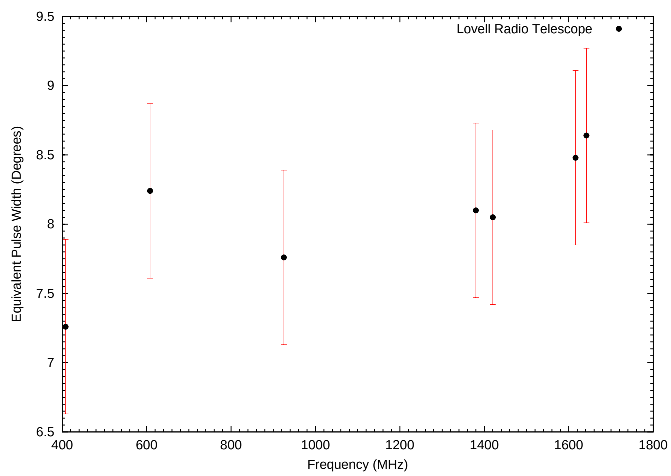

Figure 3.41: PSR B1822-09: The overall W_{eq}.

bfit. For similar reasons we have not studied $W_{10\%}$. However, W_{eq} which is associated to the whole main pulse (i.e. the precursor and the main component), was studied.

Evolution of main pulse's $W_{50\%}$

In Figure 3.40 we plot not only the distribution of the observational points but the fitted power law as well. The later corresponds to:

$$a = 15\,\frac{Degrees}{MHz^{-b}} \pm 2.7,\ b = -0.137 \pm 0.027 \tag{3.16}$$

Evolution of the overall W_{eq}

The overall W_{eq} tries to describe the equivalent width that corresponds to a fitting range that covers the main pulse and the precursor. The manner in which this quantity changes over frequency is shown in Figure 3.41. No power law is possible to fit the data.

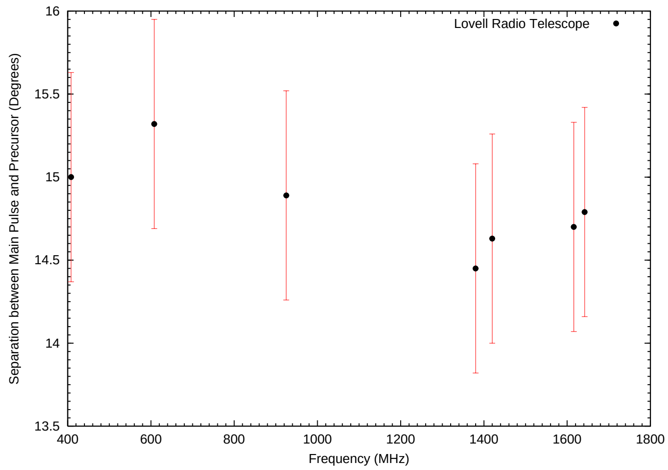

Figure 3.42: PSR B1822-09: Separation between main pulse and precursor.

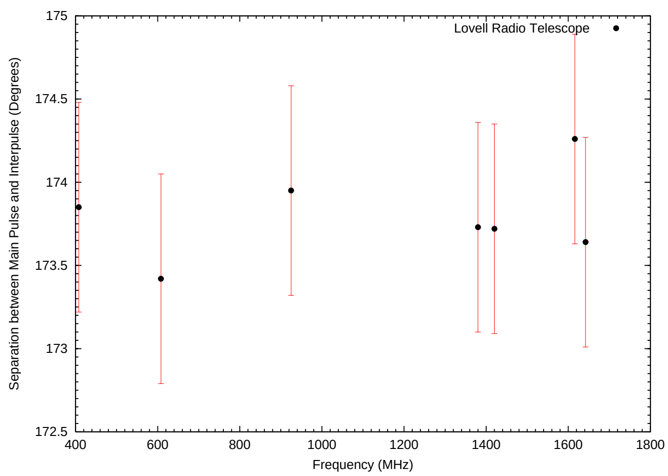

Figure 3.43: PSR B1822-09: Separation between main pulse and inter-pulse.

Separations

Here we gather all the plots related to the separation between two features of the profile. Figures 3.42, 3.43 and 3.44 show the evolution of the separation between the main pulse and the precursor, the main pulse and the inter-pulse and the precursor and the inter-pulse, respectively.

Ratios

The ratio between the main pulse and the precursor peak flux or the main pulse and inter-pulse are related to frequency as shown in Figures 3.45 and 3.46.

A brief discussion

Apart from $W_{50\%}$, the characteristic properties of PSR B1822-09 possess a qualitatively similar behavior though different from the power law. It is noteworthy that the exponent b, characterizing the power law in the case of $W_{50\%}$, is assigned the value 7.1 which is close to what would be expected according to the proposal made by Smith.

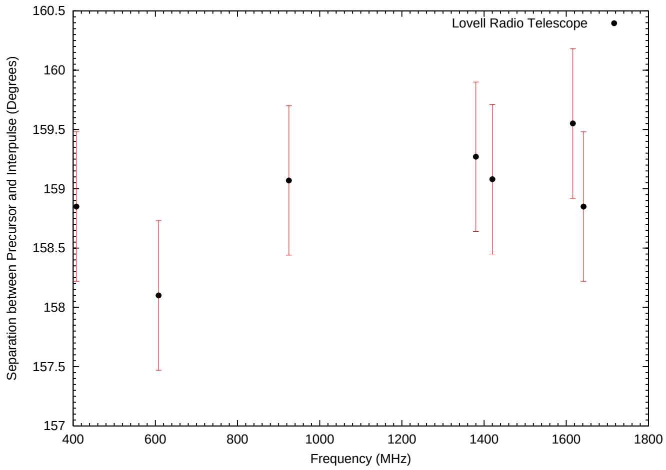

Figure 3.44: PSR B1822-09: Separation between inter-pulse and precursor.

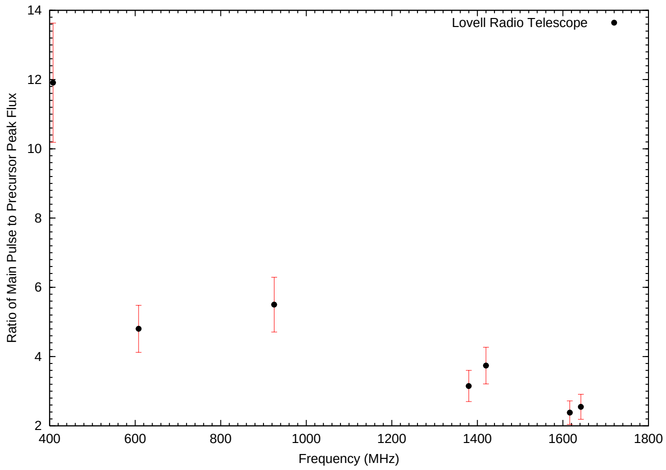

Figure 3.45: PSR B1822-09: $P_{mainpulse}$ over $P_{precursor}$.

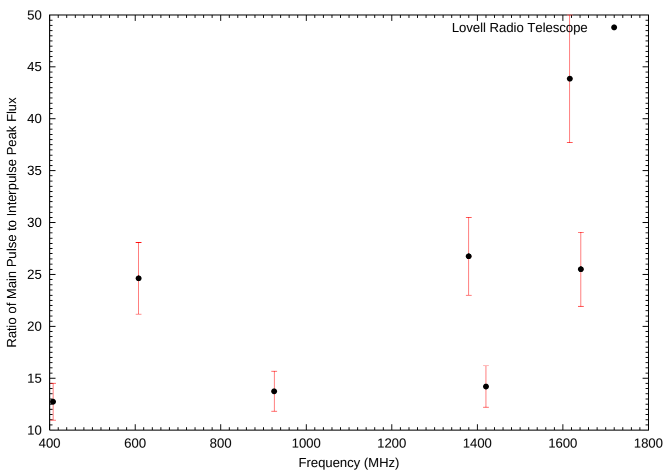

Figure 3.46: PSR B1822-09: $P_{mainpulse}$ over $P_{inter-pulse}$.

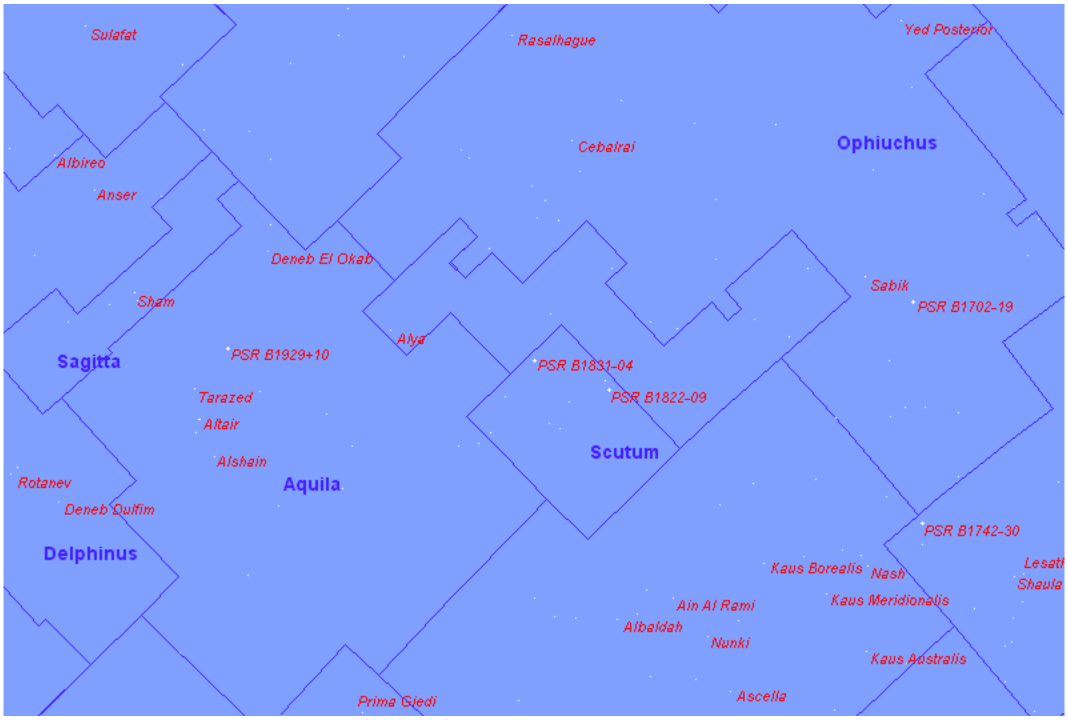

Figure 3.47: PSR B1831-04: Its location in the constellation of Scutum.

3.6 PSR B1831-04

As will be shown later, PSR B1831-04 has a profile of profound complexity. This fact, in conjunction with the discussion we have presented concerning the peculiarity of **bfit**, prevented us from obtaining measurements of $W_{50\%}$ and $W_{10\%}$.

3.6.1 General information about PSR B1831-04

PSR B1831-04 rotates once every $290.108\ ms$ in the constellation of Scutum, $2.3\ kpc$ from the Earth. It keeps transforming rotational kinetic energy into radiation for at least $23.3 \cdot 10^{6}\ years$ at a rate of $0.197 \cdot 10^{-15}\ s/s$. Its DM is about 19 and its mean flux density at 400 and 1400 MHz is 77 and 15 mJy respectively.

3.6.2 Discussion about profile morphology

In Figure 3.48 we present a typical observation of PSR B1831-04 at 1404 MHz. A quick glance through that picture reveals an amazing structure characterizing the profile. This complexity made it impossible to work out reliable calculations of the widths. In the following only estimations of W_{eq} have been undertaken.

3.6.3 Integrated profile study

Here we focus on the evolution of separations and ratios. The reason for such a decision has been already explained. We should keep in mind that the following analysis is based on four frequency observations with the Lovell Telescope at 411, 606, 1380 and 1404 MHz.

Evolution of W_{eq}

Figure 3.49 illustrates the results from the study of the equivalent pulse width. Obviously the observational points are widely spread.

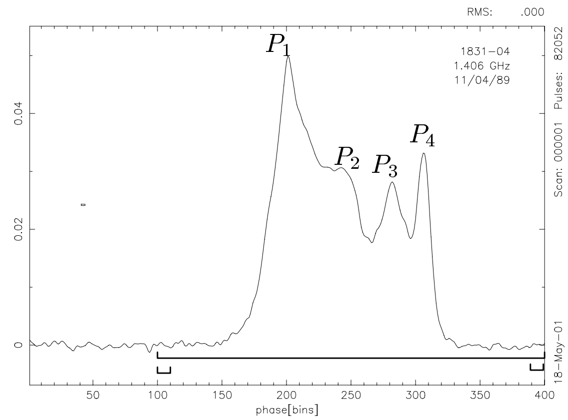

Figure 3.48: PSR B1831-04: Observed at 21 cm (1420 MHz). The terminology used in the text is also indicated.

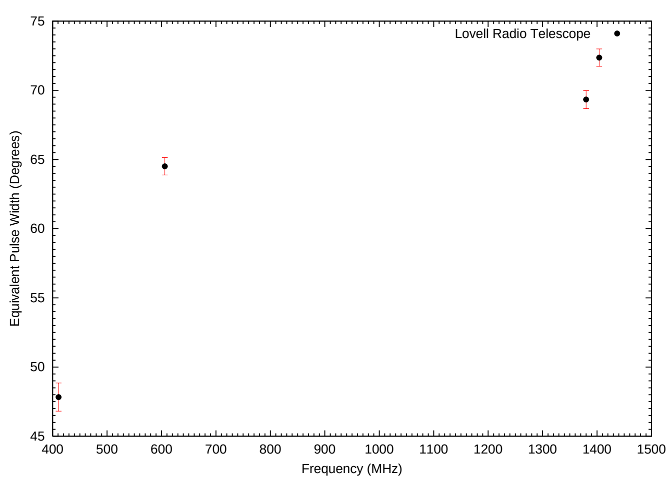

Figure 3.49: PSR B1831-04: The evolution of W_{eq}.

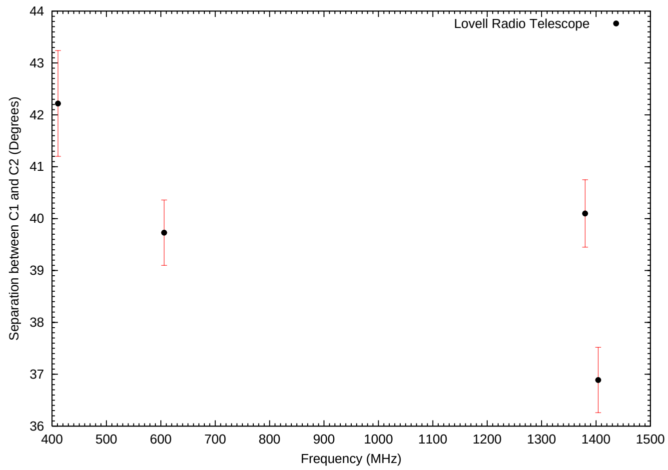

Figure 3.50: PSR B1831-04: The evolution of $C_2 - C_1$.

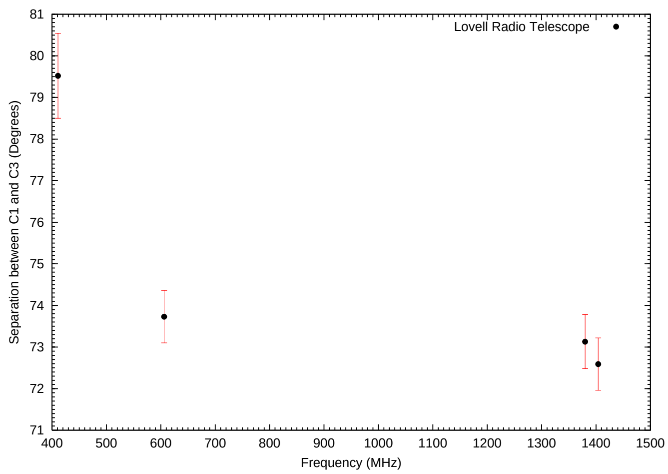

Figure 3.51: PSR B1831-04: The evolution of $C_3 - C_1$.

Separations

In Figures 3.50, 3.51 and 3.52 we summarize the derived plots for the separation between C_1 and the three remaining components. In the last picture we also present a possible power law to fit the data. This model is characterized by:

$$a = 123\,\frac{Degrees}{MHz^{-b}} \pm 7.6,\ b = -0.037 \pm 0.009 \tag{3.17}$$

Ratios

Let us introduce now the evolution of the ratio between P_1 and the rest of the peaks. Figures 3.53, 3.54 and 3.55 illustrate the results. The parameters of the model fitting the data in Figure 3.54, are:

$$a = 15\,\frac{Degrees}{MHz^{-b}} \pm 2.8,\ b = -0.3 \pm 0.027 \tag{3.18}$$

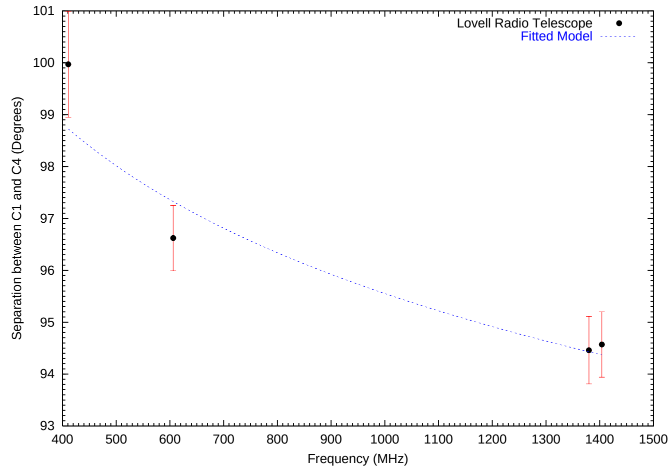

Figure 3.52: PSR B1831-04: The evolution of $C_4 - C_1$ plus the fitted power law.

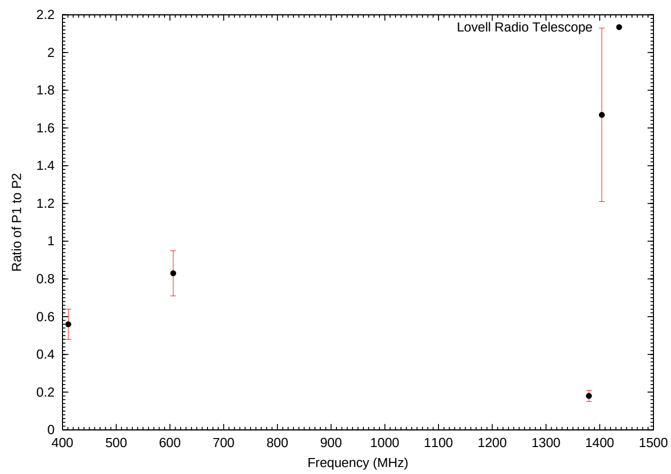

Figure 3.53: PSR B1831-04: The evolution of P_1/P_2.

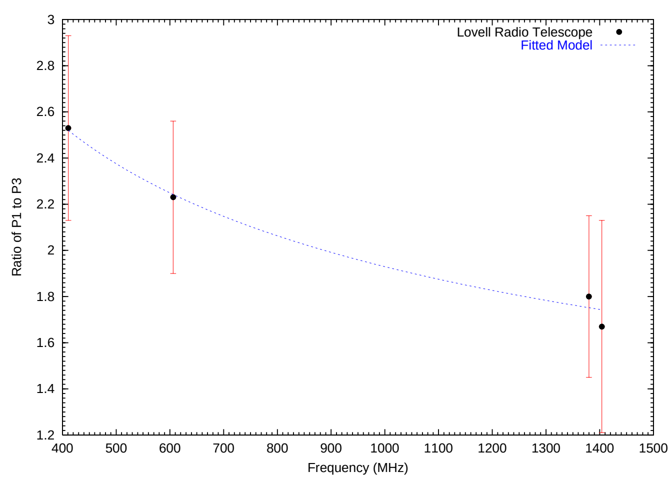

Figure 3.54: PSR B1831-04: The evolution of P_1/P_3 together with the fitted power law.

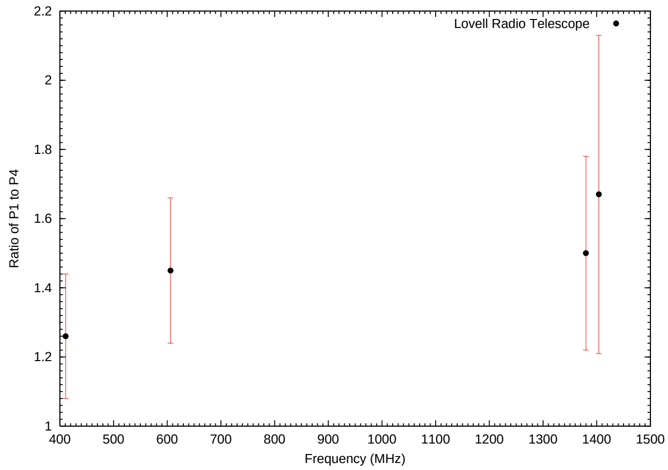

Figure 3.55: PSR B1831-04: The evolution of P_1/P_4.

A brief discussion

In the above study, the absence of data within the range from about $600\ MHz$ up to $1400\ MHz$, is obvious. Hence, no safe general conclusions can be reached through the examination of the above plots.

3.7 PSR B1929+10

In the context of the present work what we probably enjoyed most was the study of PSR B1929+10. As the reader will realize later, it displays some interesting regularities. Besides, we started our analysis with this pulsar. Therefore, one can easily imagine how enthusiastically we received so regular frequency development for all the parameters we investigated. The detailed analysis is presented in the following paragraphs. Moreover, it served (together with PSR B0525+21) as a test for the correctness of our method since it has been studied, to some extend, in the past.

3.7.1 General information about PSR B1929+10

PSR B1929+10 lies in the constellation of Aquila, not farther than $0.2\ kpc$ from the Sun. Its DM is about $3\ pccm^{-3}$ and it spins with a period of $226.518\ ms$. Its slowdown rate is about $1.2{\cdot}10^{-15}\ s/s$ giving a characteristic age close to $3{\cdot}10^{6}\ years$. PSR B1929+10 is strong enough to emit a mean flux density of $303\ mJy$ at $400\ MHz$ and 41 at $1400\ MHz$.

3.7.2 A discussion about profile morphology

Figure 3.57 depicts a typical observation of PSR B1929+10 at $1418\ MHz$ carried out with the Lovell Telescope. Besides the main pulse, this pulsar exhibits an inter-pulse as well. Before proceeding with the analysis, it would be important to discuss the issue of time resolution which makes a big difference between observations from different instruments. In Figure 3.58 a similar observation obtained with the Effelsberg Telescope is illustrated. During the Effelsberg observation the time resolution was 220 μs whereas during the Jodrell Bank observation it was only 566.3 μs. As one can easily notice, there are important differences between these two Figures. In the later profile there are three ‘peaks’ clearly seen in the main pulse, whereas in the former one, only one is obvious.

On the one hand, such an effect can be attributed to the difference between the de-dispersion channel bandwidths. If the de-dispersion channels are too wide then the pulse broadening due to interstellar medium becomes significant. Hence, the congenital structure of the pulse may disappear.

On the other hand, it can be due to the low time resolution used during the observation. Obviously, a relatively low time resolution can smooth out the profile ‘hiding’ the possible fine structure intrinsically existing in the pulse.

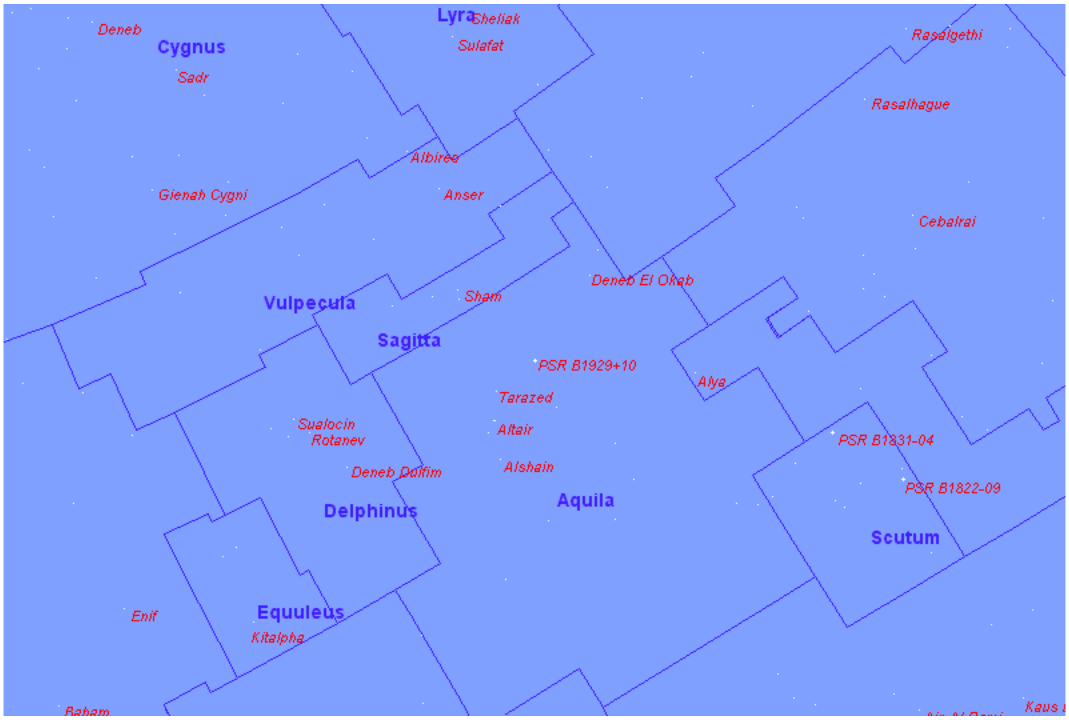

Figure 3.56: PSR B1929+10: Its location in the constellation of Aquila.

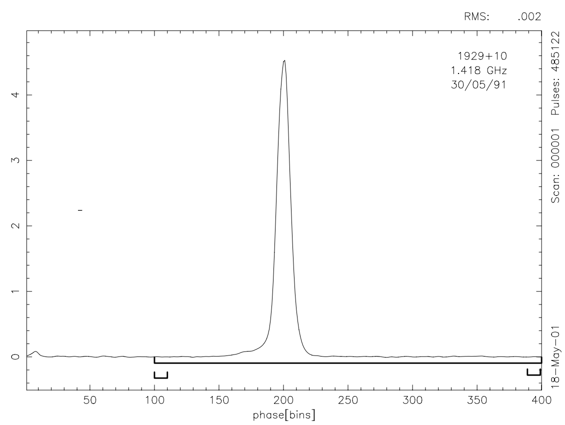

Figure 3.57: PSR B1929+10: Observed with the Lovell Telescope at 1418 MHz.

In the case of PSR B1929+10, the difference between the time resolution used for these two particular observations, is large enough to cause the effect discussed previously. Since the total number of superposed pulses was sufficiently large to provide stable profiles, in the subsequent analysis it is consequently assumed that the ‘real’ number of peaks is three. Of course in this section that we focus only on Lovell data we refrain from studying separations and ratios between components pretending that they do not exist. In Chapter 4, where we base our study exclusively on Effelsberg data, we study individual components as well.

3.7.3 Integrated profile study

Based on Lovell observations we proceed in presenting the evolution of profile’s characteristics. The frequencies used, are: 237, 325, 410, 611, 925, 1396, 1418 and 1642 MHz.

Widths’ evolution

Here we compile all the plots illustrating the frequency dependence of widths. Estimations have been made for both the main pulse and the inter-pulse. Specifically, in Figure 3.60 we present a fitted power law as well.

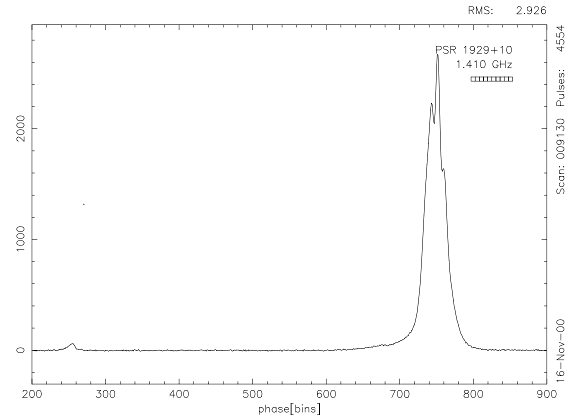

Figure 3.58: PSR B1929+10: Observed with the Effelsberg Telescope at 1410 MHz.

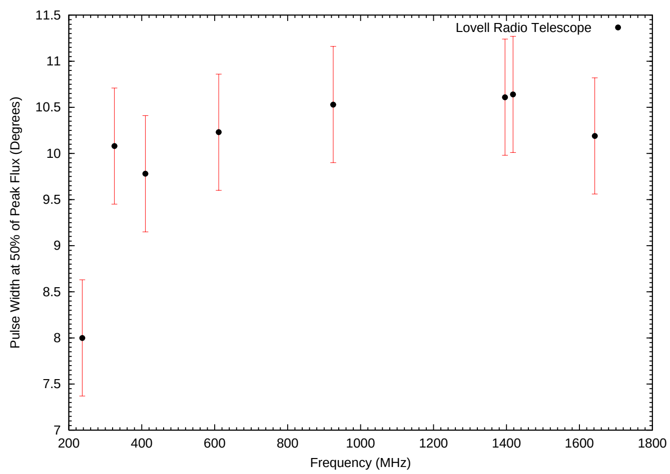

Figure 3.59: PSR B1929+10: Main pulse's $W_{50\%}$

Its parameters, are:

$$a = 48\,\frac{Degrees}{MHz^{-b}} \pm 4,\; b = -0.122 \pm 0.014 \tag{3.19}$$

Separation between main pulse and inter-pulse

In Figure 3.64 we give the plot describing the evolution of the separation between the main pulse and the inter-pulse.

Evolution of $P_{mainpulse}$ over $P_{inter-pulse}$

Figure 3.65 presents the evolution of the ratio $P_{mainpulse}/P_{inter-pulse}$.

A brief discussion

Although the development of main pulse's $W_{10\%}$ seems to be in good agreement with a power law, all the other properties display a behavior that significantly diverges from what would be expected according to the theory presented in Section 2.1.4. Still, a regularity in the distribution of all the characteristic properties is rather obvious.

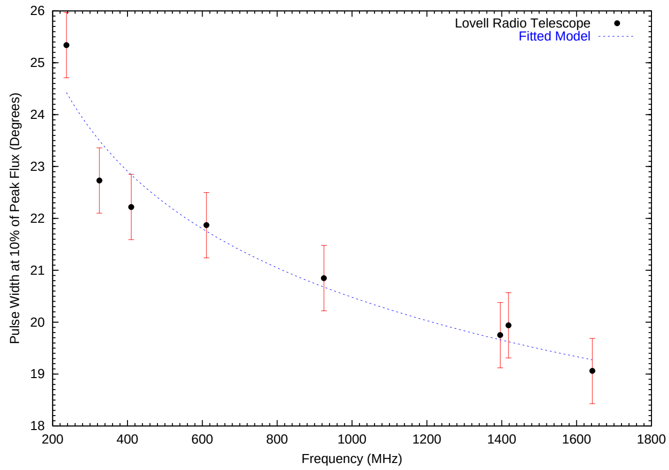

Figure 3.60: PSR B1929+10: Main pulse's $W_{10\%}$ with a fitted power law.

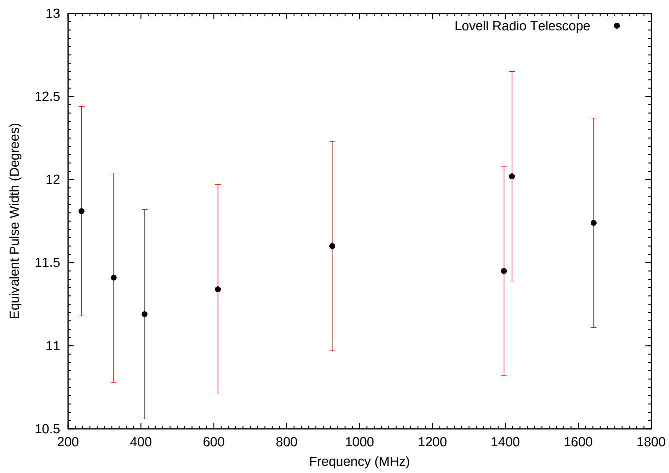

Figure 3.61: PSR B1929+10: Main pulse's equivalent width.

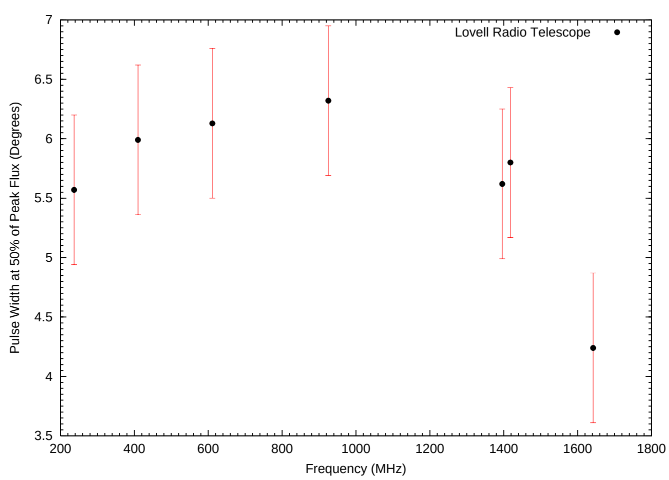

Figure 3.62: PSR B1929+10: Inter-pulse's $W_{50\%}$.

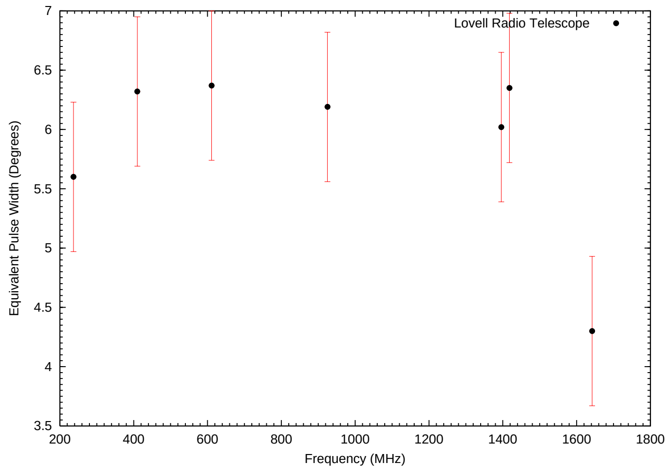

Figure 3.63: PSR B1929+10: Inter-pulse's W_{eq}.

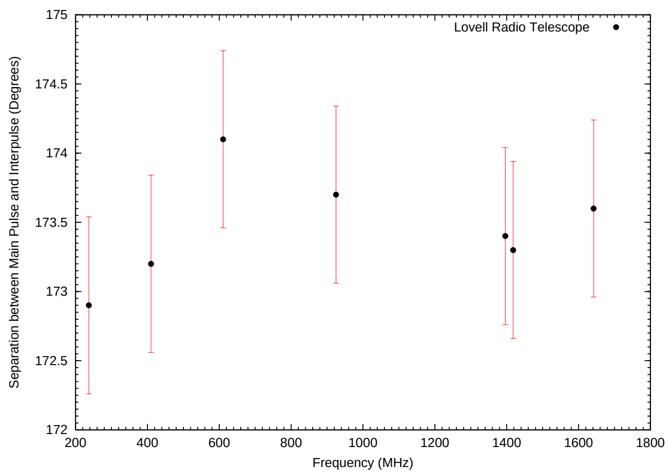

Figure 3.64: PSR B1929+10: The evolution of $C_{mainpulse} - C_{inter-pulse}$.

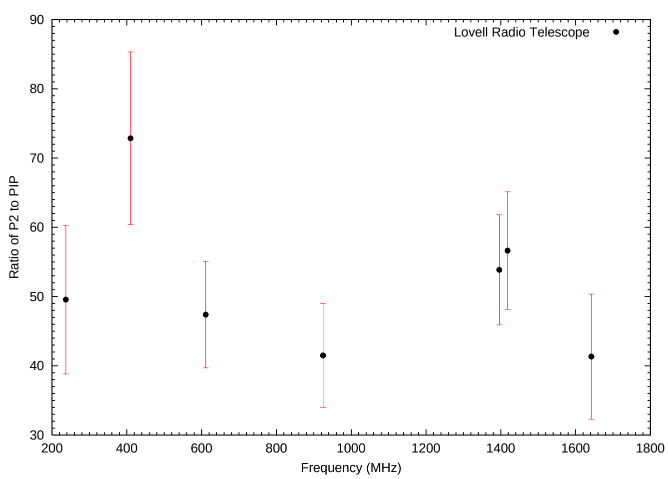

Figure 3.65: PSR B1929+10: The evolution of $P_{mainpulse}/P_{inter-pulse}$.

Chapter 4

Evolution over Closely Sampled Frequency Range

The present Chapter is to satisfy our initially planed aim. That is, to study the evolution of integrated pulse profile over a frequency range that has been closely sampled. After having done so, an answer to the question, “do the observed profile changes happen fast or gradually?”, may be reached.

The forthcoming text is organized in sections each one of which is dedicated to an individual pulsar. The sections are in the order of pulsars’ galactic coordinates.

At the beginning of each section a typical profile gained with the Effelsberg Radio Telescope is presented, even if a similar profile was presented in the previous chapter. This is necessary since, in most cases, the time resolution is significantly higher from that supported by the Lovell Radio Telescope.

4.1 PSR B1702-19

PSR B1702-19 is the first pulsar to be studied with observations taken with the Effelsberg Radio Telescope. Therefore, we shall carefully follow the associated analysis.

4.1.1 General information about PSR B1702-19

Figure 4.1 indicates that PSR B1702-19 is placed in the constellation of Ophiuchus, $1.2\ kpc$ from our solar system. Its estimated DM is about $23\ cm^{-3}pc$. It has a period of $298.987\ ms$ and a $\dot{P}$ of $4.1{\cdot}10^{-15}\ s/s$. Hence, its characteristic age is approximately $1.2{\cdot}10^{6}\ years$. Its mean flux density for observations at 400 and $1400\ MHz$ is respectively 29 and $8\ mJy$.

4.1.2 A discussion about profile morphology

Apart from being the first pulsar to be studied in the context of our initially planed project (that is to examine how fast the profile changes happen using closely sampled frequencies), PSR B1702-19 possesses a profile of astonishingly interesting structure. As shown in Figure 4.2 and 4.3 it has a multi-component profile following an inter-pulse of fairly high flux. In Figure 4.2 we also indicate the used terminology.

4.1.3 Integrated profile study

From all the components present on its profile we only study the relation between C_1 and C_2. The reason for this decision is obvious after a careful investigation of the profile. Only C_1 and C_2 have a clearly distinguishable peak so that one can estimate their center.

Moreover, we study the widths’ evolution for the inter-pulse and of course its separation from the main pulse. Keep in mind that the observations are from Effelsberg, they have been carried out at closely sampled frequencies and the profiles have been smoothed before any calculation. The smoothing parameter was set to 1. The frequencies used were: 1315, 1410, 1510, 1615 and 1710 MHz.

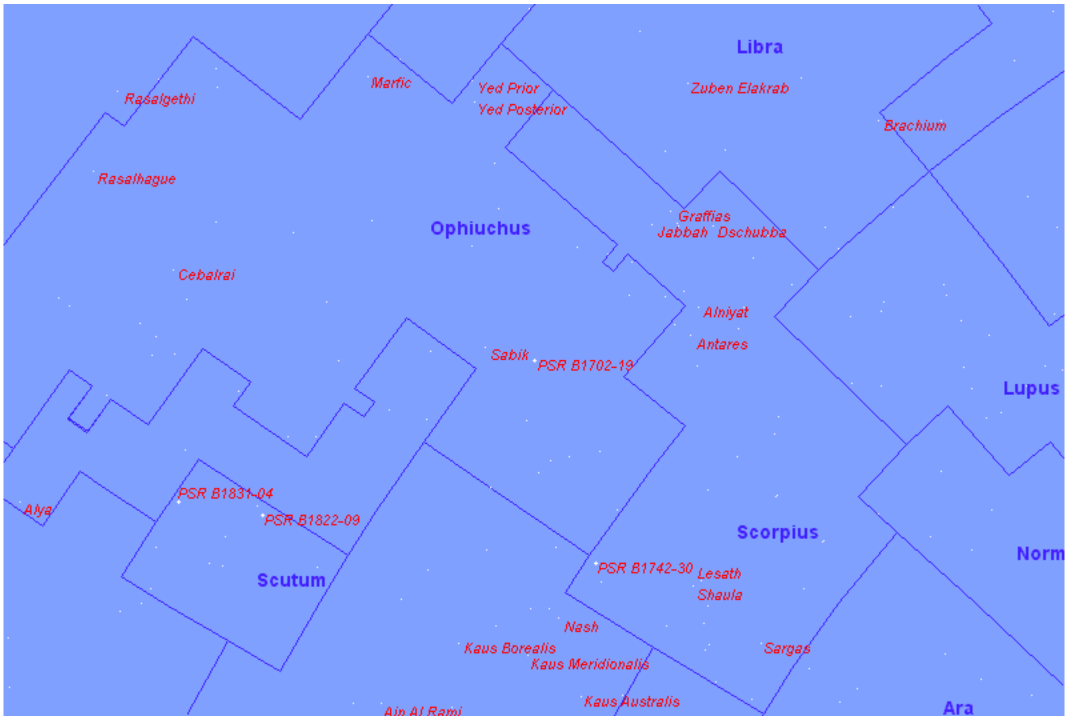

Figure 4.1: PSR B1702-19: Its location in the constellation of Ophiuchus.

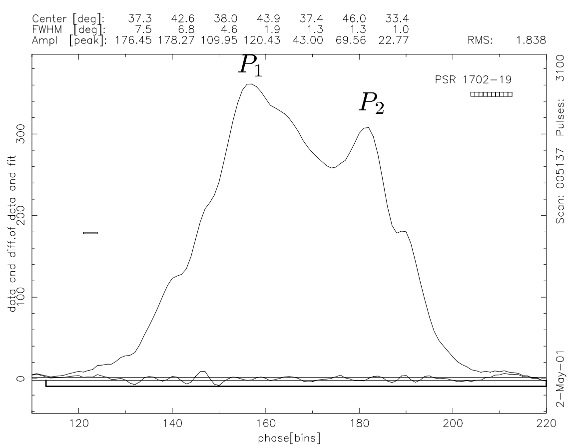

Figure 4.2: PSR B1702-19 : The main pulse at a typical 21-cm Effelsberg observation.

Evolution of main pulse's $W_{50\%}$

In Figure 4.4 we present the evolution of main pulse's $W_{50\%}$. Remember that the data are only from Effelsberg. In fact we have tried to fit a power law to the data but the errors are huge. Therefore, a law of this kind is inappropriate to fit data associated with closely sampled frequencies.

Evolution of main pulse's $W_{10\%}$

In Figure 4.5 the derived plot illustrating the main pulse's $W_{10\%}$ distribution versus frequency is shown. No power law can be fitted to the data.

Evolution of main pulse's W_{eq}

In Figure 4.6 we present the derived plot for the relation between frequency and the main pulse's W_{eq}.

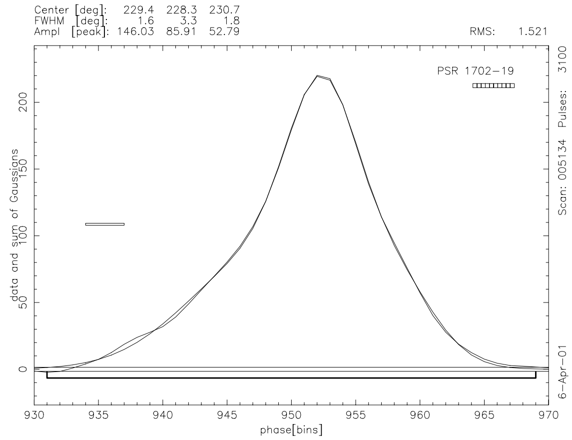

Figure 4.3: PSR B1702-19 : The inter-pulse at a typical 21-cm Effelsberg observation.

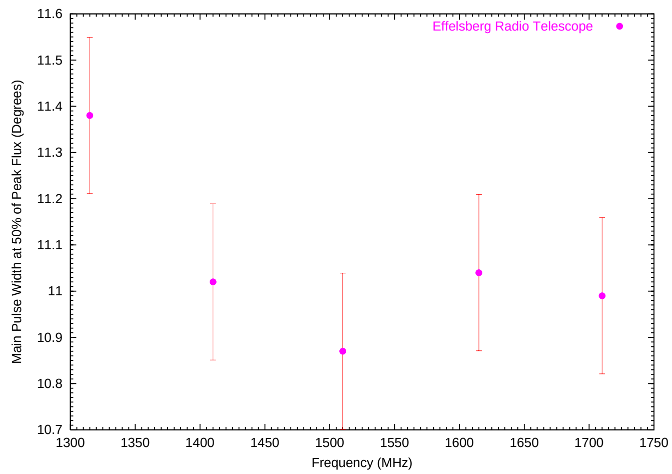

Figure 4.4: PSR B1702-19: The evolution, over a closely sampled frequency range, of the main pulse's $W_{50\%}$.

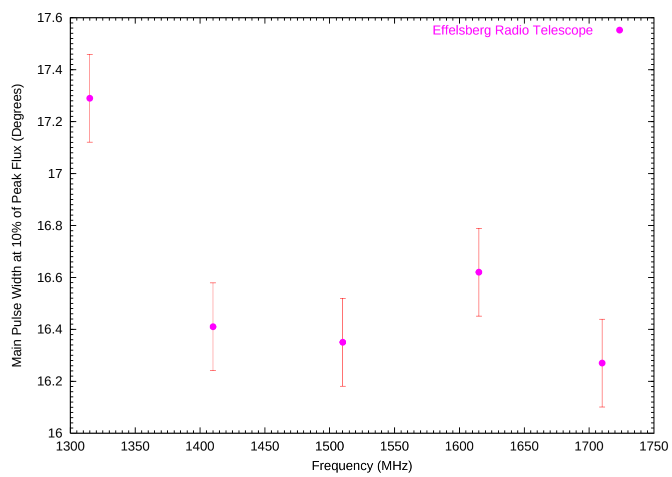

Figure 4.5: PSR B1702-19: The evolution, a over closely sampled frequency range, of the main pulse's $W_{10\%}$.

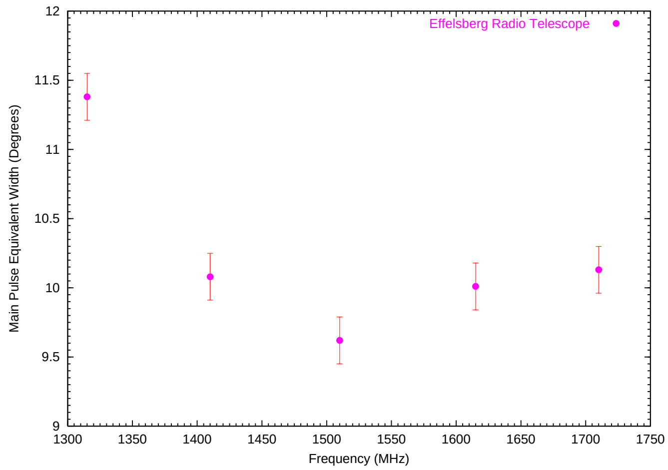

Figure 4.6: PSR B1702-19: The evolution, over a closely sampled frequency range, of the main pulse's W_{eq}.

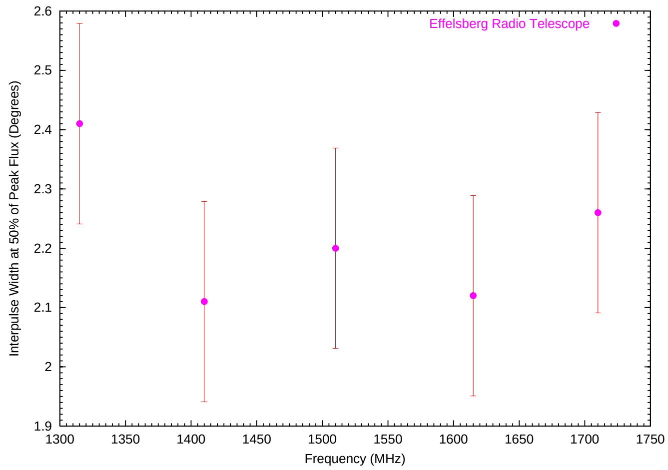

Figure 4.7: PSR B1702-19: The evolution, a over closely sampled frequency range, of the inter-pulse's $W_{50\%}$.

Evolution of inter-pulse's $W_{50\%}$

In Figure 4.7 we plot the evolution of the inter-pulse's $W_{50\%}$ while in 4.8 that of the inter-pulse's $W_{10\%}$.

The evolution of inter-pulse's W_{eq}

In Figure 4.9 we plot W_{eq} versus frequency.

Discussion about the evolution of widths

Avoiding to give a sophisticated explanation of the observed distributions, we only concentrate on a purely qualitative description. Obviously, the development of all widths is smooth.

All widths, for both the main pulse and the inter-pulse, display somehow the same behavior. Initiating with large values they fall to a flat regime (around $1500\ MHz$) to increase again around $1700\ MHz$.

Separation between C_1 and C_2

The separation between C_1 and C_2 is somehow indicative of the beamwidth of the emission. Therefore, it is very interesting to test whether it displays a behavior qualitatively similar to that of the widths. Figure 4.10 holds the answer. Obviously we have a slight deviation from the behavior we encountered so far.

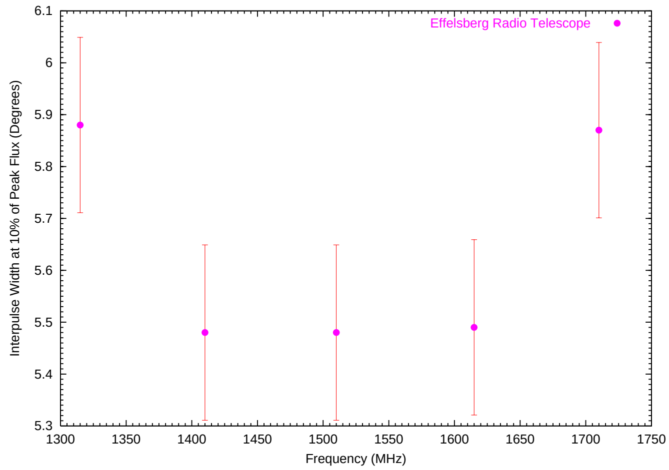

Figure 4.8: PSR B1702-19: The evolution, over a closely sampled frequency range, of the inter-pulse's $W_{10\%}$.

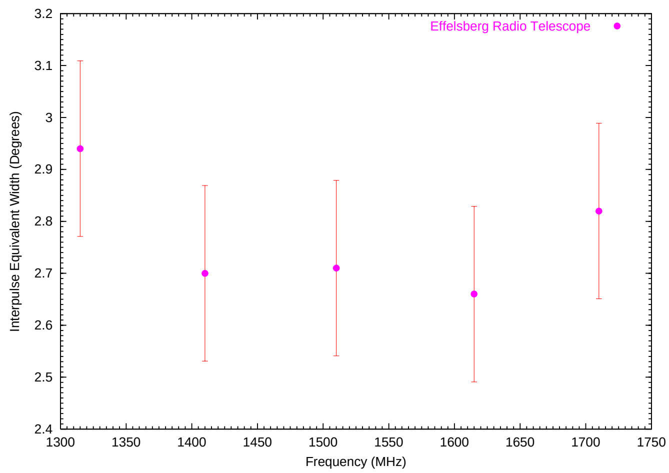

Figure 4.9: PSR B1702-19: The evolution, over a closely sampled frequency range, of the inter-pulse's W_{eq}.

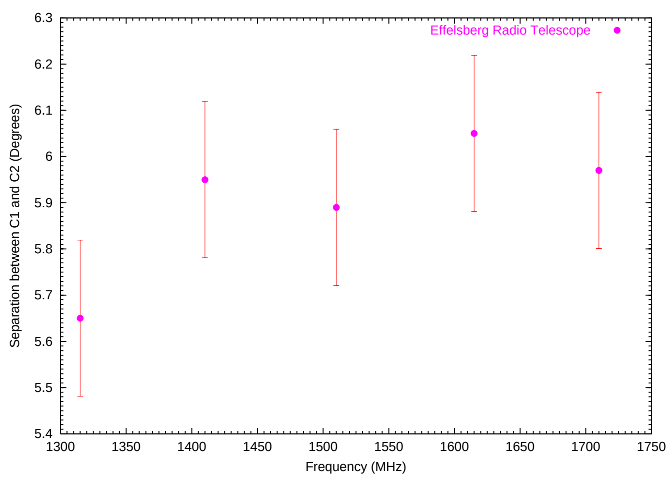

Figure 4.10: PSR B1702-19: The evolution, a over closely sampled frequency range, of $C_2 - C_1$.

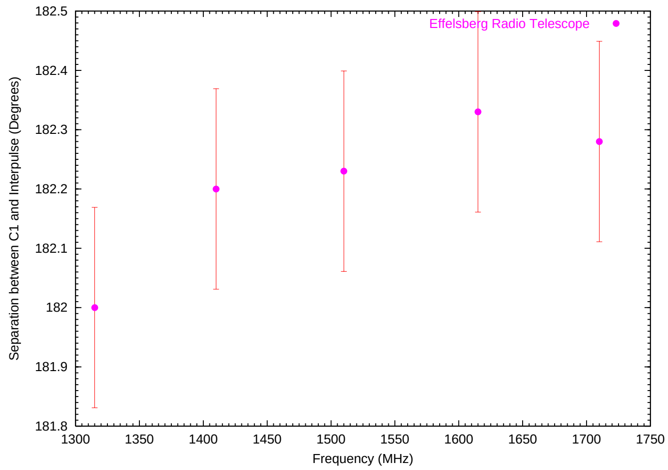

Figure 4.11: PSR B1702-19: Separation between C_1 and the inter-pulse.

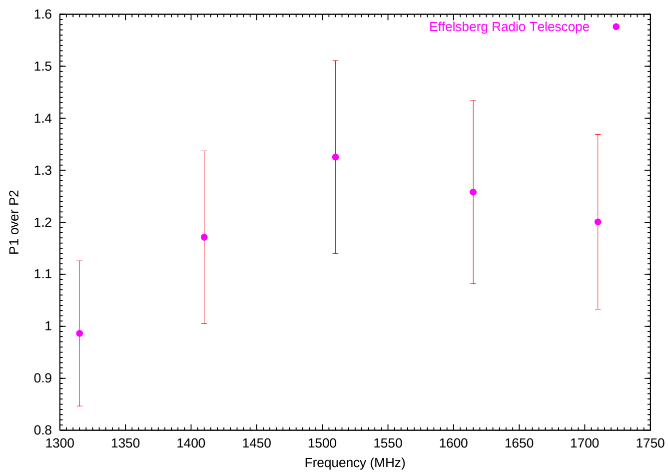

Figure 4.12: PSR B1702-19: ratio of P_1 over P_2.

Separation between C_1 and the inter-pulse

What happens with the separation between C_1 and the inter-pulse, is illustrated in Figure 4.11.

Evolution of ratio of P_1 over P_2

Interestingly, the ratio of P_1 over P_2 seems to be characterized by a different regularity than the one that seemed to dominate in the evolution of widths. This becomes clear with Figure 4.12.

Ratio P_1 or P_2 over P_{IP}

In Figures 4.13 and 4.14 we plot the ratio of P_1 and P_2 over P_{IP} respectively.

A brief discussion

Although in all of the above cases the errors are large, a regularity seems to be present. As we already pointed out, what is noteworthy is that properties of the same sort (for example the widths) display the similar behavior. Therefore, it is reasonable for a scholar to become suspicious of a regularity hidden in the above observations.

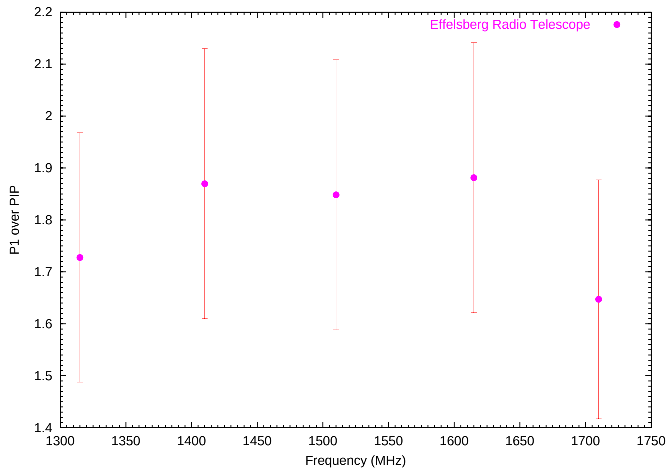

Figure 4.13: PSR B1702-19: ratio of P_1 over P_{IP}.

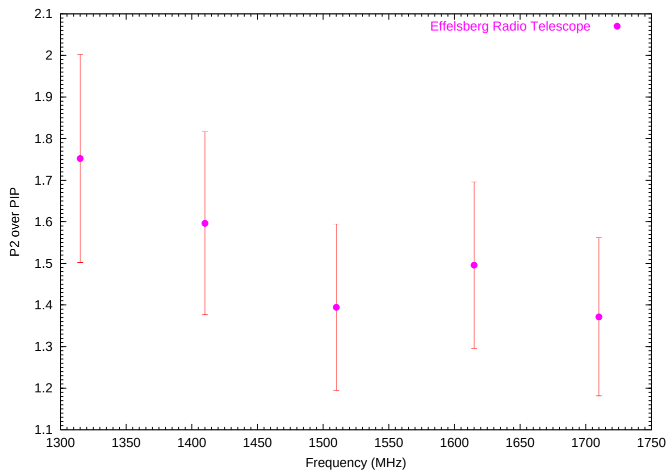

Figure 4.14: PSR B1702-19: ratio of P_2 over P_{IP}.

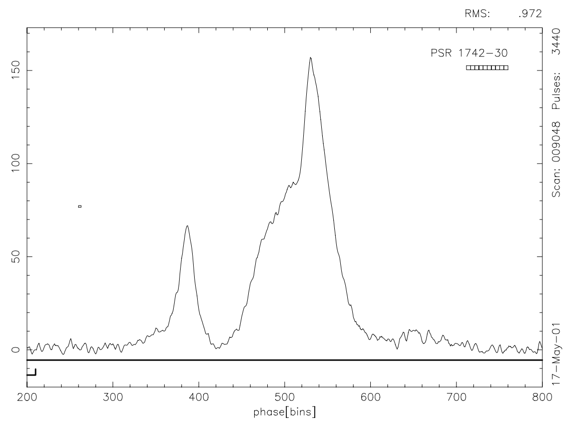

Figure 4.15: PSR B1742-30: A typical Effelsberg observation at 1420 MHz.

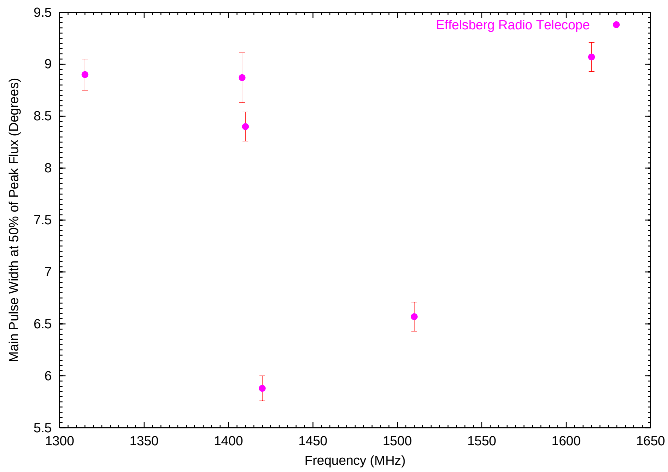

Figure 4.16: PSR B1742-30: Main pulse's observational $f - W_{50\%}$ points (Effelsberg data).

4.2 PSR B1742-30

General information about PSR B1742-30 is given in Section 3.4.

4.2.1 Integrated profile study

The frequencies used, are: 1315, 1408, 1410, 1420, 1510 and 1615 MHz. As in Section 3.4 we study the precursor separately from the main pulse (see Figure 4.15).

Widths

The first to examine is the widths, as usually, for both the main pulse and the precursor. Figures 4.16, 4.17 and 4.18 are associated with the main pulse. On the other hand, Figures 4.19, 4.20 and 4.21 correspond to the precursor.

Evolution of $P_{mainpulse}/P_{precursor}$

In Figure 4.22 we give the observed evolution of the ratio $P_{mainpulse}/P_{precursor}$. It is noteworthy the fact that though a tendency of the points to follow a power law is implied, the calculations of the parameters a and b of such a model displayed huge errors. That is the reason for not presenting that plot.

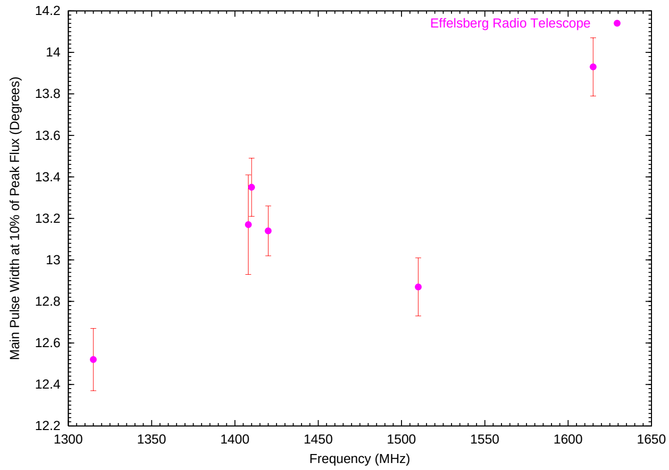

Figure 4.17: PSR B1742-30: Main pulse's observational $f - W_{10\%}$ points (Effelsberg data).

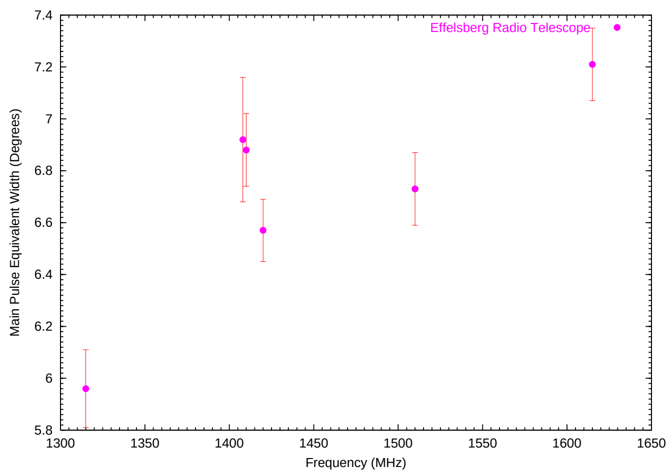

Figure 4.18: PSR B1742-30: Main pulse's observational $f - W_{eq}$ points (Effelsberg data).

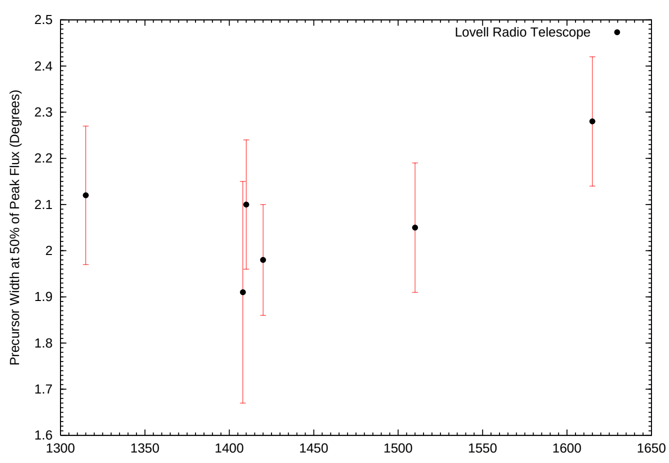

Figure 4.19: PSR B1742-30: Precursor's observational $f - W_{50\%}$ points (Effelsberg data).

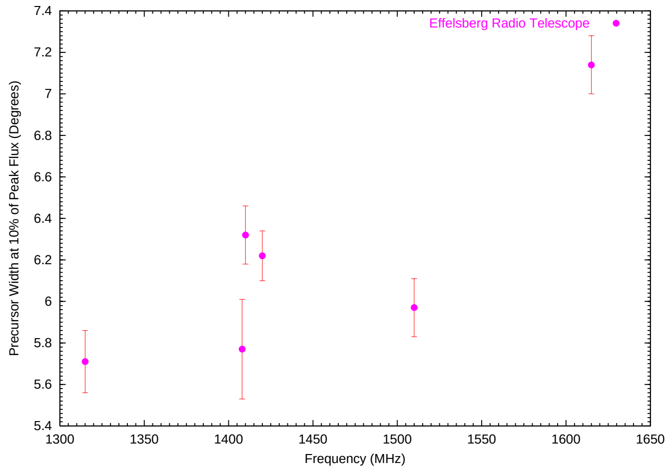

Figure 4.20: PSR B1742-30: Precursor's observational $f - W_{10\%}$ points (Effelsberg data).

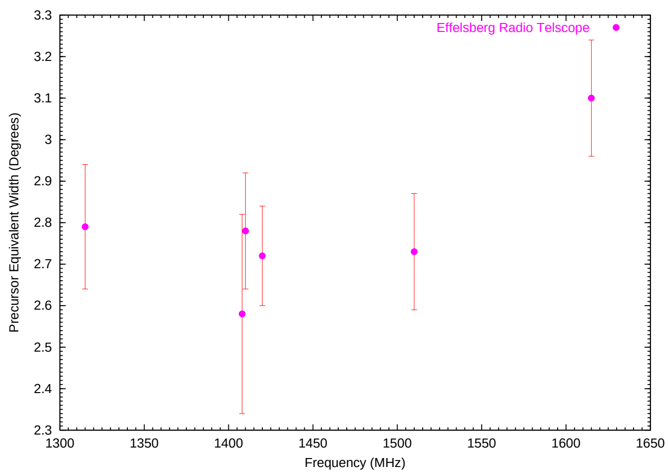

Figure 4.21: PSR B1742-30: Precursor's observational $f - W_{eq}$ points (Effelsberg data).

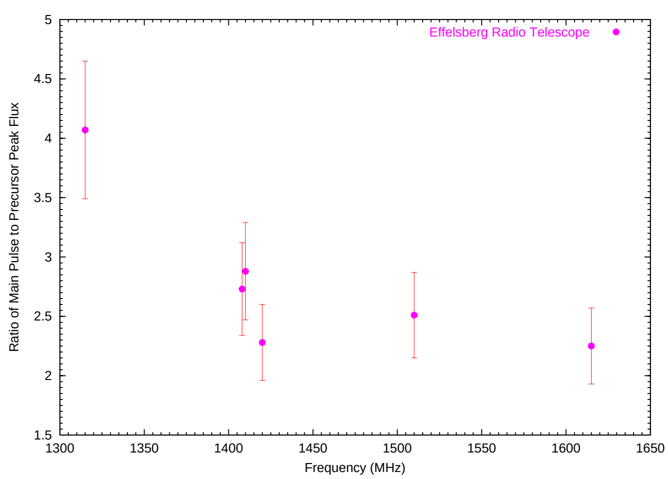

Figure 4.22: PSR B1742-30: The evolution of $P_{mainpulse}/P_{precursor}$.

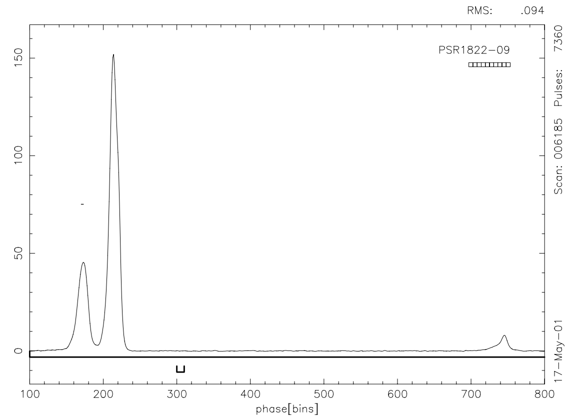

Figure 4.23: PSR B1822-09 : Typical Effelsberg observation at 1408 MHz.

A brief discussion

Although, once again, no power law is present, the behavior of observational points appears to be regular. We are of the opinion that the most important thing one could mention here, is the dramatic changes that happen around $1400\ MHz$.

4.3 PSR B1822-09

The general characteristics of PSR B1822-09 have already been presented in Section 3.5. Therefore, it is meaningless to repeat the same information here.

4.3.1 Integrated profile study

The frequencies used in this study were: 1315, 1408, 1615 and $4750\ MHz$. Keep in mind that at this phase of our report we give the results from the analysis based only on Effelsberg observations. A quick look through Figure 4.23 may be useful to refresh the memory about its profile.

The widths

In the present paragraph we gather together all the plots that involve the evolution of widths. Figure 4.24 illustrates the evolution of main pulse's $W_{50\%}$. The plot in Figure 4.25 shows the evolution of the overall W_{eq}. That is, apart from the main pulse the precursor was in the fitting range as well. In that plot we also give the fitted power law that corresponds to the parameters:

$$a = 14\ \frac{Degrees}{MHz^{-b}} \pm 0.1,\ b = -0.091 \pm 0.001 \tag{4.1}$$

Separations

At this point we report the results concerning the separations. Particularly, in Figure 4.26 we present the correlation between f and $C_{mainpulse} - C_{precursor}$. In 4.27 that between f and $C_{mainpulse} - C_{inter-pulse}$. Finally, in Figure 4.28 we give the evolution of $C_{precursor} - C_{inter-pulse}$.

Ratios

The ratio $P_{mainpulse}/P_{precursor}$ evolves as shown in Figure 4.29. Figure 4.30 displays the evolution of $P_{mainpulse} - P_{inter-pulse}$.

4.4 PSR B1831-04

The general information about PSR B1831-04 has already been given in Section 3.6.

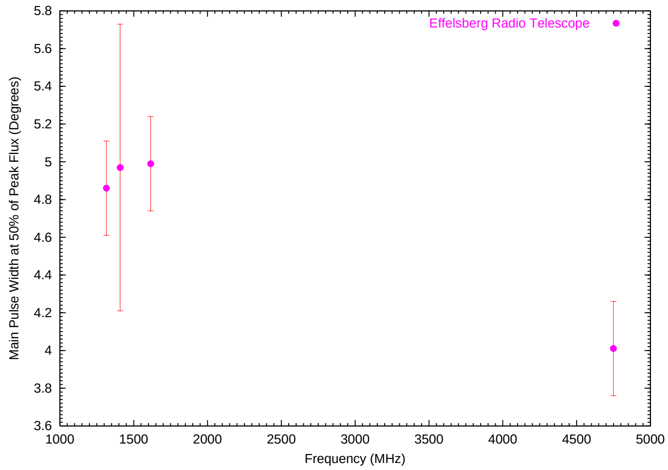

Figure 4.24: PSR B1822-09: The evolution of main pulse's $W_{50\%}$

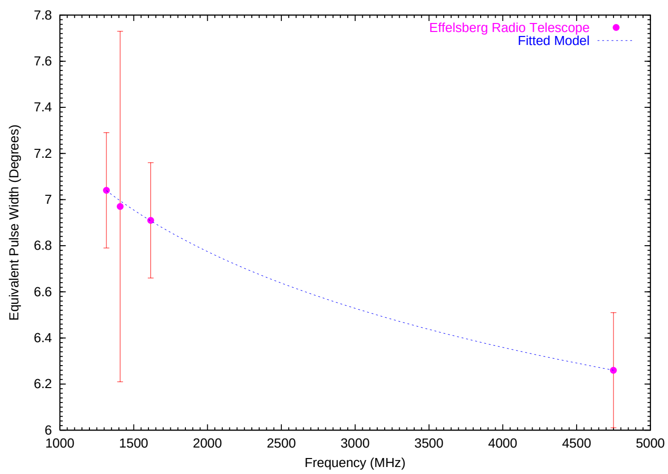

Figure 4.25: PSR B1822-09: The overall W_{eq} and the fitted power law.

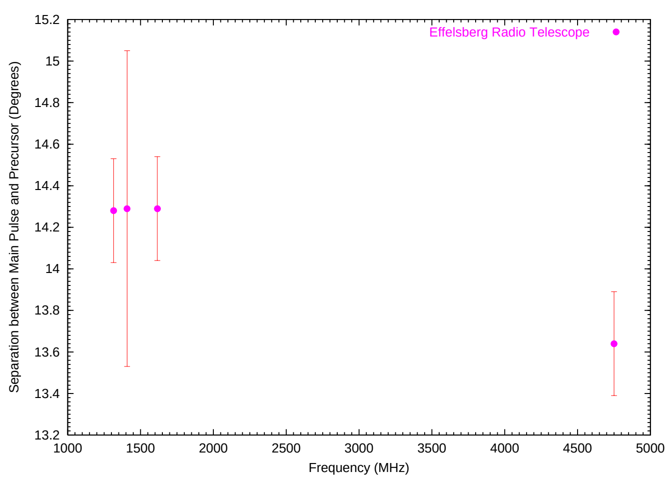

Figure 4.26: PSR B1822-09: The correlation between f and $C_{mainpulse} - C_{precursor}$.

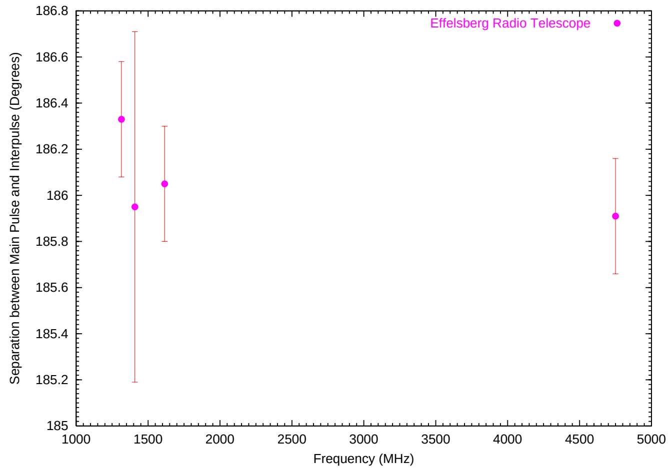

Figure 4.27: PSR B1822-09: The correlation between f and $C_{mainpulse} - C_{inter-pulse}$.

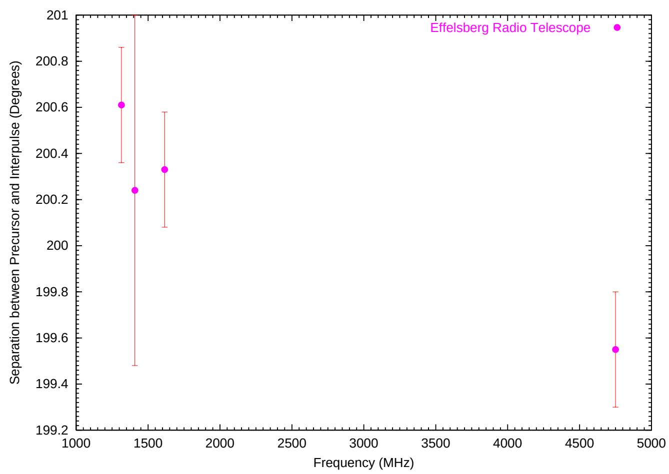

Figure 4.28: PSR B1822-09: The evolution of $C_{precursor} - C_{inter-pulse}$.

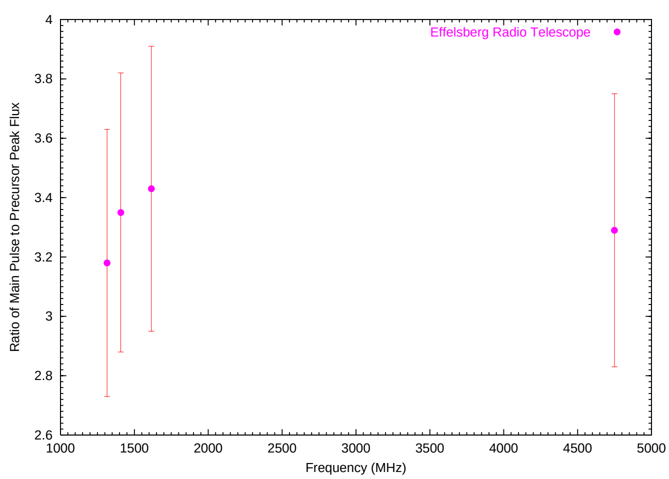

Figure 4.29: PSR B1822-09: The evolution of $P_{mainpulse} - P_{precursor}$.

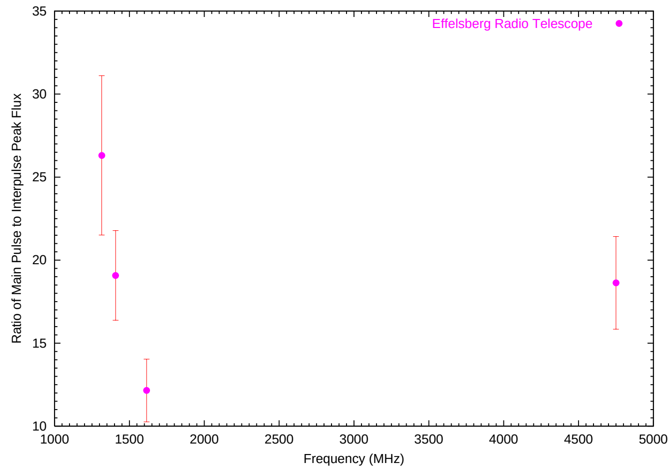

Figure 4.30: PSR B1822-09: The evolution of $P_{mainpulse} - P_{inter-pulse}$.

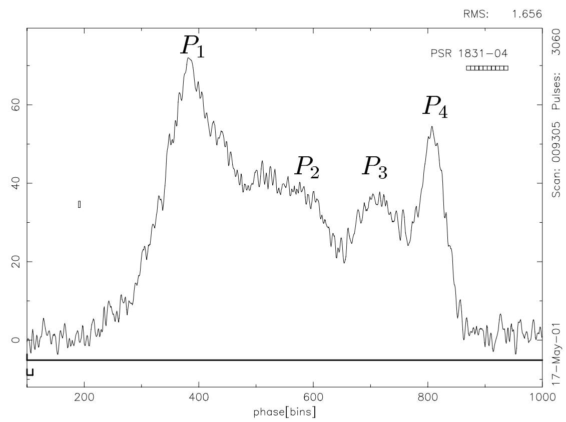

Figure 4.31: PSR B1831-04 : Typical Effelsberg observation at 1420 MHz.

4.4.1 Integrated profile study

An observation obtained with the Effelsberg Radio Telescope at $1420\ MHz$ is presented in Figure 4.31. The frequencies that used for its study, are: 1315, 1420, 1510 and $1710\ MHz$.

Equivalent pulse width

Figure 4.32 illustrates the results concerning the equivalent pulse width.

Separations

Let us present Figures 4.33 and 4.34 which describe the evolution of $C_3 - C_1$ and $C_4 - C_1$ over frequency, respectively.

Ratios

Figures 4.35 and 4.36 summarize the evolution of ratios.

A brief discussion

The plots presented above, make clear that PSR B1831-04 is a typical example of fast changes. Therefore, it would be very illuminating to investigate what is the reason for these modifications of the profile.

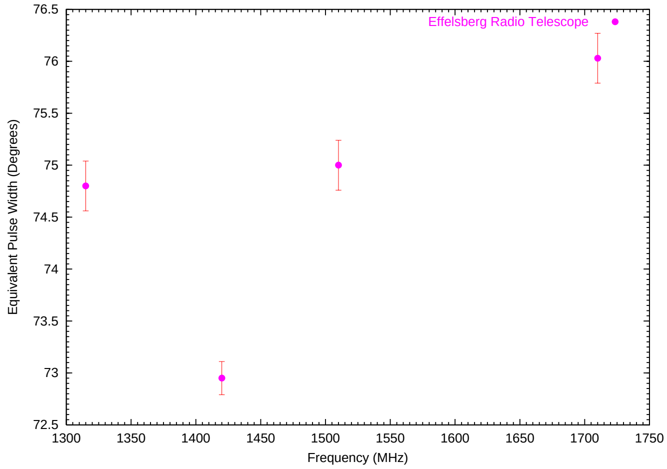

Figure 4.32: PSR B1831-04: The evolution of W_{eq}.

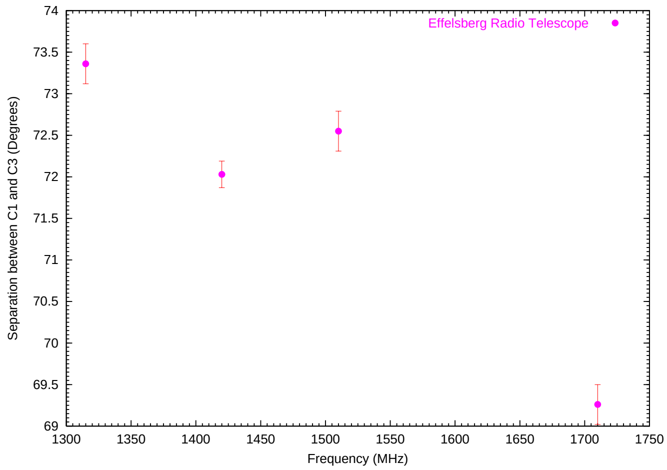

Figure 4.33: PSR B1831-04: The evolution of $C_3 - C_1$.

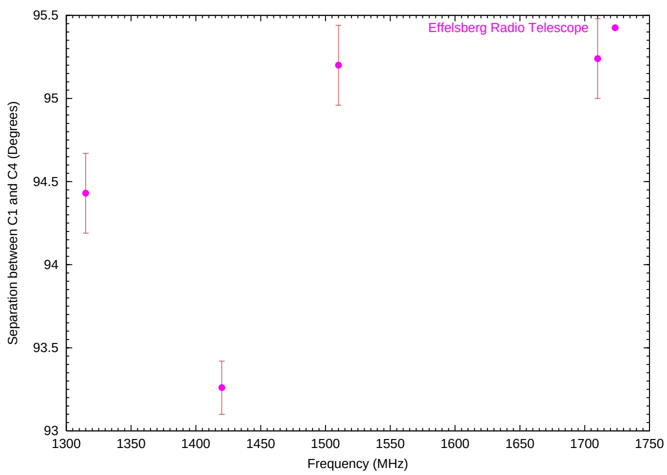

Figure 4.34: PSR B1831-04: The evolution of $C_4 - C_1$.

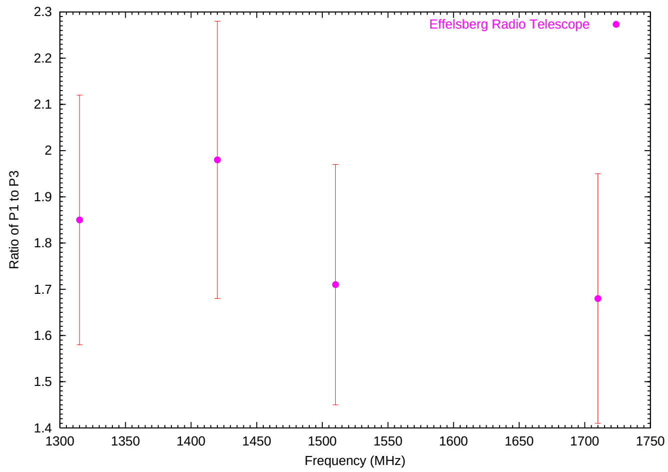

Figure 4.35: PSR B1831-04: The evolution of P_1/P_3.

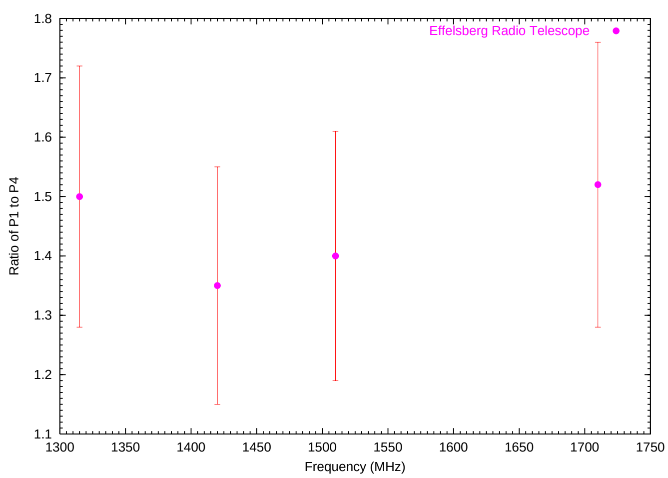

Figure 4.36: PSR B1831-04: The evolution of P_1/P_4.

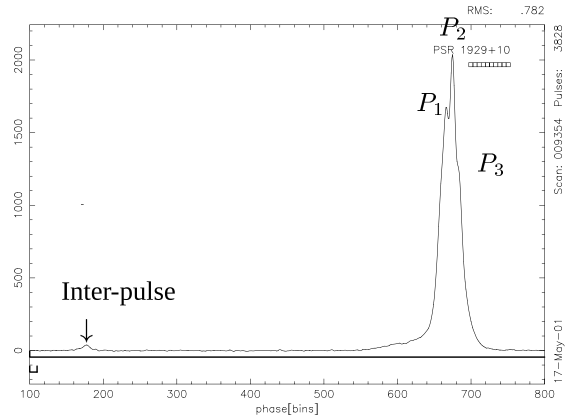

Figure 4.37: PSR B1929+10 : Typical Effelsberg observation at 1420 MHz.

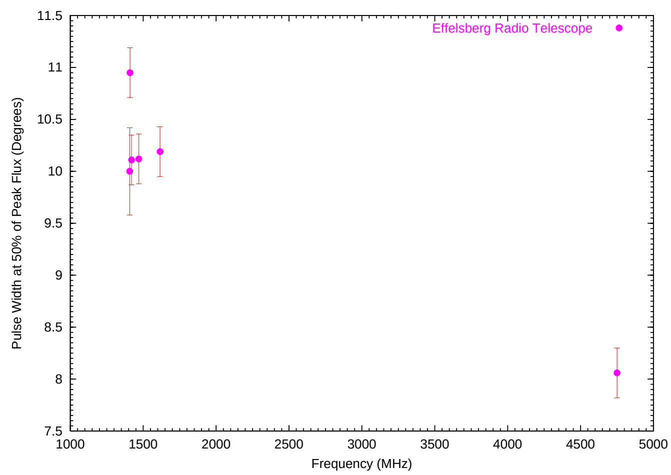

Figure 4.38: PSR B1929+10: The evolution of main pulse's $W_{50\%}$.

4.5 PSR B1929+10

Using observations carried out at Effelsberg we studied the behavior of PSR B1929+10 at 1408, 1410, 1420, 1470, 1615 and 4750 MHz. General information about it is available in Section 3.7.

4.5.1 Integrated profile study

Before proceeding, it would be useful to inspect a typical Effelsberg profile of PSR B1929+10 (see Figure 4.37). Comparing it with an observation with the Lovell telescope clearly demonstrates the importance of time resolution. This discussion has already been done in detail in Section 3.7.2.

Widths

Due to data insufficiency in the following we present widths' measurements for the main pulse, only. Figures 4.38, 4.39 and 4.40 reveal the interesting evolution of $W_{50\%,10\%,eq}$ respectively.

Separations and ratios

Figure 4.41 displays the correlation between the frequency and $C_2 - C_1$ whereas 4.42 that between f and P_2/P_1. Finally, in Figure 4.43 the ratio $P_2/P_{inter-pulse}$ is shown.

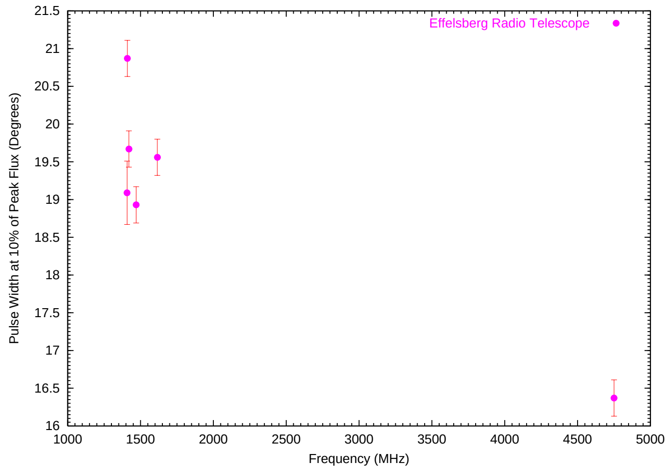

Figure 4.39: PSR B1929+10: The evolution of main pulse's $W_{10\%}$.

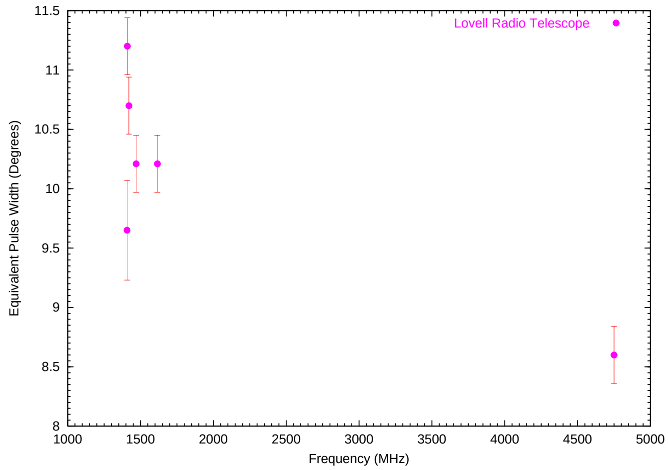

Figure 4.40: PSR B1929+10: The evolution of main pulse's W_{eq}.

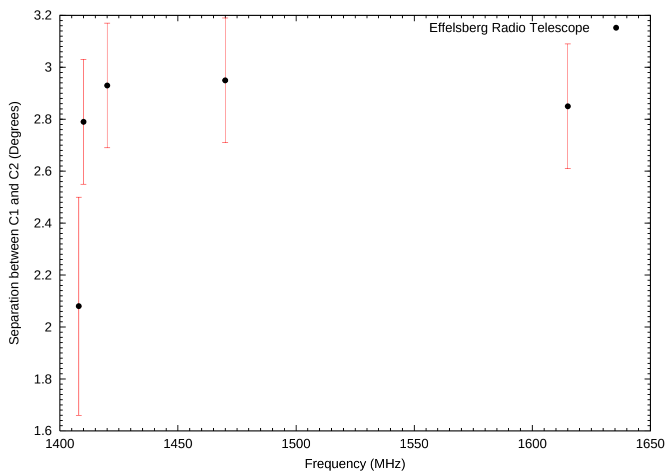

Figure 4.41: PSR B1929+10: The evolution of $C_2 - C_1$.

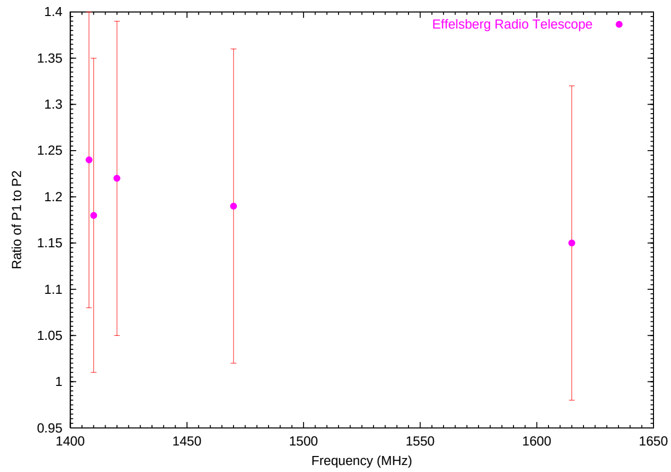

Figure 4.42: PSR B1929+10: The evolution of P_2/P_1.

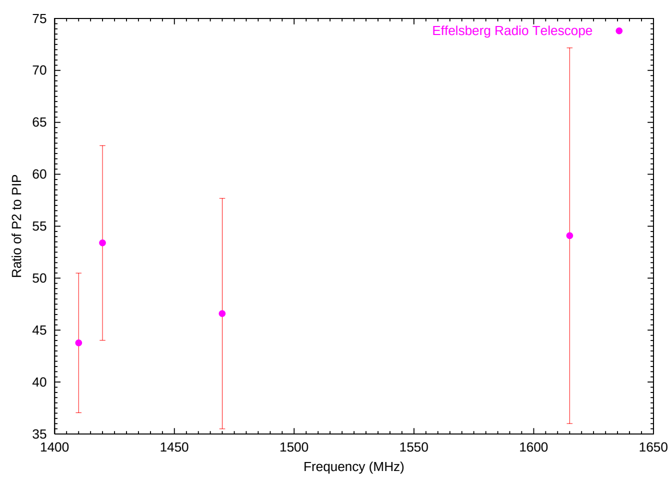

Figure 4.43: PSR B1929+10: The evolution of $P_2/P_{inter-pulse}$.

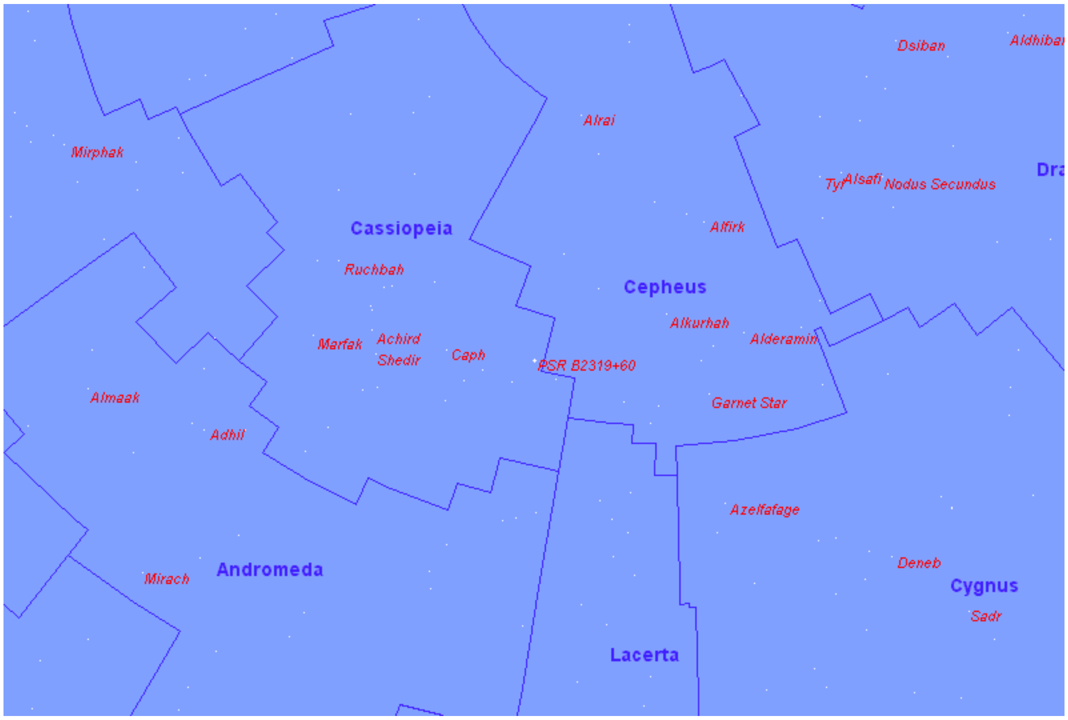

Figure 4.44: PSR B2319+60: Its location in the constellation of Cassiopeia.

A brief discussion

What is the most noteworthy to mention here, is the fast changes observed at around 1400 MHz. A further discussion about this issue will follow in Chapter 5.

4.6 PSR B2319+60

The reader will realize that it is the first time to mention PSR B2319+60. Although, only its $W_{10\%}$ and W_{eq} have been examined, we share the opinion that their evolution is very interesting. Hopefully, this is revealed during the following report. x

4.6.1 General information about PSR B2319+60

PSR B2319+60 is located in the constellation of Cassiopeia, 3.2 kpc from the Sun. Its DM is about 95 $cm^{-3}pc$ and its period roughly $2256.488\ ms$. Its slowdown happens at a rate of about $7{\cdot}10^{-15}\ s/s$ implying a characteristic age of about $5.1{\cdot}10^{6}\ years$. At 400 MHz it gives a mean flux density of about 36 mJy and at 1400 MHz about 12 mJy.

4.6.2 A discussion about profile morphology

In Figure 4.45 we present a typical 1410-MHz observation. As shown there, its wide profile is interestingly complicated. Due to dramatic changes of the profile that we have noticed to happen, we only study $W_{10\%}$ and equivalent pulse width. Nevertheless, an amazingly regular behavior has been disclosed to us.

4.6.3 Integrated profile study

The frequency range available for the study of PSR B2319+60, together with PSR B1702-19, was the most complete among that corresponding to the rest of the stars we studied. In detail, we have used 1315, 1420, 1510, 1615 and 1710 MHz. Based on these data we present the evolution of $W_{10\%}$ and W_{eq}. It is fundamental to notice that due to its long period (2.2 s), the number of averaged individual pulses is not very large.

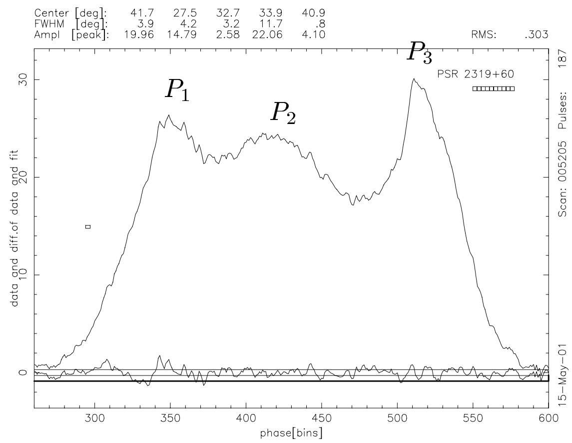

Figure 4.45: PSR B2319+60 : A typical 1410-MHz Effelsberg observation.

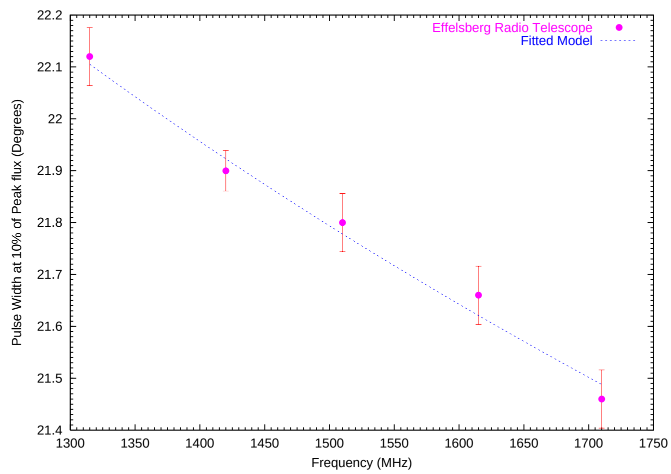

Figure 4.46: PSR B2319+60: The evolution of $W_{10\%}$ and the fitted power law.

The evolution of $W_{10\%}$

In Figure 4.46 we give the evolution of $W_{10\%}$. Its tendency to follow a power law is obvious. We have fitted the observational points with a power law of:

$$a = 48 \, \frac{Degrees}{MHz^{-b}} \pm 3, \; b = -0.108 \pm 0.008 \tag{4.2}$$

It appeared to us interesting to attempt a linear fit as well. That is, we tried to fit a straight line of the form $W_{10\%} = a \cdot f + b$. The calculated a and b, were:

$$a = -0.002 \, \frac{Degrees}{MHz} \pm 0.0001, \; b = 24 \; Degrees \pm 0.2 \tag{4.3}$$

In Figure 4.47 we give the derived plot.

The evolution of W_{eq}

In Figure 4.48 we present the last plot. It describes the evolution of W_{eq}.

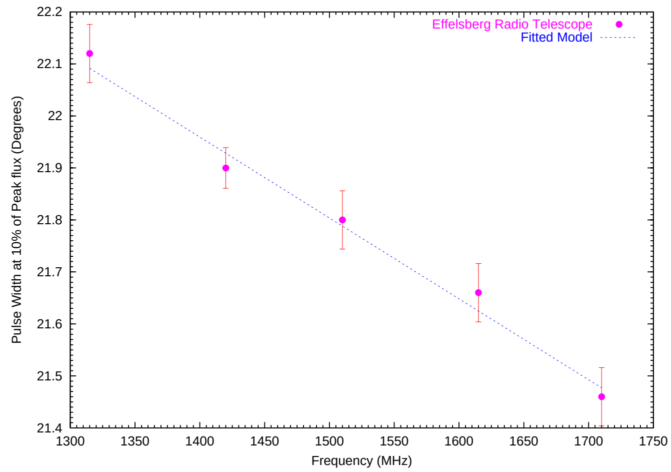

Figure 4.47: PSR B2319+60: The evolution of $W_{10\%}$ plus the fitted straight line.

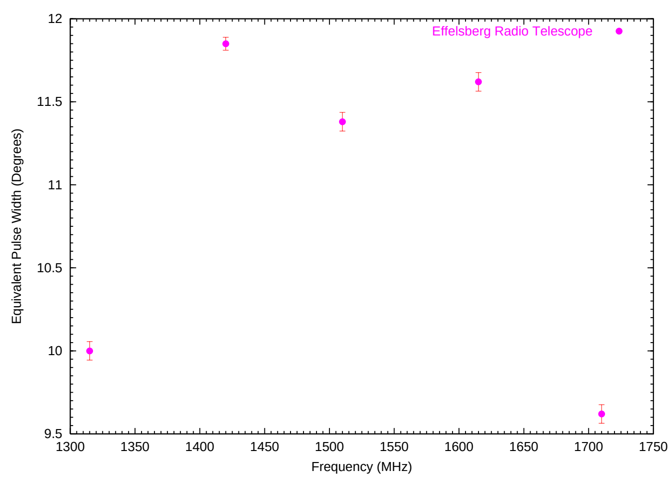

Figure 4.48: PSR B2319+60: The evolution of W_{eq}.

Chapter 5

An Overall Discussion

In the present chapter we try to point out the most outstanding issues we came across during the above study. The detailed investigation of our analysis conclusions is not the intention of this report. An extended examination of our results will be undertaken in the future.

5.1 General Remarks

Often in the previous presentation, it was mentioned that the tendency of properties of the same sort to follow qualitatively similar development, was regarded as a strong evidence for the correctness of our analysis method. Moreover, we are of the opinion that, in the cases of smooth development, an unexpected hidden law may govern the behavior of the observational data.

As one can easily notice from the above presentation, the errors characterizing the observations are large. Therefore, a skeptical reader could assume, for instance, a linear correlation to describe the smooth evolution of some of the properties we have studied rather, than a power law as we actually did. The above statement is undoubtedly reasonable. Nevertheless, provided the, at least at first sight, correctness of the theory proposed by Smith, we share the opinion that the first to be investigated is the existence of a power law. Besides, the tendency of the observational points to follow a power law decay, is obvious in some cases (see Section 3.1).

5.2 Broadly Sampled Frequency Range

In the context of the study of the profile evolution over a broadly sampled frequency range, we searched for a power law to describe the observations. It is of great importance to point out that the exponential decay is expected, according to Smith, only for the measures of beamwidth (such as the widths or the separation between individual components). That is, the power law is not expected to fit the development of ratios.

Extending the discussion about the power law, it is crucial to mention the following. Whenever a power law seemed to be suitable to fit the data, the function of the simple form $beamwidthmeasure \propto a\ cdot f^{\,b}$ was tested as well as that of the form $beamwidthmeasure \propto a\ cdot f^{\,b}+c$ (power law with offset). Although it is not obvious at first sight, the two above functions differ substantially. That is, the former formula forces the model to go to infinity or to zero when the observing frequency goes to zero or to infinity respectively. Provided that a beamwidth measure is of finite and well determined value at very low frequencies, one could state that it is a mistake to try to fit a simple power law (without an offset) to the actual data. In pure mathematical language, this is completely true. Still, since we are interested in the investigation of the behavior of the observations within a finite and particular frequency range, it is not mistaken to regard the fitted model as a segment of a general curve neglecting its development outside the frequency limits determining the range under examination. All the above in conjunction to the inability of the fitting algorithm to give precise results when the given observational points are of small number, allowed us to restrict our calculations to the estimation of a power law without an offset only.

Concentrating on the actual results of our study, we should mention the following. From the seven pulsars studied over the broadly sampled frequency range, only PSR B0525+21 displayed a purely exponential development (see Section 3.1). PSR B1742-30, 1822-09, 1831-04 and 1929+10 display such a behavior only in a few cases. Therefore, an overall conclusion could be that the theory proposed by Smith, is not that obviously general. Of course, the bigger the studied population of pulsars is, the more secure such a statement is.

As for PSR B0525+21, its $W_{50\%}$ develops with an exponent b of about $-1/10$ which significantly differs from $-1/6$ which is expected. Even worst approximation is displayed by $W_{10\%}$ which develops with an exponent of roughly 11.On the other hand, W_{eq} behaves as a power law of $b = -1/5.3$ which is not far from the expected value. In good agreement with the theory is the separation between C_1 and C_2, as well. In this case b is close to $-1/7.7$.

Good approximation of the theory is possessed by the development of main pulse's $W_{50\%}$ in the case of PSR B1822-09. The calculated value for b is about $-1/7$. In the case of PSR B1929+10 this property changes with a b of about $-1/8.3$.

5.3 Closely Sampled Frequency Range

Switching to the study over a closely sampled frequency range, we recall that what we are interested in is to examine whether the observed changes to the profile happen fast or gradually.

PSR B1742-30, 1822-09 and 1929+10 are the pulsars that, among the six ones studied, are characterized by rather fast modifications of the profile. The rest of the pulsars seem to develop more smoothly. Therefore, it is not trivial to state a general conclusion.

Of great importance is the comment that, in the cases of fast changes, $1400\ MHz$ seem to be a crucial observing frequency. A careful examination of the derived plots reveals that dramatic changes happen around this frequency.

5.4 Future Plans

In our point of view, apart from giving some evidence about how the integrated profile develops over a broadly or closely sampled frequency range, the study we have carried out brings to light new questions and therefore ideas for future projects.

The first to mention is the necessity for a detailed examination of what happens when fast changes are observed. To put it simply, does the pulsar displays *mode changing* having new components appearing, or not?

It is of outstanding importance to carefully examine the derived values of a and b and try to correlate them with physical quantities characteristic of neutron stars. This may even lead to the proposition of a new model (other than the one proposed by Smith). The idea to search for an alternative model is supported by the observation that, in many cases, a smooth development is present though a power law is absent.

Further, as we already occasionally mentioned, in the case of fast changes these seem to take place around $1400\ MHz$. Therefore, observations at as many frequencies around 21 cm as possible, would likely prove illuminating.

Appendix A

Complete Data Catalogues

Here we have gathered together all the data tables associated with the pulsars we have studied. It may be helpful for the reader to consult in the present Chapter and retrieve any information that he may need.

Table A.1: The data used in the study of PSR B0525+21.

Frequency (MHz) :	408	606	910	1408	1667	4850
Telescope :	L	L	L	L	L	E
De-dispersion channel						
Bandwidth (MHz) :	0.125	0.125	0.25	1	5	500
Despersion Broadening (ms):	0.777	0 .237	0.140	0.151	0.456	1.85
Sampling Interval (μs):	9362.9	9364.7	9364.7	9364	9363.2	1500
Factor (deg/bin) :	0.9	0.9	0.9	0.9	0.9	0.144172
RMS :	0.433	0.011	0.528	0.002	0.044	1.709
Number of Pulses :	23744	858	14872	1488	2205	948
Calibration Status :	no	yes	no	yes	no	no
$W_{50\%}$ (deg) :	19	18.06	17.31	16.64	16.29	13.52
$W_{10\%}$ (deg) :	22.63	21.56	20.82	20.26	19.84	15.58
W_{eq} (deg) :	10.96	9.89	8.99	8.54	8.38	3.68
C_1 (bins) :	184.71	185.5	186.9	187.54	187.62	717.09
P_1 (Jy) :	128.64	1.77	65.62	0.31	11.22	90.50
C_{Bridge} (bins) :	193	193	195	194.5	194	–
P_{Bridge} (Jy) :	17.07	0.12	7.11	0.033	1.34	–
C_2 (bins) :	200.84	200.87	201.42	201.34	201.13	793.99
P_2 (Jy) :	127.41	1.91	80.75	0.41	14.23	154.98

Table A.2: The data used in the study of PSR B0540+23.

Frequency (MHz) :	410	606	926	1376	1412	1642	1315	1408	1420
Telescope :	L	L	L	L	L	L	E	E	E
De-dispersion channel Bandwidth (MHz) :	0.125	0.25	0.25	3	3	5	0.6667	0.6667	0.6667
Dispersion Broadening (ms):	1.17	0.72	0.2	0.74	0.2	0.73	0.189	0.154	0.15
Time resolution (μs):	614.9	615	614.9	614.9	614.9	615	240	240	100
Factor (deg/bin) :	0.9	0.9	0.9	0.9	0.9	0.9	0.35125558	0.3512563	0.1463567
RMS :	0.003	0.003	0.328	0.0	0.002	0.001	4.889	8.528	2.470
Number of Pulses :	10944	43812	10122	17496	7290	14460	780	1860	1200
$W_{50\%}$ (deg) :	9.33	8.4	8.34	9.13	8.88	9.53	6.7	7.35	7.2
$W_{10\%}$ (deg) :	27.61	23.71	24.30	24.79	25.01	25.89	21.83	22.66	21.99
W_{eq} (deg) :	12.23	10.99	11.19	11.77	11.78	12.27	9.49	9.95	9.74

Table A.3: The data used in the study of PSR B0740-28.

Frequency (MHz) :	234	326	413.9	606	925	1396	1420	1594	1606	1616	1642	1710	4700
Telescope :	L	L	L	L	L	L	L	L	L	L	L	E	E
De-dispersion													
channel Bandwidth (MHz) :	0.03125	0.03125	0.125	0.125	0.25	1	5	5	5	1	5		
Dispersion Broadening (ms):	1.49	0.55	1.08	0.34	0.19	0.23	1.07	0.76	0.74	0.15	0.69		
Time resolution (μs) :	416.9	416.9	416.9	416.9	416.9	416.9	416.9	416.9	416.9	416.9	416.9	160	160
Factor (deg/bin) :	0.9	0.9	0.9	0.9	0.9	0.9	0.9	0.9	0.9	0.9	0.9	0.35	0.35
RMS :	0.031	0.448	0.639	0.002	0.005	0.001	0.001	0.003	0.003	0.278	0.001	1.586	0.195
Number of Pulses :	9526	21338	9702	61278	19206	12924	18818	9927	6402	12936	1378	7120	7120
$W_{50\%}$ (deg) :	15.37	9.26	12.42	9.71	9.15	10.24	11.19	11.42	10.46	10.97	10.45	10.29	24.32
$W_{10\%}$ (deg) :	35.74	20.07	21.50	16.50	15.73	17.93	19.01	18.71	17.01	17.84	17.55	16.42	28.14
W_{eq} (deg) :	18.61	10.44	12.91	9.90	9.34	10.75	11.68	11.99	10.71	11.37	10.88	10.13	10.41

Table A.4: The data used in the study of PSR B1702-19.

Frequency (MHz) :	1315	1410	1510	1615	1710
Telescope :	E	E	E	E	E
De-dispersion channel					
Bandwidth (MHz) :	0.6667	06667	06667	06667	06667
Despersion Broadening (ms):	0.0558	0.0452	0.0368	0.0301	0.0254
Sampling Interval (μs):	200	200	200	200	200
Factor (deg/bin) :	0.24	0.24	0.24	0.24	0.24
RMS :	1.521	1.838	2.02	2.167	2.558
Number of Pulses :	3100	3100	3100	2100	1100
Calibration Status :	no	no	no	no	no
Main Pulse					
$W_{50\%}$ (deg) :	11.38	11.02	10.87	11.04	10.99
$W_{10\%}$ (deg) :	17.29	16.41	16.35	16.62	16.27
W_{eq} (deg) :	11.38	10.08	9.62	10.01	10.13
C_1 (bins) :	193.99	156.75	191.62	164.52	171.12
P_1 (Jy) :	381.88	361.99	362.06	597.84	214.55
C_2 (bins) :	217.53	181.56	216.14	189.73	195.99
P_2 (Jy) :	387.26	309.06	273.14	475.30	178.67
Interpulse					
$W_{50\%}$ (deg) :	2.41	2.11	2.2	2.12	2.26
$W_{10\%}$ (deg) :	5.88	5.48	5.48	5.49	5.87
W_{eq} (deg) :	2.94	2.7	2.71	2.66	2.82
C_{IP} (bins) :	952.33	915.93	950.91	924.23	930.60
P_{IP} (Jy) :	221.02	193.6	195.88	317.78	130.26

Table A.5: The data used in the study of PSR B1742-30.

Frequency (MHz) :	410	606	925	1380	1412	1642	1315	1408	1410	1420	1510	1615
Telescope :	L	L	L	L	L	L	E	E	E	E	E	E
De-dispersion channel												
Bandwidth (MHz) :	0.125	0.25	0.25	3	1	5	0.6667	0.6667	0.6667	0.6667	0.6667	0.6667
Despersion Broadening (ms):	1.33	0.82	0.23	0.84	0.26	0.83	0.22	0.18	0.17	0.17	0.14	0.12
Sampling Interval (μs):	918.6	918.5	918.6	918.5	918.5	918.5	200	350	200	100	200	200
Factor (deg/bin) :	0.9	0.9	0.9	0.9	0.9	0.9	0.2	0.34	0.2	0.1	0.2	0.2
RMS :	0.012	0.005	0.008	0.002	0.002	0.001	2.094	9.976	3.248	1.356	3.448	3.685
Number of Pulses :	6348	40986	8712	9780	15648	12100	880	480	880	3440	880	880
Calibration Status :	yes	yes	yes	yes	yes	yes	no	no	no	no	no	no
Main Pulse												
$W_{50\%}$ (deg) :	7.21	6.38	6.67	8.64	8.41	9.06	8.9	8.87	8.4	5.88	6.57	9.07
$W_{10\%}$ (deg) :	15.7	13.53	13.11	15.88	15.8	15.82	12.52	13.17	13.35	13.14	12.87	13.93
W_{eq} (deg) :	8.25	7.30	7.31	8.95	8.81	9.28	5.96	6.92	6.88	6.57	6.73	7.21
C_{MP} (bins) :	201.19	200.8	200.76	200.83	200.83	200.71	790.63	320.28	308.75	530.96	523.02	418.9
P_{MP} (Jy) :	2.99	2.03	1.69	0.74	0.77	0.35	516.4	1710.71	419.43	200.2	451.51	309.96
Precursor												
$W_{50\%}$ (deg) :	4.94	3.94	3.94	4.61	4.85	4.48	2.12	1.91	2.1	1.98	2.05	2.28
$W_{10\%}$ (deg) :	–	7.52	7.6	–	–	–	5.71	5.77	6.32	6.22	5.97	7.14
W_{eq} (deg) :	5.25	4.27	4.3	5.12	5.48	5.03	2.79	2.58	2.78	2.72	2.73	3.1
C_{Pr} (bins) :	184.25	184.4	184.53	185.07	185.06	185.07	718.83	278.91	235.79	386.82	451.2	346.2
P_{Pr} (Jy) :	0.53	0.38	0.35	0.18	0.19	0.1	126.98	627.43	145.77	87.67	179.86	137.6

Table A.6: The data used in the study of PSR B1822-09.

Frequency (MHz) :	408	608	925	1380	1419.5	1616	1642	1315	1408	1615	4750
Telescope :	L	L	L	L	L	L	L	E	E	E	E
De-dispersion											
channel Bandwidth (MHz) :	0.125	0.125	0.25	3	1	1	5	0.6667	40	0.6667	0.6667
Dispersion Broadening (ms):	0.2972	0.0898	0.051	0.1844	0.0564	0.0383	0.1824	0.0474	2.315	0.0256	0.0010
Time resolution (μs) :	1922	1922	1922	1922	1922	1922	1922	750	750	750	750
Factor (deg/bin) :	0.9	0.9	0.9	0.9	0.9	0.9	0.9	0.35	0.35	0.35	0.35
RMS :	0.241	0.005	0.005	0.004	0.003	0.606	0.002	0.207	0.067	0.093	0.343
Number of Pulses :	24315	1872	4158	468	2808	2106	4389	2000	7360	1999	4680
Main Pulse											
$W_{50\%}$ (deg) :	6.34	6.41	5.95	5.33	5.73	5.21	5.42	4.86	4.97	4.99	4.01
C_{MP} (bins) :	201.19	201.64	201.12	200.71	201.11	201.13	201.3	228.05	213.78	206.47	315.73
P_{MP} (Jy) :	98.61	1.97	1.1	1.07	0.71	118.42	0.51	47.09	152.22	17.37	130.78
Precursor											
C_{Prcrsr} (bins) :	184.52	184.62	184.58	184.65	184.85	184.79	184.87	187.25	172.95	165.65	276.76
P_{Prcrsr} (Jy) :	8.28	0.41	0.2	0.34	0.19	49.69	0.2	14.82	45.44	5.06	39.71
Interpulse											
C_{IP} (bins) :	8.02	8.95	7.84	7.68	8.09	7.51	8.37	760.43	745.06	738.03	846.90
P_{IP} (Jy) :	7.74	0.08	0.08	0.04	0.05	2.7	0.02	1.79	7.98	1.43	7.02
Overall											
W_{eq} (deg) :	7.26	8.24	7.76	8.1	8.05	8.48	8.64	7.04	6.97	6.91	6.26

Table A.7: The data used in the study of PSR B1831-04.

Frequency (MHz) :	411	606	1380	1404	1315	1420	1510	1710
Telescope :	L	L	L	L	E	E	E	E
De-dispersion channel Bandwidth (MHz) :	0.125	0.25	3	1	0.6667	0.6667	0.6667	0.6667
Time resolution (μs) :	725	725	725	725	280	180	280	280
Factor (deg/bin) :	0.9	0.9	0.9	0.9	0.35	0.22	0.35	0.35
RMS :	0.012	0.006	0.006	0.006	1.427	1.589	2.977	2.554
Number of Pulses :	40823	23342	18540	82052	3162	3060	3162	2142
C_1 (bins) :	153.97	156.65	200.89	201.25	601.22	383.47	457.82	287.71
P_1 (Jy) :	0.43	0.29	0.09	0.05	105.3	70.71	110.98	62.77
C_2 (bins) :	200.88	200.79	245.45	242.24	714.89	–	567.39	–
P_2 (Jy) :	0.77	0.35	0.5	0.03	70.63	–	66.75	–
C_3 (bins) :	242.33	238.57	282.14	281.91	810.81	710.86	665.11	485.59
P_3 (Jy) :	0.17	0.13	0.05	0.03	57.06	35.73	64.81	37.32
C_4 (bins) :	265.05	264.01	305.84	306.33	871.02	807.36	729.82	559.82
P_4 (Jy) :	0.34	0.2	0.06	0.03	70.31	52.21	78.46	41.31
W_{eq} (deg) :	47.83	64.51	69.33	72.36	74.80	72.95	75	76.03

Table A.8: The data used in the study of PSR B1929+10.

Frequency (MHz) :	237	325	410	611	925	1396	1418	1642	1408	1410	1420	1470	1615	4750
Telescope :	L	L	L	L	L	L	L	L	E	E	E	E	E	E
De-dispersion channel														
Bandwidth (MHz) :	0.125	0.125	0.125	0.125	0.25	1	1	5	40	0.6667	0.6667	0.6667	0.6667	0.6667
Despersion Broadening (ms):	0.25	0.096	0.048	0.014	0.008	0.01	0.009	0.03	0.378	0.006	0.006	0.006	0.004	0.0002
Sampling Interval (μs):	566.3	566.3	566.3	566.3	566.3	566.3	566.3	566.3	110	220	220	220	220	220
Factor (deg/bin) :	0.9	0.9	0.9	0.9	0.9	0.9	0.9	0.9	0.175	0.35	0.35	0.35	0.35	0.35
RMS :	0.059	4.604	0.027	0.008	0.009	0.003	0.004	0.005	0.639	3.534	3.978	2.387	3.343	0.093
Number of Pulses :	3168	2382	20632	14368	14267	7920	485122	4710	6600	4554	3828	4158	3960	3960
Calibration Status :	yes	no	yes	yes	yes	yes	yes	yes	n0	no	no	no	no	no
Main Pulse														
$W_{50\%}$ (deg) :	8.00	10.08	9.78	10.23	10.53	10.61	10.64	10.19	10	10.95	10.11	10.12	10.19	8.06
$W_{10\%}$ (deg) :	25.34	22.73	22.22	21.87	20.85	19.75	19.94	19.06	19.09	20.87	19.67	18.93	19.56	16.37
W_{eq} (deg) :	11.81	11.41	11.19	11.34	11.60	11.45	12.02	11.74	9.65	11.20	10.70	10.21	10.21	8.6
C_1 (bins) :	–	–	–	–	–	–	–	–	424.1	743.46	666.4	311.73	737.61	796.60
P_1 (Jy) :	–	–	–	–	–	–	–	–	79.77	2192.39	1677.93	486.95	521.33	26.88
C_2 (bins) :	200.33	200.73	200.83	200.5	200.67	200.16	200.43	199.73	440.74	751.42	674.76	320.16	745.74	–
P_2 (Jy) :	17.84	1228.35	20.40	4.74	3.32	3.77	4.53	1.24	98.91	2595.5	2041.57	579.61	597.20	–
C_3 (bins) :	206.75	206.73	–	–	–	–	–	–	–	–	–	–	–	803.07
P_3 (Jy) :	8.05	643.27	–	–	–	–	–	–	–	–	–	–	–	22.33
Inter Pulse														
$W_{50\%}$ (deg) :	5.57	–	5.99	6.13	6.32	5.62	5.8	4.24	–	3.89	4.02	–	–	–
$W_{10\%}$ (deg) :	–	–	–	–	–	10.62	–	7.67	–	–	–	–	–	–
W_{eq} (deg) :	5.6	–	6.32	6.37	6.19	6.02	6.35	4.3	–	4.76	4.76	–	–	–
C_{MP} (bins) :	8.21	–	8.36	7.06	7.63	7.54	7.87	6.87	–	254.55	177.08	853.3	250.95	–
P_{IP} (Jy) :	0.36	–	0.28	0.1	0.08	0.07	0.08	0.03	–	59.30	38.24	12.44	11.04	–

Table A.9: The data used in the study of PSR B2319+60.

Frequency (MHz) :	1315	1420	1510	1615	1710
Telescope :	E	E	E	E	E
De-dispersion channel					
Bandwidth (MHz) :	0.6667	0.6667	0.6667	0.6667	0.667
Despersion Broadening (ms):	0.2306	0.1832	0.1523	0.1245	0.1049
Sampling Interval (μs):	500	350	500	500	500
Factor (deg/bin) :	0.07977	0.05584	0.07977	0.07977	0.07977
RMS :	1.383	0.336	0.215	0.195	1.691
Number of Pulses :	180	532	299	1982	198
Calibration Status :	no	no	no	no	no
$W_{10\%}$ (deg) :	22.12	21.90	21.80	21.66	21.46
W_{eq} (deg) :	10.0	11.85	11.38	11.62	9.62

My gratitude to ...

Sincere feelings of unlimited gratitude and deep obligation accompany my thoughts whenever I recall the support I received from specific persons during the fairly painful, but still amazing, days of the previously presented project.

I owe my thankfulness to the reader that dedicated some of her or his precious time to the study of my report. Time is irreversible and hence its consumption may sometimes be even a sacrifice.

Great honor and pure respect are words that sound so poor to express my feelings for Professor John Hugh Seiradakis, working with whom was far more than merely being supervised. I was taken by the most happily valuable surprise in the last 4 years, when I first met him personally. He is the person that, thank God, unfolded a completely fresh and unbelievably valuable attitude in front of my eyes. I beg his kindness to allow me not to hesitate to regard him as an opinion leader that revealed to me a way of living determined by values of vital importance and outstanding gentleness. Hopefully, someday he may understand how hard I had been working in silence with a single expectation: to give myself the illusion of being eligible to work by his side. I finish this paragraph thanking him not for being there whenever or for whatever I needed, but rather for being everywhere in my life[1].

Trying to find some words to describe my feelings for Dr. Michael Kramer, is like trying to empty an ocean using only a tea cup. I had the opportunity to work under his supervision during the winter of 2000 at Jodrell Bank observatory. Since then, I keep on wondering “does Michael have the *time machine*?” A smile always went up on his face before helping me even with the most trivial and boring problems I came across. His affection and patience made the days of hard working seem like holiday in wet Cheshire. I thank him with all my heart.

It is not easy at all to express my thankfulness to Professor Andrew Lyne. Despite the huge number of his responsibilities, he always found enough time to dedicate to my boring questions. I regard myself so privileged to have the honor to work in the scientific group of a legend such as Andrew. His presence in the Wednesday pulsar lunches made them remain in my memory as an unbelievable experience.

What more exciting could I ask for than interfering with scientists like Professor Sir Fransis Graham-Smith? A reference to his name is an excitement itself. Moreover, Sir Fransis played a crucial role in the progress of our project. He carried out himself the theoretical calculations we have previously presented. But most of all, I deeply thank him for exciting my inspiration every time, while keeping his eyes slightly closed, he made those surprisingly wise questions and comments during the pulsar lunches.

Every time I recall the hard times I had during my staying at Jodrell Bank Observatories, whatever the reason for them may have been, I realize that Dr. Bhal Chandra Joshi was always there to alleviate my pain. Constantly with a sincerely gentle smile on his face, Bhal, was a lot more than a friend. He was an angel. His goodness and pure kindness turned any problem into a trivial matter, that time would cure. How can I ever forget the moments of non-stop laughter, those of sharing sincere thoughts and feelings with each other, or even the moments he revealed so many of the pulsar secrets to me? Nothing sounds good enough to express my true gratitude to him. I really miss you a lot Bhal.

Although I know Simos Konstantidis would not allow me to dedicate a paragraph to him, I feel absolutely obliged to do so. The 5 years of our relationship have revealed to me a person of inconceivably rare values. I have never heard him refusing anything to anybody in need. Concerning me, he has been a life-raft. His contribution to the project has been very important as he he took good care of a great deal of trivialities that had to do with it. In several cases, the obstacles would have been insurmountable without his encouragement. From the depth of my heart, I send him my most sincere wishes for his future career in Pennsylvania State University.

I wish I had the power to make up for all the good Georgia Grivaki has done to me. Admittedly, she served as a “spare” mother. Always being ready to help without asking back anything. I owe her my thankfulness along with a promise for an everlasting friendship.

Many thanks to George Hobbs and Stephen Oord for the invaluable comments they made on my text and their will to help me with anything. I would also like to thank the members of the staff, both at the Jodrell Bank Observatories and the Observatory of Thessaloniki.

As a conclusion, I want to thank Anthony Keidis, Flea, John Frusciante and Chad Smith for composing “Californication”. Whenever things seemed to have stuck, listening to the song was enough to rejuvenate me.

[1]This paragraph was excepted from the report correction procedure since, I knew, Professor Seiradakis would strongly ask me not to include it in my report. Not even for a single moment have I thought of accepting such a request. My precious Evanthia Petropoulou (Phd student in linguistics in the University of Basel) had the kindness to make all the necessary corrections. Hence, I regard myself the only responsible for any mistakes of any kind.

Bibliography

[Baade and Zwicky, 1934] Baade, W. and Zwicky, F. (1934). On super-novae. *Proc. Nat. Acad. Sci.*, 20:254.

[Charalampous, 1981] Charalampous, S. (1981). *Introduction to Nuclear Physics*. Aristotle University of Thessaloniki.

[Hewish et al., 1968] Hewish, A., Bell, S. J., Pilkington, J. D. H., Scott, P. F., and Collins, R. A. (1968). Obsrvation of a rapidly pulsating radio source. *Nature*, 217:709–713.

[Hobbs, 2001] Hobbs, G. (2001). personal communication. personal communication.

[Kramer, 1995] Kramer, M. (1995). *High Frequency Observations of Pulsars*. Max-Planck-Institut fur Radioastronomie.

[Kramer et al., 1994] Kramer, M., Wielebinski, R., Jessner, A., Gil, J. A., and Seiradakis, J. H. (1994). Geometrical analysis of average pulsar profiles using multi-component gaussian fits at several frequencies. i. method and analysis. *Astron. Astrophys. Suppl. Ser.*, 107:1–12.

[Landau, 1932] Landau, L., D. (1932). *Phys. Z.*, 1:285.

[Lorimer, 1999] Lorimer, D. R. (1999). Radio pulsars-an observer's perspective. *astro-ph*.

[Lyne and Graham-Smith, 1998] Lyne, A. G. and Graham-Smith, F. (1998). *Pulsar Astronomy*. Cambridge University Press.

[Lyne and Manchester, 1988] Lyne, A. G. and Manchester, R. N. (1988). The shape of pulsar radio beam. *Mon. Not. R. astr. Soc.*, 234:477–508.

[Manchester and Taylor, 1977] Manchester, R. N. and Taylor, J. H. (1977). *Pulsars*. W.H. Freeman and Company.

[Pasachoff, 1998] Pasachoff, J. M. (1998). *Astronomy. From the Earth to the Universe*. Saunders College Publishing.

[Rankin, 1983] Rankin, J. M. (1983). Toward an emperical theory of pulsar emission. i. morphological taxonomy. *The Astrophysical Journal*, 274:333–358.

[Seiradakis and Noutsos, 2000] Seiradakis, J. H. and Noutsos, A. (2000). personal communication. personal communication.

[Seiradakis and Varvoglis, 1994] Seiradakis, J. H. and Varvoglis, H. (1994). *Introduction to Contemporary Astronomy*. Ziti's Publications.

[Smith, 2000] Smith, F. G. (2000). personal communication. personal communication.

[Thorsett, 1991] Thorsett, S., E. (1991). Frequency dependence of pulsar integrated profiles. *The Astrophysical Journal*, 377:263–267.